

## SIMULATION OF SOLUTE TRANSPORT IN FRACTURED AQUIFERS

DEVELOPMENT OF SOLUTIONS FOR RAPID SIMULATION OF SOLUTE  
TRANSPORT IN FRACTURED AQUIFERS

By MOHAMED MAHMOUD KHAFAGY, B.SC., M.SC.

A Thesis Submitted to the School of Graduate Studies in Partial Fulfilment of the  
Requirements for the Degree Doctor of Philosophy

McMaster University © Copyright by Mohamed Khafagy, October 2022

McMaster University DOCTOR OF PHILOSOPHY (2022) Hamilton, Ontario (Civil Engineering)

TITLE: Development of Solutions for Rapid Simulation of Solute Transport in Fractured Aquifers

AUTHOR: Mohamed Mahmoud Khafagy Mahmoud, B.Sc., M.Sc. (Cairo University)

SUPERVISORS: Professor S. E. Dickson-Anderson and Professor W. El-Dakhakhni

NUMBER OF PAGES: xxii, 191

## **Lay Abstract**

Aquifer pollution by various contaminants is an issue of concern across Canada. It has been well-established that fractured aquifers can be highly susceptible to contamination. Contaminants are primarily transported through fractures over a period of decades or longer; however, storage occurs in the surrounding rock matrix. Contaminant transport models are important tools for understanding field conditions and developing aquifer management and remediation strategies. Unfortunately, currently available modeling approaches either lack accuracy or require extensive computational resources when applied to field-scale problems. The goal of this study is to develop a suite of modeling tools that are accurate and efficient enough to capture solute transport processes in fractured aquifers occurring at the field scale.

## **Abstract**

Understanding the flow and transport of contaminants in fractured rocks play a fundamental role in geo-environmental problems since subsurface contamination poses a serious threat to human health and the environment. Therefore, it is imperative to understand solute transport in these environments; models are an important tool in the advancement of our understanding. Aquifers in which the flow pattern is dominated by a network of connected fractures present challenges with respect to modeling due to the high degree of heterogeneity in fracture density and geometry. The goal of this research is to develop a suite of modeling tools that are accurate, computationally stable, and efficient enough to simulate solute transport in complex, discrete fracture networks (DFNs). Four research objectives have been designed to achieve this goal: (1) develop a computationally efficient analytical model for simulating two-dimensional spatial and temporal solute transport in discrete fracture networks (DFNs), (2) develop a closed-form solution describing the classical advection-dispersion equation for simulating reactive transport in single, parallel-plate fractures under a range of conditions, (3) develop a numerical model (based on the closed-form solution developed in Objective 2) to simulate solute transport in small-scale ( $\sim 350$  m  $\times$  350 m) discrete fracture networks considering mass exchange between the fracture and surrounding matrix, and (4) upscale the frameworks developed in Objectives 1 and 3 to develop an accurate and computationally efficient numerical model simulating solute transport in field-scale fracture networks. The developed analytical model (Objective 1) provides a useful reference tool for the verification of numerical dual-porosity fracture network simulations. The other developed numerical approaches (Objectives 2, 3, and 4) advance solute transport behavior predictions in fractured environments as they are both simpler and more computationally efficient than currently adopted techniques, which is particularly important for simulating fracture networks at the macroscopic scale.

## **Acknowledgements**

I would like to express my gratitude to my supervisors, Prof. Sarah Dickson and Prof. Wael El-Dakhakhni for their guidance, support, and encouragement throughout my Ph.D. They have been a great source of inspiration and allowed me to explore my research with freedom and enthusiasm along with their guidance and support. I will be always grateful to them. I would like to extend my appreciation to my committee members, Prof. Paulin Coulibaly and Dr. Benzhong (Robin) Zhao for providing their support, input, ideas, and comments. I would like to extend my deep gratitude to my M.Sc. supervisors, Prof. Ahmed Emam and Dr. Mohamed Attia for their guidance during my masters which helped me reach this milestone.

Last but not least, without the support and love of my family and my wife, I know I wouldn't be at this point now. Thanks must go to my father, Mahmoud, my mother, Nahed, and my sister, Yasmina, for their overseas endless support, unconditional love, encouragement, and sacrifice. Your prayer for me was what sustained me this far. I would like to give a special thanks to my wife, Yasmin, for her support to pass the challenges together with our little ones, Ali and Lily, who gave me the emotional support throughout the research work.

## Table of Contents

Lay Abstract.....	iii
Abstract.....	iv
Acknowledgements.....	v
Table of Contents.....	vi
List of Figures .....	x
List of Tables.....	xvi
List of Abbreviations and Symbols.....	xvii
Acronyms.....	xviii
Declaration of Academic Achievement.....	xix
Preface.....	xxii
Chapter 1: Introduction.....	1
1.1. Analytical Solutions and Numerical Modelling.....	2
1.1.1. Stochastic Continuum (SC) and Fracture Continuum (FC) Models.....	3
1.1.2. Discrete Fractures Models .....	4
1.2. Research Objectives .....	7
1.3. Layout of the Dissertation .....	8
1.4. References .....	11

Chapter 2: Analytical Model for Solute Transport in Discrete Fracture Networks: 2D Spatiotemporal

Solution with Matrix Diffusion.....	20
2.1. Introduction .....	22
2.2. Model Development .....	27
2.3. Model Verification .....	33
2.4. Results and Discussion .....	35
2.5. Conclusion .....	44
2.6. Acknowledgment.....	46
2.7. References .....	47
Chapter 3: Multi-Gene Genetic Programming Solution for Simulating Solute Transport in Fractures....	56
3.1. Introduction .....	58
3.2. Model Development .....	62
3.2.1. Dataset.....	63
3.2.2. Multi-gene Genetic Programming .....	65
3.3. Results and Discussion .....	71
3.3.1. MGGP Model Structure and Evaluation .....	76
3.3.2. MGGP Model Verification.....	86
3.4. Conclusion .....	88
3.5. Acknowledgment.....	89
3.6. References .....	90

Chapter 4: A Rapid, Simplified, Hybrid Modeling Approach for Simulating Solute Transport in Discrete Fracture Networks.....	98
4.1. Introduction .....	100
4.2. Model Development .....	103
4.3. Model Verification and Validation.....	107
4.4. Results and Discussion .....	112
4.5. Conclusion .....	121
4.6. Acknowledgment.....	122
4.7. References .....	123
 Chapter 5: Computationally efficient upscaled model for simulating solute transport in complex large-scale fracture networks .....	 133
5.1. Introduction .....	135
5.2. Objectives .....	138
5.3. Model Development .....	139
5.3.1. Steady State Flow Simulation.....	141
5.3.2. Solute Transport Using RWPT .....	143
5.3.3. Upscaling the Fracture Network Model.....	145
5.4. Results and Discussion .....	149
5.4.1. Model Validation.....	149
5.4.2. Impact of EV-FN Size .....	152
5.4.3. Mass Distribution using the UFN model .....	153

5.2. Conclusion ..... 155

5.3. Acknowledgment..... 157

5.4. References ..... 158

Chapter 6: Summary and Conclusions ..... 165

Appendix 1..... 169

    References ..... 172

Appendix 2..... 173

    References ..... 175

Supplementary Data A (TDRW-Based Model)..... 176

    References ..... 179

Supplementary Data B (RWPT-Based Model) ..... 180

    References ..... 191

## List of Figures

Fig. 2-1: Schematic of a single fracture illustrating the solute growth/decay and sorption processes. .....	28
Fig. 2-2: Schematic diagram illustrating mixing at intersections within a fracture network for (a) the CM method; and (b) the ST method. ....	31
Fig. 2-3: Synthetic fracture networks for model verification. Solid lines represent hydraulically active fractures, while dashed lines represent dead-end fractures. ....	34
Fig. 2-4: BTCs for Case 1 ( $t_{1/2} = n/a$ ; $R = 1$ or $4$ ; $\theta = 0$ ; $D^* = 0$ m <sup>2</sup> /sec) calculated using both CN and ST mass sharing methods in (a) FN1, and (b) FN2 with a Type 1 boundary condition. Lines represent and symbols represent AN and TDRW model simulations, respectively. ....	36
Fig. 2-5: BTCs for Case 2 ( $t_{1/2} = 20$ or $40$ days; $R = 1$ ; $\theta = 0$ ; $D^* = 0$ m <sup>2</sup> /sec) calculated using both CM and ST mass sharing methods in FN1 with a Type 1 boundary condition. Lines represent AN model and symbols represent TDRW model. ....	38
Fig. 2-6: BTCs for Case 3 ( $t_{1/2} = n/a$ ; $R = 1$ ; $\theta = 0.1$ ; $D^* = 1 \times 10^{-9}$ m <sup>2</sup> /sec) calculated using the CM mass sharing method in FN1 with a Type 1 boundary condition, and $Pe = 18$ at the network intersections. Lines and symbols represent AN and RWPT model simulations, respectively. ....	39
Fig. 2-7: BTCs calculated for Case 1 ( $t_{1/2} = n/a$ ; $R = 1$ ; $\theta = 0$ ; $D^* = 0$ m <sup>2</sup> /sec) by the AN model at intersections A and B (see Fig. 2-3) using the CM mass sharing method in FN1 for (a) Type 1 and (b) Type 2 boundary conditions. ....	40

Fig. 2-8: BTCs calculated using the AN model for Case 1 ( $t_{1/2} = n/a$ ;  $R = 1$ ;  $\theta = 0.1$ ;  $D^* = 1 \times 10^{-7}$  or  $1 \times 10^{-10}$  m<sup>2</sup>/sec) using both the CM and ST mass sharing methods in FN1 based on a Type 2 boundary conditions for (a) no matrix diffusion and  $Pe = 9 \times 10^{-5}$  at the intersections, (b) matrix diffusion and  $Pe = 9 \times 10^{-5}$  at the intersections, (c) no matrix diffusion and  $Pe = 178$  at the intersections, and (d) matrix diffusion and  $Pe = 178$  at the intersections... 42

Fig. 2-9: BTCs calculated using the CM mass sharing method in FN1 comparing AN simulations to TDRW and RWPT simulations with different numbers of particles released for (a) Case 1 with a Type 2 boundary condition ( $t_{1/2} = n/a$ ;  $R = 1$ ;  $\theta = 0$ ;  $D^* = 0$  m<sup>2</sup>/sec) and (b) Case 3 with a Type 1 boundary condition ( $t_{1/2} = n/a$ ;  $R = 1$ ;  $R' = 1$ ;  $\theta = 0.1$ ;  $D^* = 1 \times 10^{-9}$  m<sup>2</sup>/sec). ..... 43

Fig. 3-1: Example of a multigene symbolic model..... 66

Fig. 3-2: MGGP flowchart..... 68

Fig. 3-3: Network analysis based on weighted adjacency representing the final dataset. .... 73

Fig. 3-4: Solute concentration vs  $\log(\epsilon)$  at  $t = 5 \times 10^4$  years for case A and  $t = 450$  years for case B. Case A represents a parameter combination for which the midpoint rule requires additional discretization (i.e., more than 50,000 points) to generate an accurate curve defining the  $\epsilon$  integral. Case B represents a parameter combination for which the midpoint rule with the prescribed 50,000 discretization points can generate an accurate curve defining the  $\epsilon$  integral..... 75

Fig. 3-5: Boxplot of (a) RMSE and (b)  $r^2$  for the generated BTCs using lognormal distribution. 76

Fig. 3-6: MGGP tree structure representing the expression for  $\mu p$ . ..... 79

Fig. 3-7: MGGP tree structure representing the expression for  $\sigma p$ . ..... 79

Fig. 3-8: Best fitness (RMSE) versus generation number for (a) $\mu p$ and (b) $\sigma p$ components of the MGGP models. ....	81
Fig. 3-9: Observed versus predicted values of (a) $\mu$ and (b) $\sigma$ of the lognormal distribution. Blue dots represent training and validation data, and red dots represent testing data. Points A, B, and C represent BTCs with overpredicted, well-predicted, and underpredicted $\sigma$ , respectively. ....	82
Fig. 3-10: Observed and predicted BTCs for (a) overestimated, (b) well-estimated, and (c) underestimated $\sigma$ of the lognormal distribution (points A, B, and C, respectively, from Fig. 3-9). ....	83
Fig. 3-11: Box and whisker plots of residuals for the lognormal distribution parameters (a) $\mu$ and (b) $\sigma$ . ....	85
Fig. 3-12: Sensitivity of the MGGP SF-ST ( $\mu p$ and $\sigma p$ ) model to each of the input variables ( $X1$ to $X7$ ). ....	86
Fig. 3-13: MGGP SF-ST model (circles) vs analytical solution (asterisks) vs RWPT model (squares) for transport in a single fracture. ....	87
Fig. 4-1: Synthetic fracture network (DFN1) for model verification. Solid lines represent hydraulically active fractures, while dashed lines represent dead-end fractures. ....	108
Fig. 4-2: CFD model discretization scheme for DFN1 (Fig. 4-1). ....	110
Fig. 4-3: High fracture density DFN (DFN2) used for the simulation of spatial and temporal solute mass. ....	112

Fig. 4-4: BTCs for Case 1 ( $\alpha = 5$  m;  $2b = 250$   $\mu$ m;  $2B = 1$  m;  $D^* = 1 \times 10^{-7}$  m<sup>2</sup>/sec;  $Rm = 1 - 3$ ;  $\theta = 0.1$ ;  $\tau = 1$ ) for (a) Type 1 and (b) Type 2 boundary conditions – lines represent AN model and symbols represent the developed model. .... 113

Fig. 4-5: BTCs for Case 2 ( $\alpha = 5$  m;  $2b = 250$   $\mu$ m;  $2B = 1 - 3$  m;  $D^* = 1 \times 10^{-7}$  m<sup>2</sup>/sec;  $Rm = 1$ ;  $\theta = 0.1$ ;  $\tau = 1$ ) for (a) Type 1 and (b) Type 2 boundary conditions – lines represent AN model and symbols represent the developed model. .... 114

Fig. 4-6: BTCs for Case 3 ( $\alpha = 5$  m;  $2b = 250$   $\mu$ m;  $2B = 13.7$  m;  $D^* = 1 \times 10^{-7}$  m<sup>2</sup>/sec;  $Rm = 1$ ;  $\theta = 0.1$ ;  $\tau = 1$ ) for Type 1 BC calculated by the CFD model and the developed model. .... 116

Fig. 4-7: Spatial distribution of the solute concentration in DFN1 after 475 years from the time of release. Simulations are conducted using parameters for Case 3 ( $\alpha = 25$  m;  $2b = 250$   $\mu$ m;  $2B = 13.7$  m;  $D^* = 1 \times 10^{-7}$  m<sup>2</sup>/sec;  $Rm = 1$ ;  $\theta = 0.1$ ;  $\tau = 1$ ) based on constant release (Type 1 BC) represented by (a) the CFD model using COMSOL and (b) the developed model. .... 117

Fig. 4-8: Spatial distribution of the solute mass in DFN 2 at 20, 40, 60, and 80 years from the time of release. Simulations are conducted using parameters for Case 1 ( $\alpha = 5$  m;  $2b = 250$   $\mu$ m;  $2B = 1$  m;  $D^* = 1 \times 10^{-7}$  m<sup>2</sup>/sec;  $Rm = 1$  and 5;  $\theta = 0.1$ ;  $\tau = 1$ ) based on a 10 kg pulse release (Type 2 BC). .... 118

Fig. 4-9: Effect of changing  $D^*$ ,  $\alpha$ ,  $2b$ , and  $2B$  on the spatial distribution of the solute mass in DFN2 (i.e., fractures and matrix). Panel (a) represents the base case at  $t = 20$  years based on Case 1 parameters ( $\alpha = 5$  m;  $2b = 250$   $\mu$ m;  $2B = 1$  m;  $D^* = 1 \times 10^{-7}$  m<sup>2</sup>/sec;  $Rm = 1$ ;  $\theta = 0.1$ ;  $\tau = 1$ ) under a Type 2 BC. Individual parameters are perturbed in panels (b)  $D^* = 1 \times 10^{-9}$  m<sup>2</sup>/sec, (c)  $\alpha = 10$  m, (d)  $2b = 400$   $\mu$ m, and (e)  $2B = 0.5$  m. .... 120

Fig. 5-1: Illustration of the model at different scales (i.e., micro, macro, and regional network scales). Note the FCs (identified by red arrows) are upscaled from the micro to macro to regional scales. .... 140

Fig. 5-2: The macro scale network used in the simulation showing the hydraulic head along each boundary (i.e., quadrilateral). All dead-end and isolated fractures have been removed..... 142

Fig. 5-3: The macro- and micro-network scales showing the EV-FNs in the macro scale in green, the EV-FNs in the micro scale in blue, and the FCs in red..... 145

Fig. 5-3: An example for the micro scale network showing the FCs in blue EV-FNs. The purple EV-FCs describe the solute retention in the flow channels. .... 146

Fig. 5-5: The EV-FCs with corresponding BTCs (in the micro-scale network) for all five possible FCs in case the flow direction is from left to right (i.e., solute transport directions). Solute is released along the influent (red) boundary, and the BTC is calculated at the effluent (blue) boundary. .... 148

Fig. 5-6: FC-based networks and solute masses corresponding to the micro scale network (Fig. 5-3b) for (a)  $\alpha = 1$  m and (b)  $\alpha = 5$  m..... 150

Fig. 5-7: BTCs from model validation runs (i.e., network properties in Table 5-1 in the micro-scale network (Fig. 5-4) with a Type 1 boundary condition for  $\alpha = 1$  m and  $\alpha = 5$  m. Solid blue lines represent the RWPT model and dashed red lines represent the UFN model..... 151

Fig. 5-8: RMSE versus EV-FN size for the BTCs at effluent boundaries of the UFN model for  $\alpha = 1$  m. .... 153

Fig. 5-9: BTCs calculated for network properties in Table 2-1 calculated by the UFN model at effluent boundaries in the macro scale network (Fig. 2-3) for Type 1 boundary condition. Lines and dashed lines represent simulations for  $\alpha = 1$  m and  $\alpha = 5$  m, respectively. .... 154

## List of Tables

Table 1-1: Comparison between various numerical modelling of fractured rocks.....	6
Table 2-1: Properties of the DFN for the cases used in the verification.....	35
Table 3-1: Range of values for fracture and solute properties.....	64
Table 3-2: Parameter and setting for best MGGP models.....	70
Table 3-3: Pearson correlation coefficients ( $r$ ) between input and output parameters.....	80
Table 3-4: p-values for Wilcoxon rank-sum and Levene's tests (95% confidence level).....	84
Table 4-1: Properties of the DFN for the Cases used in the verification and validation.....	108
Table 5-1: Simulation parameters.....	143

## List of Abbreviations and Symbols

$v$ [L/T]	Groundwater velocity in the fracture
$2b$ [L]	Fracture aperture width
$D$ [L <sup>2</sup> /T]	Hydrodynamic dispersion coefficient along the fracture
$D'$ [L <sup>2</sup> /T]	Diffusion coefficient in the porous matrix
$\alpha_L$ [L]	Dispersivity
$R$ [-]	Fracture retardation coefficient
$R'$ [-]	Matrix retardation coefficient
$\theta$ [-]	Matrix porosity
$\theta_f$ [-]	Porosity within the fracture
$t$ [T]	Time
$\lambda$ [T <sup>-1</sup> ]	First-order decay constant
$t_{1/2}$ [T]	Half-life of the solute
$K_f$ [L]	Fracture distribution coefficient
$K_m$ [L <sup>3</sup> /M]	Matrix distribution coefficient
$C$ [M/L <sup>3</sup> ]	Solute concentration
$\tau$ [-]	Matrix tortuosity
$F_x$ [M/L <sup>2</sup> · T]	Mass flux
$P_e$ [-]	Peclet number
$Q$ [L <sup>3</sup> /T]	Volumetric flow rate in fracture
$V^*$ [L/T]	Characteristic velocity at the fracture intersection

## **Acronyms**

DFN:	Discrete fracture network model
DFM:	Discrete fracture-matrix model
CF:	Continuum fracture model
ADE:	Advection-dispersion equation
AN model:	Analytical network model
MGGP:	Multi-gene genetic programming approach
MGGP SF-ST:	Multi-gene genetic programming single fracture solute transport model
EA:	Evolutionary algorithm
UFN:	Upscaled fracture network model
RWPT:	Random walk particle tracking method
TDRW:	Time domain random-walk method
BTC:	Breakthrough curve
FC:	Fracture channel/Fracture continuum
EV:	Elementary volume
CM:	Complete mixing method
ST:	Stream tube method
PDF:	Probability density function
CDF:	Cumulative distribution function

## **Declaration of Academic Achievement**

This thesis has been prepared in accordance with the guidelines of the sandwich thesis format from the School of Graduate Studies at McMaster University. Four papers are included in this thesis as listed below.

1. Khafagy, M., El-Dakhakhni, W., Dickson-Anderson, S., 2022a. Analytical model for solute transport in discrete fracture networks: 2D spatiotemporal solution with matrix diffusion. *Comput. Geosci.* 159, 104983. <https://doi.org/10.1016/j.cageo.2021.104983>
2. Khafagy, M., El-Dakhakhni, W., Dickson-Anderson, S., 2022b. Multi-gene genetic programming expressions for simulating solute transport in fractures. *J. Hydrol.* 606, 127316. <https://doi.org/10.1016/j.jhydrol.2021.127316>
3. Khafagy, M., Dickson-Anderson, S., El-Dakhakhni, W., 2022c. A Rapid, Simplified, Hybrid Modeling Approach for Simulating Solute Transport in Discrete Fracture Networks. (Submitted to *Computers and Geotechnics* journal).
4. Khafagy, M., Dickson-Anderson, S., El-Dakhakhni, W., 2022d. Towards simulating solute transport in complex, regional-scale fracture networks: a computationally efficient approach. (Submitted to *Water Resources Research* journal).

The first manuscript is presented in Chapter 2. The manuscript was submitted in April 2021 and accepted in November 2021. The work was conducted under the supervision of Drs. Sarah Dickson-Anderson and Wael El-Dakhakhni. The manuscript is included in this thesis as it represented an analytical network model to simulate solute transport in two-dimensional fracture networks considering advection and dispersion within the fracture, sorption on the fracture walls

and within the matrix, matrix diffusion, and first-order decay. My contributions include conceptualization, methodology, software, formal analysis, writing, and original draft preparation. The second manuscript is presented in Chapter 3. The manuscript was submitted in August 2021 and accepted in December 2021. The work was conducted under the supervision of Drs. Sarah Dickson-Anderson and Wael El-Dakhakhni. The manuscript is included in this thesis as it represented a closed-form solution (MGGP SF-ST) employing the multi-gene genetic programming approach to simulate reactive transport in a single, parallel plate fracture under a range of hydraulic, geological and chemical conditions for either a constant concentration or pulse injection at the inlet. My contributions include conceptualization, methodology, software, formal analysis, writing, and original draft preparation.

The third manuscript is presented in Chapter 4. The manuscript was submitted in March 2022 to Computers and Geotechnics journal. The work was conducted under the supervision of Drs. Sarah Dickson-Anderson and Wael El-Dakhakhni. The manuscript is included in this thesis as it represented a numerical model to simulate the solute transport in fracture networks based on an extension of the MGGP SF-ST model for solute transport in a single fracture considering advection and dispersion along the fracture; molecular diffusion within the fracture and into the matrix; and, adsorption within the matrix for Type 1 and Type 2 BC. My contributions include conceptualization, methodology, software, formal analysis, writing, and original draft preparation.

The fourth manuscript is presented in Chapter 5. The manuscript was submitted in July 2022 to Water Resources Research journal. The work was conducted under the supervision of Drs. Sarah Dickson-Anderson and Wael El-Dakhakhni. The manuscript is included in this thesis as it

represented an upscaled fracture network (UFN) model employing random walk particle tracking approach in a discrete fracture network. The UFN model accurately captures solute transport processes occurring at the macro scale fracture networks. My contributions include conceptualization, methodology, software, formal analysis, writing, and original draft preparation.

## **Preface**

### **Chapter 2 Contributions:**

Mohamed Khafagy: Conceptualization, Methodology, Software, Formal analysis, Writing, and Original draft preparation.

Sarah Dickson-Anderson: Writing & Review & Editing, Supervision, and Funding acquisition.

Wael El-Dakhakhni: Writing & Review & Editing, Supervision, and Funding acquisition.

### **Chapter 3 Contributions:**

Mohamed Khafagy: Conceptualization, Methodology, Software, Formal analysis, Writing, and Original draft preparation.

Sarah Dickson-Anderson: Writing & Review & Editing, Supervision, and Funding acquisition.

Wael El-Dakhakhni: Writing & Review & Editing, Supervision, and Funding acquisition.

### **Chapter 4 Contributions:**

Mohamed Khafagy: Conceptualization, Methodology, Software, Formal analysis, Writing, and Original draft preparation.

Sarah Dickson-Anderson: Writing & Review & Editing, Supervision, and Funding acquisition.

Wael El-Dakhakhni: Writing & Review & Editing, Supervision, and Funding acquisition.

### **Chapter 5 Contributions:**

Mohamed Khafagy: Conceptualization, Methodology, Software, Formal analysis, Writing, and Original draft preparation.

Sarah Dickson-Anderson: Writing & Review & Editing, Supervision, and Funding acquisition.

Wael El-Dakhakhni: Writing & Review & Editing, Supervision, and Funding acquisition.

## **Chapter 1: Introduction**

More than 50% of the global population relies on groundwater for their potable water supply, and 30% rely on groundwater as their sole source of potable water (Döring, 2020). Increasing population and industrialization have resulted in increasing demands for energy and potable water. Related activities, such as radioactive waste disposal (e.g., Alzamel et al., 2022; Karolytė et al., 2022; Malkovsky and Yudinsev, 2022), percolation of leachate from landfills (e.g., Brunella and Raffaele, 2022; Javahershenas et al., 2022; Wang et al., 2022), salt water intrusion (e.g., Luo et al., 2022; Tran et al., 2022; Yuan et al., 2022), oil spills (e.g., Kalibatiene and Burmakova, 2022; Mallants et al., 2022; Scanlon et al., 2022), exploitation of petroleum (e.g., Demenev et al., 2022; Li et al., 2022; Wei et al., 2022), gas and geothermal reservoirs (e.g., Morais et al., 2022; Ryu et al., 2022; Zhao et al., 2022), and seepage from mining operations (e.g., Adamovic et al., 2022; Singha et al., 2022; Xu et al., 2022) have resulted in increasing groundwater contamination. As near-surface groundwater supplies become depleted or contaminated, deeper supplies, which often exist in fractured rock formations, must be accessed. As such, there is an increased interest in understanding the processes associated with groundwater flow and solute transport in fractured rock aquifers.

The mechanisms governing solute transport in fractures include advection, dispersion, diffusion, sorption, radioactive decay, and a range of chemical and biological reactions. The principal mechanisms for solute transport in fractures are advection and hydrodynamic dispersion (due to high permeability and low storage capacity), whereas the surrounding matrix is primarily

accessible by diffusion (due to low permeability and high storage capacity) (Bishop et al., 2020; Chen and Zhan, 2018; Hyman et al., 2019; Zhou et al., 2017). Fractured aquifers are often very heterogeneous due to the sparse and irregular nature of discrete fractures, which impacts flow pathways and affects transport process. There have been extensive contributions to the literature over the last few decades regarding flow and solute transport through either single fractures or fracture networks through analytical solutions and numerical models.

### **1.1. Analytical Solutions and Numerical Modelling**

Analytical models have gained much attention, as they can provide valuable insights into fundamental physical phenomena and are computationally efficient over a wide range of time scales required for performance assessments of radioactive waste repositories. Several analytical solutions have been developed to simulate solute transport in single fractures. Although analytical models have provided important insights into solute transport behavior in fractured rock, they lack in obtaining closed-form solutions for complex fracture network geometries, however they require numerical tools to obtain the transport solution.

Numerical modelling is an efficient tool that approximates the process-based mathematical formulations that describe the coupled behavior of flow and transport in fracture network domain. In general, the numerical models for solute transport in fractured aquifer are based on different representation concepts of fractures and matrix in the aquifer (Bear, 1993; Neuman, 2005). These models are mathematical equations which translate the conceptual model that describes the main geological and hydrogeological features of the fractured porous media that control the fluid flow

and transport behaviours in the system (Hawez et al., 2021). The development of conceptual models for flow and transport in fractured rocks is a significant research problem for subsurface contamination (Lei et al., 2019). Many numerical models have been presented to describe fractured porous media, which can be divided into four categories: (1) stochastic continuum approaches (Hammond et al., 2014; Lichtner et al., 2015; Trinchero et al., 2017), (2) fracture continuum (FC) models (Ahmed et al., 2019; Dong et al., 2019; Jackson et al., 2000; Kalinina et al., 2014; Khoei et al., 2020; L. Wang et al., 2020), (3) discrete fracture network (DFN) models (Feng et al., 2020; Jiang et al., 2021; Yao et al., 2020), and (4) discrete fracture- matrix (DFM) models (Chen et al., 2020; Flemisch et al., 2018; Sandve et al., 2012; Sweeney et al., 2020).

### **1.1.1 Stochastic Continuum (SC) and Fracture Continuum (FC) Models**

SC and FC models represent the fracture network using an equivalent porous medium with different scales. The SC models state that both fracture and matrix are either in the same domain (single continuum approach) where fractured permeability is adapted by one continuum or are represented as two separate continua (dual continuum approach), such as with dual porosity and dual permeability values. The fluctuation of permeability tensor in space and its orientation might vary, based on the fracture properties and network. On the other hand, FC models utilize a small scale finite difference discretization to preserve fracture network details for solving fluid flow by assigning a conductivity value for each grid cells representing the rock matrix and those representing fractures (Ahmed et al., 2019; Botros et al., 2008; Reeves et al., 2008). The conductivity of the cells representing the rock matrix is assigned orders of magnitude less than that

representing fractures which restricts fluid flow to the fracture cells (Reeves et al., 2008).

In general, SC models are computationally less demanding than FC models; nonetheless, the effect of fracture geometry is not incorporated explicitly (i.e., fracture length, orientation, aperture variations, density), which reduces the accuracy of these models. However, FC models use a correction factor to preserve the total flux along the whole area of study (e.g., Ahmed et al., 2019).

### **1.1.2 Discrete Fractures Models**

Unlike the continuum models, the discrete fractures models explicitly define the fractures individually and model the fractured media as interacting fractures and rock matrix. It is necessary to simulate flow and solute transport in the natural fracture network explicitly with respect to their geometry in order to capture the heterogeneity in the system of fractures. There are two types of discrete fractures models in the literature, the first is the discrete fracture network (DFN) model which neglects matrix diffusion, and the second is the discrete fracture-matrix (DFM) model which considers matrix diffusion. A body of literature has solved the coupled groundwater flow and solute transport in fractured rock based on the DFN approach in order to advance the understanding of the influence of various mechanisms affecting transport processes media. Several different numerical modelling approaches have been applied, including: intermediate mesh generation (Blessent et al., 2009); partial differential equation (PDE) based constraint optimization approach (Berrone et al., 2018); finite element method (Hu et al., 2022); random walk particle tracking (Khafagy et al., 2020); and time-domain particle tracking (Trincherro et al., 2020). In the DFM model, the fracture and the matrix are treated differently. After gridding, the fracture is represented

as an element that is one dimension lower than the matrix element. For example, the fracture is represented as a polygon in 3D grids, whereas it is represented as a line segment in 2D grids. Irregular grids are used in DFM models to represent the randomness of fracture positions. In general, it is evident that, DFN modelling is a widely accepted concept for simulating groundwater flow and solute transport (Hawez et al., 2021). However, it becomes challenging to model a large-scale fracture network and incorporate the influence of local aperture variations. On the other hand, the DEM model has a high accuracy of the results as the model captures most of the fracture properties. However, the computing cost is extremely high when the scale of the fracture network is large, which limits its application to small-scale simulations. In conclusion, different types of fracture network models demonstrate different strengths in various aspects, but each technique has its own drawbacks, as listed in **Table 1-1** which provides a detailed comparison of distinct fracture network models.

**Table 1-1: Comparison between various numerical modelling of fractured rocks.**

Numerical Methods		Input Parameters	Advantages	Limitations
<b>Continuum model</b>	<b>Stochastic</b>	Properties of fractures and matrix.	<ul style="list-style-type: none"> <li>• Reduces geometrical complexity.</li> <li>• Suitable for large scale of application.</li> <li>• Uses deterministic or stochastic models.</li> </ul>	<ul style="list-style-type: none"> <li>• Implicit generation of system.</li> <li>• Valid only for using REV.</li> <li>• Uniform value of porosity and permeability.</li> </ul>
	<b>Fracture</b>	Properties of fractures, fracture sets and matrix blocks.	<ul style="list-style-type: none"> <li>• Explicit generation of the effect of each individual fractures.</li> <li>• Conforming structured mesh.</li> </ul>	<ul style="list-style-type: none"> <li>• Intensive computational time.</li> <li>• Correction factors are required in flow and solute transport simulations for accurate results.</li> </ul>
<b>Discrete fractures model</b>	<b>Without matrix diffusion</b>	Properties of fractures and fracture sets.	<ul style="list-style-type: none"> <li>• Explicit generation of the effect of each individual fracture.</li> <li>• Most popular and accurate numerical modelling.</li> </ul>	<ul style="list-style-type: none"> <li>• Rock matrix is impermeable.</li> <li>• Intensive computational time.</li> </ul>
	<b>With matrix diffusion</b>	Properties of fractures, fracture sets and matrix blocks.	<ul style="list-style-type: none"> <li>• No need for fluid exchange term between fracture and matrix interface.</li> <li>• Explicit generation of the effect of each individual fracture.</li> </ul>	<ul style="list-style-type: none"> <li>• Intensive computational time.</li> <li>• Conforming unstructured mesh.</li> <li>• Can found only by stochastic and probabilistic models.</li> </ul>

## 1.2. Research Objectives

The goal of this research is to develop a suite of accurate and computationally stable modeling tools that overcome the limitations of current approaches to simulate solute transport in complex DFNs. Four research objectives have been designed to achieve this goal:

- 1. Develop a computationally efficient analytical model to simulate two-dimensional spatial and temporal solute transport in discrete fracture networks (DFNs):** A computationally efficient analytical network (AN) model is developed to simulate two-dimensional spatial and temporal distribution of a solute considering advection and hydrodynamic dispersion within the fractures, matrix diffusion, sorption onto the fracture walls and in the matrix, and first order decay for one constituent.
- 2. Develop a closed-form solution to simulate reactive transport in single, parallel-plate fractures under a range of conditions:** An accurate, closed-form data-driven solution is developed to predict solute transport in single, parallel-plate fractures as a function of the parameters that describe relevant physical and chemical processes. The MGGP model is employed to obtain an accurate relationship between the hydraulic, geological, and chemical parameters of the fracture-matrix system as inputs and an ensemble of breakthrough curves as outputs. The developed solution is substantially more computational efficiency than current methods (i.e., numerical and analytical approaches).
- 3. Develop a numerical model (based on the closed-form solution developed in Objective 2) to simulate solute transport in small-scale (~40,000 m<sup>2</sup>) discrete fracture networks**

**considering mass exchange between the fracture and surrounding matrix:** A numerical model is developed to predict solute transport in discrete fracture networks to provide an understanding of how to address the longitudinal diffusion in the matrix by employing fracture dispersivity correction factor to approximate the results that considers the 2-dimensional matrix diffusion.

- 4. Upscale the frameworks developed in Objectives 1 and 3 to develop an accurate and computationally efficient numerical model simulating solute transport in field-scale fracture networks:** The upscaled Fracture Network (UFN) model is developed to accurately capture solute transport processes occurring at the macro scale in saturated fracture networks. The developed Upscaled Fracture Network (UFN) model generates representative flow channels (FCs) employing random walk particle tracking (RWPT) to obtain the solute migration scheme in the micro scale DFN to achieve upscaling.

### **1.3. Layout of the Dissertation**

The dissertation is organized as follows:

**Chapter (1):** This chapter provides an introduction including a brief background on studies carried out on solute transport from the literature, problem definition, objectives of the study, and thesis outline.

**Chapter (2):** This chapter provides a computationally efficient analytical network (AN) model for simulating solute transport in discrete fracture networks (DFNs). The AN model simulates two-dimensional spatial and temporal solute distribution and considers the mechanisms of advection

and hydrodynamic dispersion within the fractures, matrix diffusion, sorption onto the fracture walls and in the matrix, and first order decay for one constituent. Previously developed analytical solutions for a single fracture are implemented in the developed model, and a transfer function approach is applied to extend these solutions to a DFN. Mass sharing at fracture intersections is calculated using the complete mixing and stream-tube methods. The AN model was verified against numerical models based on random walk methods for a range of properties in two fracture networks. The sensitivity of the mass sharing methods was investigated for Peclet numbers ranging from  $P_e = 3 \times 10^{-6}$  - 380. The AN model provides a reference tool for the verification of numerical dual-porosity fracture network simulations.

**Chapter (3):** This chapter presents an approximate a solution of the classical advection-dispersion equation for reactive transport in single, parallel-plate fractures using multi-gene genetic programming approach. The approach is employed to obtain an accurate relationship between the hydraulic, geologic, and chemical parameters of the fracture-matrix system as inputs and an ensemble of breakthrough curves as outputs. This approach is simpler and computationally more efficient than currently adopted methods and therefore it advances solute transport behavior predictions especially when the simulation increases from that of a single fracture to a network.

**Chapter (4):** This chapter discusses the development of a numerical model to simulate spatial and temporal solute transport in discrete fracture networks with implementing the mass exchange between the fracture and the surrounding matrix. The developed model considers three mechanisms: advection and dispersion along the fracture, molecular diffusion within the fracture and into the matrix, and adsorption within the matrix. The developed model predictions are

compared to those of an existing analytical model and a computational fluid dynamics (CFD) model employing Navier Stokes equations. The model will facilitate solute transport simulations in complex fracture networks as a result of the pronounced computational efficiency in predicting solute transport.

**Chapter (5):** This chapter presents the development of an Upscaled Fracture Network (UFN) model employing random walk particle tracking (RWPT) in a DFN. The UFN model accurately captures solute transport processes occurring at the macroscopic scale in saturated fracture networks. The UFN model involves discretizing a complex fracture network into elementary volumes, within which both representative solute transport flow channels and their corresponding breakthrough curves were identified. This identified flow channels were then employed to construct the residence time at the macroscopic scale. The UFN model represents a significant advancement in simulating solute transport in complex, regional aquifers due to its computational efficiency, simple implementation, and high level of accuracy.

**Chapter (6):** A summary of the developed models along with the different analyses conducted within the dissertation are presented, and the main contribution to the literature is listed.

## 1.4. References

- Adamovic, D., Ishiyama, D., Kawaraya, H., Ogawa, Y., & Stevanovic, Z. (2022). Geochemical characteristics and estimation of groundwater pollution in catchment areas of Timok and Pek Rivers, Eastern Serbia: Determination of early-stage groundwater pollution in mining areas. *Groundwater for Sustainable Development*, 16(December 2021), 100719. <https://doi.org/10.1016/j.gsd.2021.100719>
- Ahmed, M. I., Abd-Elmegeed, M. A., & Hassan, A. E. (2019). Modelling transport in fractured media using the fracture continuum approach. *Arabian Journal of Geosciences*, 12(5). <https://doi.org/10.1007/s12517-019-4314-3>
- Alzamel, M., Haruna, S., & Fall, M. (2022). Saturated hydraulic conductivity of bentonite–sand barrier material for nuclear waste repository: effects of physical, mechanical thermal and chemical factors. *Environmental Earth Sciences*, 81(7), 1–13. <https://doi.org/10.1007/s12665-022-10358-0>
- Bear, J. (1993). Flow and Contaminant Transport in Fractured Rock. In *Flow and Contaminant Transport in Fractured Rock*. <https://doi.org/10.1016/c2009-0-29127-6>
- Berrone, S., Fidelibus, C., Pieraccini, S., Scialò, S., & Vicini, F. (2018). Unsteady advection-diffusion simulations in complex Discrete Fracture Networks with an optimization approach. *Journal of Hydrology*, 566(September), 332–345. <https://doi.org/10.1016/j.jhydrol.2018.09.031>
- Bishop, P., Persaud, E., Levison, J., Parker, B., & Novakowski, K. (2020). Inferring flow pathways between bedrock boreholes using the hydraulic response to borehole liner installation. *Journal*

- of Hydrology, 580(May 2019), 124267. <https://doi.org/10.1016/j.jhydrol.2019.124267>
- Blessent, D., Therrien, R., & MacQuarrie, K. (2009). Coupling geological and numerical models to simulate groundwater flow and contaminant transport in fractured media. *Computers and Geosciences*, 35(9), 1897–1906. <https://doi.org/10.1016/j.cageo.2008.12.008>
- Botros, F. E., Hassan, A. E., Reeves, D. M., & Pohll, G. (2008). On mapping fracture networks onto continuum. *Water Resources Research*, 44(8), 1–17. <https://doi.org/10.1029/2007WR006092>
- Brunella, R., & Raffaele, B. (2022). Tritium as a tool to assess leachate contamination: An example from Conversano landfill (Southern Italy). *Journal of Geochemical Exploration*, 235(November 2021), 106939. <https://doi.org/10.1016/j.gexplo.2021.106939>
- Chen, K., & Zhan, H. (2018). A Green's function method for two-dimensional reactive solute transport in a parallel fracture-matrix system. *Journal of Contaminant Hydrology*, 213, 15–21. <https://doi.org/10.1016/j.jconhyd.2018.03.006>
- Chen, Y., Wang, H., Wang, Y., & Ma, G. (2020). Numerical evaluation of a fracture acidizing treatment in a three-dimensional fractured carbonate reservoir. *Journal of Natural Gas Science and Engineering*, 81(May), 103440. <https://doi.org/10.1016/j.jngse.2020.103440>
- Demenev, A., Maksimovich, N., Khmurchik, V., Rogovskiy, G., Rogovskiy, A., & Baryshnikov, A. (2022). Field Test of In Situ Groundwater Treatment Applying Oxygen Diffusion and Bioaugmentation Methods in an Area with Sustained Total Petroleum Hydrocarbon (TPH) Contaminant Flow. *Water*, 14(2), 192. <https://doi.org/10.3390/w14020192>
- Dong, Z., Li, W., Lei, G., Wang, H., & Wang, C. (2019). Embedded discrete fracture modeling as

- a method to upscale permeability for fractured reservoirs. *Energies*, 12(5).  
<https://doi.org/10.3390/en12050812>
- Döring, S. (2020). Come rain, or come wells: How access to groundwater affects communal violence. *Political Geography*, 76(September 2019), 102073.  
<https://doi.org/10.1016/j.polgeo.2019.102073>
- Feng, S., Wang, H., Cui, Y., Ye, Y., Liu, Y., Li, X., Wang, H., & Yang, R. (2020). Fractal discrete fracture network model for the analysis of radon migration in fractured media. *Computers and Geotechnics*, 128(August), 103810. <https://doi.org/10.1016/j.compgeo.2020.103810>
- Flemisch, B., Berre, I., Boon, W., Fumagalli, A., Schwenck, N., Scotti, A., Stefansson, I., & Tatomir, A. (2018). Benchmarks for single-phase flow in fractured porous media. *Advances in Water Resources*, 111(January 2017), 239–258.  
<https://doi.org/10.1016/j.advwatres.2017.10.036>
- Hammond, G. E., Lichtner, P. C., & Mills, R. T. (2014). Evaluating the performance of parallel subsurface simulators: An illustrative example with PFLOTRAN. *Water Resources Research*, 50(1), 208–228. <https://doi.org/10.1002/2012WR013483>
- Hawez, H. K., Sanaee, R., & Faisal, N. H. (2021). A critical review on coupled geomechanics and fluid flow in naturally fractured reservoirs. *Journal of Natural Gas Science and Engineering*, 95(July), 104150. <https://doi.org/10.1016/j.jngse.2021.104150>
- Hu, Y., Xu, W., Zhan, L., Zou, L., & Chen, Y. (2022). Modeling of solute transport in a fracture-matrix system with a three-dimensional discrete fracture network. *Journal of Hydrology*, 605(September 2021), 127333. <https://doi.org/10.1016/j.jhydrol.2021.127333>

- Hyman, J. D., Rajaram, H., Srinivasan, S., Makedonska, N., Karra, S., Viswanathan, H., & Srinivasan, G. (2019). Matrix Diffusion in Fractured Media: New Insights Into Power Law Scaling of Breakthrough Curves. *Geophysical Research Letters*, 46(23), 13785–13795. <https://doi.org/10.1029/2019GL085454>
- Jackson, C. P., Hoch, A. R., & Todman, S. (2000). Self-consistency of a heterogeneous continuum porous medium representation of a fractured medium. *Water Resources Research*, 36(1), 189–202. <https://doi.org/10.1029/1999WR900249>
- Javahershenas, M., Nabizadeh, R., Alimohammadi, M., & Mahvi, A. H. (2022). The effects of Lahijan landfill leachate on the quality of surface and groundwater resources. *International Journal of Environmental Analytical Chemistry*, 102(2), 558–574. <https://doi.org/10.1080/03067319.2020.1724984>
- Jiang, L., Liu, J., Liu, T., & Yang, D. (2021). Semi-analytical modeling of transient pressure behaviour for fractured horizontal wells in a tight formation with fractal-like discrete fracture network. *Journal of Petroleum Science and Engineering*, 197(September 2020), 107937. <https://doi.org/10.1016/j.petrol.2020.107937>
- Kalibatiene, D., & Burmakova, A. (2022). Fuzzy Model for Predicting Contamination of the Geological Environment During an Accidental Oil Spill. *International Journal of Fuzzy Systems*, 24(1), 425–439. <https://doi.org/10.1007/s40815-021-01145-3>
- Kalinina, E. A., Klise, K. A., McKenna, S. A., Hadgu, T., & Lowry, T. S. (2014). Applications of fractured continuum model to enhanced geothermal system heat extraction problems. *SpringerPlus*, 3(1), 110. <https://doi.org/10.1186/2193-1801-3-110>

- Karolytè, R., Warr, O., van Heerden, E., Flude, S., de Lange, F., Webb, S., Ballentine, C. J., & Sherwood Lollar, B. (2022). The role of porosity in H<sub>2</sub>/He production ratios in fracture fluids from the Witwatersrand Basin, South Africa. *Chemical Geology*, 595(March). <https://doi.org/10.1016/j.chemgeo.2022.120788>
- Khafagy, M. M., Abd-Elmegeed, M. A., & Hassan, A. E. (2020). Simulation of reactive transport in fractured geologic media using random-walk particle tracking method. *Arabian Journal of Geosciences*, 13(2). <https://doi.org/10.1007/s12517-019-4952-5>
- Khoei, A. R., Salehi Sichani, A., & Hosseini, N. (2020). Modeling of reactive acid transport in fractured porous media with the Extended-FEM based on Darcy-Brinkman-Forchheimer framework. *Computers and Geotechnics*, 128(July), 103778. <https://doi.org/10.1016/j.compgeo.2020.103778>
- Lei, G., Liao, Q., & Zhang, D. (2019). A new analytical model for flow in acidized fractured-vuggy porous media. *Scientific Reports*, 9(1), 1–12. <https://doi.org/10.1038/s41598-019-44802-2>
- Li, R., Xiao, X., Zhao, Y., Tu, B., & Zhu, X. (2022). Characteristics of the Archaeal Communities in Petroleum Hydrocarbon-Contaminated Groundwater. *Water, Air, & Soil Pollution*, 233(3), 69. <https://doi.org/10.1007/s11270-022-05544-6>
- Lichtner, P. C., Hammond, G. E., Lu, C., Karra, S., Bisht, G., Andre, B., Mills, R., & Kumar, J. (2015). PFLOTRAN User Manual: A Massively Parallel Reactive Flow and Transport Model for Describing Surface and Subsurface Processes. <https://doi.org/10.2172/1168703>
- Luo, M., Zhang, Y., Li, H., Hu, W., Xiao, K., Yu, S., Zheng, C., & Wang, X. (2022). Pollution

assessment and sources of dissolved heavy metals in coastal water of a highly urbanized coastal area: The role of groundwater discharge. *Science of the Total Environment*, 807, 151070. <https://doi.org/10.1016/j.scitotenv.2021.151070>

Malkovsky, V., & Yudinsev, S. (2022). Numerical analysis of safety of a borehole repository for vitrified high-level nuclear waste. *Progress in Nuclear Energy*, 144(November 2021), 104075. <https://doi.org/10.1016/j.pnucene.2021.104075>

Mallants, D., Kirby, J., Golding, L., Apte, S., & Williams, M. (2022). Modelling the attenuation of flowback chemicals for a soil-groundwater pathway from a hypothetical spill accident. *Science of the Total Environment*, 806, 150686. <https://doi.org/10.1016/j.scitotenv.2021.150686>

Morais, T. A., Ladd, B., Fleming, N. A., & Ryan, M. C. (2022). Free-Phase Gas Detection in Groundwater Wells via Water Pressure and Continuous Field Parameters. *Groundwater*, 60(2), 262–274. <https://doi.org/10.1111/gwat.13135>

Neuman, S. P. (2005). Trends, prospects and challenges in quantifying flow and transport through fractured rocks. *Hydrogeology Journal*, 13(1), 124–147. <https://doi.org/10.1007/s10040-004-0397-2>

Reeves, D. M., Benson, D. A., & Meerschaert, M. M. (2008). Transport of conservative solutes in simulated fracture networks: 1. Synthetic data generation. *Water Resources Research*, 44(5), 1–10. <https://doi.org/10.1029/2007WR006069>

Ryu, H. S., Kim, H., Lee, J. Y., Kaown, D., & Lee, K. K. (2022). Abnormal groundwater levels and microbial communities in the Pohang Enhanced Geothermal System site wells pre- and

post-Mw 5.5 earthquake in Korea. *Science of the Total Environment*, 810, 152305.

<https://doi.org/10.1016/j.scitotenv.2021.152305>

Sandve, T. H., Berre, I., & Nordbotten, J. M. (2012). An efficient multi-point flux approximation method for Discrete Fracture-Matrix simulations. *Journal of Computational Physics*, 231(9), 3784–3800. <https://doi.org/10.1016/j.jcp.2012.01.023>

Scanlon, B. R., Reedy, R. C., & Wolaver, B. D. (2022). Assessing cumulative water impacts from shale oil and gas production: Permian Basin case study. *Science of the Total Environment*, 811, 152306. <https://doi.org/10.1016/j.scitotenv.2021.152306>

Singha, S. S., Singha, S., Pasupuleti, S., & Venkatesh, A. S. (2022). Knowledge-driven and machine learning decision tree-based approach for assessment of geospatial variation of groundwater quality around coal mining regions, Korba district, Central India. *Environmental Earth Sciences*, 81(2), 1–13. <https://doi.org/10.1007/s12665-021-10147-1>

Sweeney, M. R., Gable, C. W., Karra, S., Stauffer, P. H., Pawar, R. J., & Hyman, J. D. (2020). Upscaled discrete fracture matrix model (UDFM): an octree-refined continuum representation of fractured porous media. *Computational Geosciences*, 24(1), 293–310. <https://doi.org/10.1007/s10596-019-09921-9>

Tran, D. A., Tsujimura, M., Pham, H. V., Nguyen, T. V., Ho, L. H., Le Vo, P., Ha, K. Q., Dang, T. D., Van Binh, D., & Doan, Q. Van. (2022). Intensified salinity intrusion in coastal aquifers due to groundwater overextraction: a case study in the Mekong Delta, Vietnam. *Environmental Science and Pollution Research*, 29(6), 8996–9010. <https://doi.org/10.1007/s11356-021-16282-3>

- Trincherro, P., Painter, S. L., Poteri, A., Sanglas, J., Cvetkovic, V., & Selroos, J. O. (2020). A Particle-Based Conditional Sampling Scheme for the Simulation of Transport in Fractured Rock With Diffusion Into Stagnant Water and Rock Matrix. *Water Resources Research*, 56(4), 1–18. <https://doi.org/10.1029/2019WR026958>
- Trincherro, P., Puigdomenech, I., Molinero, J., Ebrahimi, H., Gylling, B., Svensson, U., Bosbach, D., & Deissmann, G. (2017). Continuum-based DFN-consistent numerical framework for the simulation of oxygen infiltration into fractured crystalline rocks. *Journal of Contaminant Hydrology*, 200(February), 60–69. <https://doi.org/10.1016/j.jconhyd.2017.04.001>
- Wang, H., Jiang, Z., Xu, W., Wang, R., & Xie, W. (2022). Physical model test on deformation and failure mechanism of deposit landslide under gradient rainfall. *Bulletin of Engineering Geology and the Environment*, 81(1), 1–14. <https://doi.org/10.1007/s10064-021-02566-y>
- Wang, L., Mou, J., Mo, S., Zhao, B., Liu, Z., & Tian, X. (2020). Modeling matrix acidizing in naturally fractured carbonate reservoirs. *Journal of Petroleum Science and Engineering*, 186(October 2019), 106685. <https://doi.org/10.1016/j.petrol.2019.106685>
- Wei, K. H., Ma, J., Xi, B. D., Yu, M. Da, Cui, J., Chen, B. L., Li, Y., Gu, Q. B., & He, X. S. (2022). Recent progress on in-situ chemical oxidation for the remediation of petroleum contaminated soil and groundwater. *Journal of Hazardous Materials*, 432(March), 128738. <https://doi.org/10.1016/j.jhazmat.2022.128738>
- Xu, J., Gui, H., Xia, Y., Zhao, H., Li, C., Chen, J., Wang, C., & Chen, C. (2022). Study on hydrogeochemical connection and water quality assessment of subsidence lake and shallow groundwater in Luling coal-mining area of the Huaibei coalfield, Eastern China. *Water*

Supply, 22(2), 1735–1750. <https://doi.org/10.2166/ws.2021.314>

Yao, W., Mostafa, S., Yang, Z., & Xu, G. (2020). Role of natural fractures characteristics on the performance of hydraulic fracturing for deep energy extraction using discrete fracture network (DFN). *Engineering Fracture Mechanics*, 230(February), 106962. <https://doi.org/10.1016/j.engfracmech.2020.106962>

Yuan, J., Xu, F., & Zheng, T. (2022). The genesis of saline geothermal groundwater in the coastal area of Guangdong Province: Insight from hydrochemical and isotopic analysis. *Journal of Hydrology*, 605(August 2021), 127345. <https://doi.org/10.1016/j.jhydrol.2021.127345>

Zhao, Z., Lin, Y.-F., Stumpf, A., & Wang, X. (2022). Assessing impacts of groundwater on geothermal heat exchangers: A review of methodology and modeling. *Renewable Energy*, 190, 121–147. <https://doi.org/10.1016/j.renene.2022.03.089>

Zhou, R., Zhan, H., & Chen, K. (2017). Reactive solute transport in a filled single fracture-matrix system under unilateral and radial flows. *Advances in Water Resources*, 104, 183–194. <https://doi.org/10.1016/j.advwatres.2017.03.022>

## **Chapter 2: Analytical Model for Solute Transport in Discrete Fracture Networks: 2D Spatiotemporal Solution with Matrix Diffusion**

This chapter describes a computationally efficient analytical network (AN) model for simulating solute transport in discrete fracture networks (DFNs). The AN model simulates two-dimensional spatial and temporal solute distribution and considers the mechanisms of advection and hydrodynamic dispersion within the fractures, matrix diffusion, sorption onto the fracture walls and in the matrix, and first order decay for one constituent. Previously developed analytical solutions for a single fracture are implemented in the developed model, and a transfer function approach is applied to extend these solutions to a DFN. Mass sharing at fracture intersections is calculated using the complete mixing and stream-tube methods. The AN model was verified against numerical models based on random walk methods for a range of properties in two fracture networks. The sensitivity of the mass sharing methods was investigated for Peclet numbers ranging from  $P_e = 3 \times 10^{-6}$  - 380. The AN model provides a reference tool for the verification of numerical dual-porosity fracture network simulations.

Authors: M. Khafagy, W. El-Dakhakhni, and S. E. Dickson-Anderson

Journal: Computers and Geosciences - DOI: 10.1016/j.cageo.2021.104983

### **Chapter 2 Contributions:**

Mohamed Khafagy: Conceptualization, Methodology, Software, Formal analysis, Writing, and Original draft preparation.

Sarah Dickson-Anderson: Writing & Review & Editing, Supervision, and Funding acquisition.

Wael El-Dakhakhni: Writing & Review & Editing, Supervision, and Funding acquisition.

## **Abstract**

A computationally efficient analytical network (AN) model simulating solute transport in discrete fracture networks (DFNs) is developed. The model simulates two-dimensional spatial and temporal distribution of a solute considering advection and hydrodynamic dispersion within the fractures, matrix diffusion, sorption onto the fracture walls and in the matrix, and first order decay for one constituent. The AN model is based on previously developed analytical solutions for a single fracture, and a transfer function approach is applied to extend these solutions to a DFN. Mass sharing at fracture intersections is calculated using the complete mixing and stream-tube methods. The AN model was verified against numerical models based on the time domain random walk and random walk particle tracking methods using two different fracture networks with a range of properties. In all cases, the AN model solutions showed excellent agreement with the numerical model solutions. The sensitivity of the mass sharing methods to the dominant transport mechanism (i.e., advection or diffusion) was investigated for Peclet numbers ranging from  $P_e = 3 \times 10^{-6}$  - 380. Both mass sharing methods give the same results when the transport processes are advection-dominated and matrix diffusion is considered; however, attention must be paid to the mass sharing method employed under other conditions, particularly when the fracture density is small. The AN model was at least 97% more efficient than the numerical models used in this work, and this efficiency will only increase with network complexity. The AN model provides a useful reference tool for the verification of numerical dual-porosity fracture network simulations.

**Key words:** solute transport, discrete fracture network, matrix diffusion, dual porosity, analytical model

## **2.1. Introduction**

More than 50% of the global population relies on groundwater for their potable water supply, and 30% rely on groundwater as their sole source of potable water (Döring, 2020). As groundwater resources become increasingly compromised, there is a growing need to access deeper water resources that are often present in fractured bedrock formations. As a result, the dependency on fractured rock aquifers as a primary water supply is increasing (Bondu et al. 2016; Marshall et al. 2019; Dippenaar, van Rooy, and Diamond 2019; Rao and Latha 2019; Bishop et al. 2020). However, these aquifers are also vulnerable to contamination as fractures represent particularly effective pathways for solute transport due to their high permeabilities relative to the surrounding rock matrix (Frampton et al. 2019). While mathematical modeling facilitates the development of effective management and monitoring strategies needed to protect groundwater supplies (Thakur et al., 2020), the strong heterogeneities in fractured rock aquifers have made it challenging to develop accurate solute transport models in these environments (Tsang et al. 2015). For example, safety assessments of deep geological repositories (DGRs) for nuclear waste storage rely on the earliest arrival time of radioactive contamination, requiring long-term prediction of low-concentration radionuclide migration. The earliest arrival time is sensitive to the heterogeneity of the system, which can only be reflected in modeling approaches that describe as much as possible of the aquifer features (i.e., explicit fractures and their orientations) and therefore preserve the properties of the flow pathway. Given this, a significant body of research has emerged over the past four decades focused on improving our understanding of solute transport in fractured media (Trincherio et al., 2020). Despite this, groundwater flow and solute transport in fractured aquifers

have been identified among the most significant groundwater knowledge gaps in Canada (Jarrahi et al. 2019). There is a need to address this gap given the prevalence of these aquifers (e.g., 70% of the regional aquifers in Canada exist in fractured rock formations (Rivera, 2005)), and our increasing reliance on them (Bondu et al. 2018).

The development of accurate transport models in fractured media is based on considering the mechanisms occurring within the fracture itself, as well as interactions between the fracture and surrounding stagnant zones (matrix). The dominant processes within the fracture include advection, dispersion, adsorption, and growth/decay, all of which are described by the classical advection-dispersion equation (ADE). However, solutes may also diffuse into the surrounding matrix (i.e., matrix diffusion) within which adsorption or decay may occur, and which often has large storage capacities.

Several analytical solutions have been developed to simulate solute transport in a single fracture with smooth, parallel plate walls. These models use mechanical dispersion (i.e., resulting from spatial velocity variations and diffusion) to represent spreading caused by the Poiseuille velocity distribution and non-uniform flow (e.g., Bear 1972; Sudicky and Frind 1982; Sudicky and Frind 1984; Houseworth et al. 2013). Bear (1972) developed a simple analytical solution for solute transport in a single fracture with an impermeable matrix. Sudicky and Frind (1982) also developed an analytical solution for solute transport in a single fracture, but considered matrix diffusion. Specifically, their solution considers: i) advective transport along the fracture; ii) longitudinal mechanical dispersion within the fracture; iii) adsorption onto the fracture wall; iv) adsorption

within the matrix; v) first-order decay for a single constituent, vi) molecular diffusion within the fracture along the direction of flow, and vii) molecular diffusion between fracture and porous matrix. Sudicky and Frind (1984) extended the work of Sudicky and Frind (1982) to consider the transport of two constituents subject to first-order decay.

Numerical approaches have also been employed to simulate solute transport in fractures; these models are categorized according to the approach—continuum and discrete fracture network (DFN). The continuum approach assumes that the fracture network scale and connectivity characteristics are such that the network can be approximated by a continuum. The DFN approach requires an explicit representation of the system, including: i) the fractures as discrete attributes with flow-carrying abilities, and, ii) the matrix with significant storage capacity (Long et al., 1982). While the DFN approach typically yields more accurate results since it considers the geometric complexity of the system (Cacas et al. 1990; Park et al. 2001; Frampton and Cvetkovic 2010, 2011; De Dreuzy, Méheust, and Pichot 2012; Lang, Paluszny, and Zimmerman 2014; Hyman et al. 2015, 2016; Maillot et al. 2016; Somogyvári et al. 2017), the computational costs are extensive due to the large number of input parameters required to describe the properties of each fracture and intersection in the network. Additionally, specific geometries and fracture properties are rarely known in field-scale problems.

To overcome this issue, different numerical approaches are commonly used to solve the ADE in fractures, including Eulerian, or grid-based, and Lagrangian, or particle tracking. The most common Lagrangian approach is the random walk particle tracking (RWPT) method, which

represents the solute mass with a large number of particles. At each time step, each particle experiences different displacements comprised of a deterministic component (representing advection) and a stochastic component (representing dispersion). The number of particles used controls the accuracy of the solution, where an infinite number of particles results in the solution of the ADE. The time steps must be small enough such that the velocity and dispersion coefficients do not change significantly in consecutive time steps. The other common Lagrangian approach is the time domain random-walk (TDRW) method that was inspired by the Random Walk method. The TDRW method calculates the solute breakthrough curve (BTC) at a given point based on the difference in residence times of each particle within the fracture (Cvetkovic et al. 2014; Bodin 2015; Roubinet et al. 2017). Trinchero et al. (2020) presented a flexible algorithm based on TDRW to simulate solute transport in single fractures with diffusion into stagnant zones and the surrounding matrix. This algorithm is based on a stepwise Monte Carlo sampling that first samples the particle retention in the fracture conditioned with a related hydrodynamic control parameter. Second, it defines the total time in the rock matrix conditioned with a transport resistance value that accounts for the total time in fracture. Their approach is based on precomputed retention time distributions stored in look-up tables. At the network scale, Bodin et al. (2003) presented a numerical solution using the time domain random walk (TDRW) method in discrete fracture networks. Their solution is based on representing the fracture network by a set of parallel (elementary) paths for the transport of solute particles. The solution incorporates advection, longitudinal dispersion, sorption, and first-order decay, and was shown to be accurate at Peclet numbers up to 10, but inaccurate beyond this. Khafagy et al. (2020) implemented a 2D solution of

a DFN using RWPT to simulate matrix diffusion and reactive processes along the fracture walls and within the matrix. Their solution implemented matrix diffusion using particle transfer probabilities between the fracture and the matrix developed by Pan and Bodvarsson (2002) and Pan et al. (2005).

The aforementioned random walk-based models are computationally intensive, particularly when matrix diffusion, adsorption, and decay are considered, as they require the release of a large number of particles to achieve accurate results. While accurate solutions under these conditions can be obtained using analytical methods, which are much less computationally intensive, these solutions are only available at the scale of a single fracture. To date, no analytical modeling scheme that includes both connectivity between fractures and their surrounding matrix has been reported in the literature. Furthermore, few numerical fracture network models have employed the transfer function approach (i.e., Bodin et al. 2003; Frampton and Cvetkovic 2011; Cherubini, Giasi, and Pastore 2014). This involves spitting the network into all possible elementary solute pathways to express solute transferred along each pathway (e.g., Bodin et al. 2003). However, this approach is only able to predict the breakthrough curve at the fracture outlet; it cannot provide the spatial distribution of solute within the network. Therefore, the goal of the current study is to develop an analytical network model (AN) for reactive solute transport in a two-dimensional fracture network that is able to predict both the effluent concentration profile and the spatial distribution of solute in the fracture network and surrounding matrix. The AN considers any fracture spacing and incorporates advection, mechanical dispersion, molecular diffusion within the fracture and into the matrix, adsorption on the fracture walls and within the matrix, and first-order decay.

## 2.2. Model Development

The 2D AN model for fracture networks developed in this work is based on two analytical solutions for solute transport in a single, parallel plate fracture. Single fractures are assembled to form a network, and mass is partitioned at the intersections. The transfer function approach is applied to calculate the BTC on the downstream side of each intersection using mass sharing at the intersection as the inlet boundary condition.

The AN model considers advection, hydrodynamic dispersion, sorption, radioactive decay, and matrix diffusion (**Fig. 2-1**), or a combination of these, and therefore implements two previously developed analytical solutions for solute transport in 1D fractures i.e., Bear (1972), and Sudicky and Frind (1982). Although both of these solutions consider the same transport mechanisms, the Sudicky and Frind (1982) solution requires the implementation of matrix diffusion while the Bear (1972) solution cannot simulate matrix diffusion. The relevant transport processes in a 1D fracture-matrix system are described by two differential equations, describing the fracture and the matrix, respectively, coupled as follows:

$$\frac{\partial c}{\partial t} + \frac{v}{R} \frac{\partial c}{\partial z} - \frac{D}{R} \frac{\partial^2 c}{\partial z^2} + \lambda c - \frac{\theta D'}{bR} \frac{\partial c'}{\partial x} \Big|_{x=b} = 0 \quad (2-1)$$

where  $z$  [L] is the fracture length,  $x$  [L] is the coordinate perpendicular to the fracture axis with the origin at the centerline of the fracture [L],  $v$  [L/T] is groundwater velocity in the fracture, which can be impacted by fracture orientation,  $2b$  [L] is the aperture width,  $D$  [L<sup>2</sup>/T] is the hydrodynamic dispersion coefficient along the fracture,  $D'$  [L<sup>2</sup>/T] is the diffusion coefficient in the porous matrix,

$R$  [-] is the retardation coefficient,  $\theta$  [-] is the matrix porosity,  $t$  [T] is the time, and  $\lambda$  [ $T^{-1}$ ] is the first-order decay constant defined as:

$$\lambda = \frac{\ln 2}{t_{1/2}} \quad (2-2)$$

where  $t_{1/2}$  [T] is the half-life of the solute.

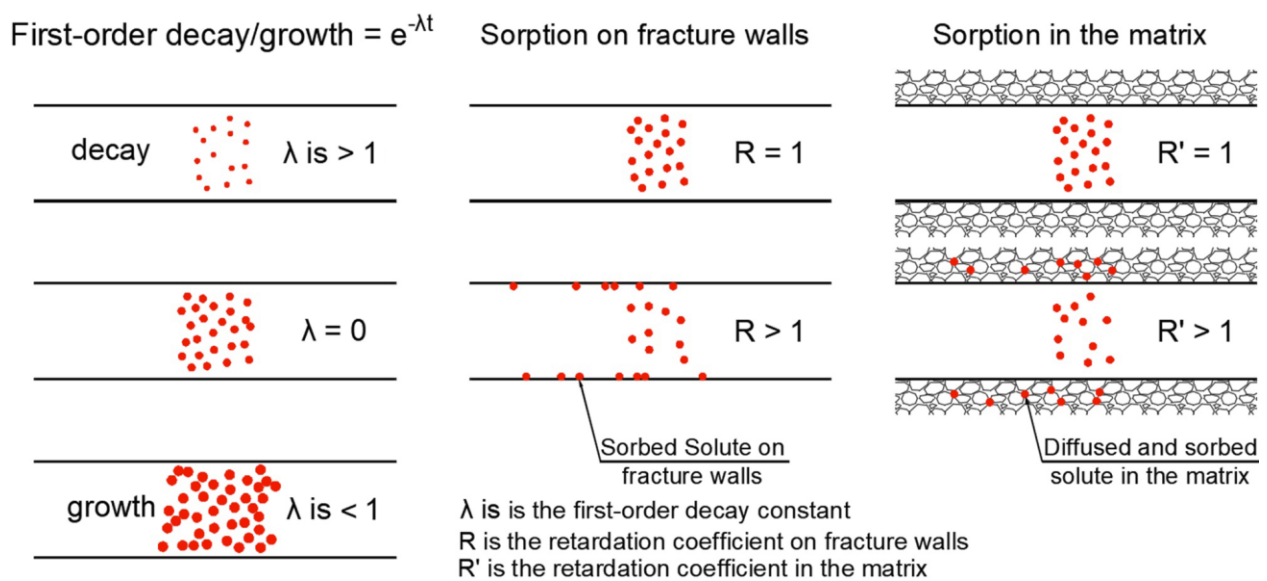


**Fig. 2-1: Schematic of a single fracture illustrating the solute growth/decay and sorption processes.**

Bear (1972) and Sudicky and Frind (1982) proposed analytical solutions to **Eq. (2-1)**. The details of the two analytical solutions are given in Appendix A. While the BTC resulting from Sudicky and Frind (1982) solution (**Eq. (A.1.3)**) is based on a constant concentration at the inlet boundary (Type 1), the resulting BTC must be converted to an equivalent discrete curve with an

instantaneous injection at the inlet boundary (Type 2) in order to apply the solute mass transfer approach in each fracture. This is achieved by numerically differentiating the resulting BTC as follows:

$$C_I = \frac{\partial C_C}{\partial t} \times dt \quad (2-3)$$

where  $C_I$  [M/L<sup>3</sup>] is the concentration from the instantaneous injection BTC and  $C_C$  [M/L<sup>3</sup>] is the concentration from the constant concentration BTC. The resulting BTC gives the solute concentration relative to its initial concentration. To solve solute transport as a function of mass concentration rather than mass injected, the discrete BTC obtained from Bear (1972) solution (**Eq. (A.1.1)**) is modified based on the relationship between the one-dimensional mass flux due to advection and the initial concentration (Fetter et al. 2018):

$$F_x = v \theta_f C_o \quad (2-4)$$

where  $F_x$  [M/L<sup>2</sup> · T] is defined as the mass flux, and  $\theta_f$  [-] is the porosity within the fracture (i.e., 1). The solution developed by Bear (1972) (**Eq. (A.1.1)**) can then be modified to solve solute transport as a function of the relative concentration based on **Eq. (2-4)**:

$$\frac{C}{C_o} = \frac{z}{\sqrt{4\pi \frac{D}{R} t^3}} \exp\left(-\frac{\left(z - \frac{v}{R} t\right)^2}{4 \frac{D}{R} t}\right) \exp(-\lambda t) \quad (2-5)$$

**Eq. (2-5)** gives the effluent BTC based on an instantaneous injection at inlet boundary, and can be converted to give the effluent BTC based on Type 1 boundary condition using **Eq. (2-3)**.

The solute mass sharing at intersections is calculated using both the complete mixing (CM) method developed by Smith and Schwartz (1984) and the stream tube (ST) method developed by Endo et al. (1984). The CM method assumes that the residence time at the intersection is sufficient to allow spatial homogenization through molecular diffusion, and therefore solute concentrations in the downstream fractures are proportional to their discharges (**Fig. 2-2a**). Mass conservation at an intersection is calculated by:

$$\sum_{i=1}^N C_i Q_i = \sum_{j=1}^M C_j Q_j \quad (2-6)$$

where the subscripts  $i$  and  $j$  represent the upstream and downstream fractures, respectively,  $N$  and  $M$  represent the number of upstream and downstream fractures, respectively, and  $Q_j$  is the discharge in the downstream fracture  $j$ . The percent of the solute mass entering each downstream fracture is determined as follows:

$$P_k = \frac{Q_k}{\sum_{j=1}^M Q_j} \quad (2-7)$$

where  $P_k$  is the percent of solute mass from the upstream intersection entering a downstream fracture  $k$ .

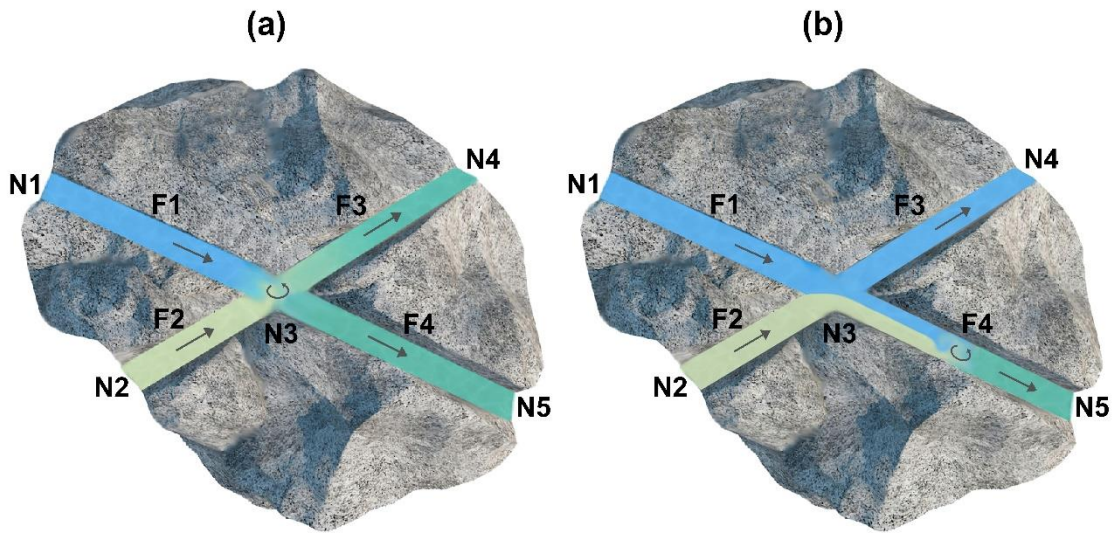


**Fig. 2-2: Schematic diagram illustrating mixing at intersections within a fracture network for (a) the CM method; and (b) the ST method.**

The ST method assumes that solute flows along streamlines into the downstream fractures, and the solution is homogenized within the downstream fracture through forced mixing (**Fig. 2-2b**). At the intersection, the solute is divided based on the mass percentage of the relative discharge between the upstream and downstream fractures:

$$\text{If } Q_i \leq Q_j \begin{cases} P_{ij} = 1 \\ P_{ik} = 0 \end{cases} \quad (2-8a)$$

$$\text{If } Q_i > Q_j \begin{cases} P_{ij} = \frac{Q_j}{Q_i} \\ P_{ik} = \frac{Q_i - Q_j}{Q_i} \end{cases} \quad (2-8b)$$

where  $P_{ij}$  is the mass percentage from an upstream fracture  $i$  entering its contiguous downstream fracture  $j$ ,  $P_{ik}$  is the mass percentage from an upstream fracture  $i$  entering the other downstream fracture  $k$ , and  $Q_i$  is the discharge through the upstream fracture  $i$ .

The BTC at each upstream intersection is divided among the downstream fractures based on their corresponding mass percentage to calculate the influent concentration BTC for each downstream fracture. The final effluent BTC for the downstream fracture is then determined by numerically applying a transfer function approach between influent concentration BTCs (as calculated via mass sharing at the intersection) and the mass transfer probability of reaching the fracture outlet based on the pulse injection:

$$C_{final}(t) = (C_1 * C_2)(t) = \int_0^t C_1(\tau) \cdot C_2(t - \tau) d\tau \quad (2-9)$$

where  $C_1$  [M/L<sup>3</sup>] is the solute concentration at the fracture inlet at time  $\tau$ ,  $C_2$  [-] is the mass transfer probability of reaching the fracture outlet shifted by  $t$ , and  $C_{final}(t)$  [M/L<sup>3</sup>] is the solute concentration at the fracture outlet.

The CM and ST mixing approaches were assessed by comparing their network effluent BTCs obtained under a range of Peclet numbers ( $P_e$ ), defined as follows (Zafarani and Detwiler, 2013):

$$P_e = \frac{V^* \sqrt{2b}}{D^*} \quad (2-10)$$

where  $V^*$  [L/T] is the characteristic velocity at the intersection defined as  $\frac{\bar{Q}}{2b}$ ,  $\bar{Q}$  [L<sup>3</sup>/T] is the

average volumetric flow rate of the upstream fractures 1 and 2, and  $\overline{2b}$  [L] is the average upstream aperture size. The network  $P_e$  was taken as the mean  $P_e$  from each intersection.

### 2.3. Model Verification

Results from the AN model simulations are subsequently compared to those from TDRW (Bodin et al. 2003) and RWPT simulations (Khafagy et al. 2020). The TDRW model calculates the residence time of each particle in each fracture within an elementary path. The residence time for each particle in the elementary path is then determined by summing the residence time in each fracture within the path. The details of the TDRW model implementation are included in Supplementary file A. The RWPT model uses transfer probabilities to incorporate matrix diffusion and reactive processes between the aqueous and sorbed phases. The details of the RWPT model implementation are included in Supplementary file B.

The efficiency of the developed AN model was demonstrated using two synthetic fracture networks. The first network, FN1, was presented by Bodin et al. (2003), and sits within a 350 m x 350 m square domain (**Fig. 2-3a**). It includes 123 fractures with two different orientations; 77 fractures are hydraulically active and 46 are dead-end fractures. There is a 1 m head difference between the west and east boundaries, with flow from west to east. The north and south boundaries represent no-flow boundaries. The second network, FN2, has a much higher fracture density and has the same domain size and boundary conditions as FN1 (**Fig. 2-3b**). FN2 was generated using statistical distribution functions based on fracture density, orientation and length, and aperture size. The fracture density is 0.449 m/m<sup>2</sup> and the network contains two equally

distributed orientation sets in the probability density –  $(40^\circ - 50^\circ)$  and  $(130^\circ - 140^\circ)$ . There are 12,884 hydraulically active fractures and 199 dead-end fractures in FN2.

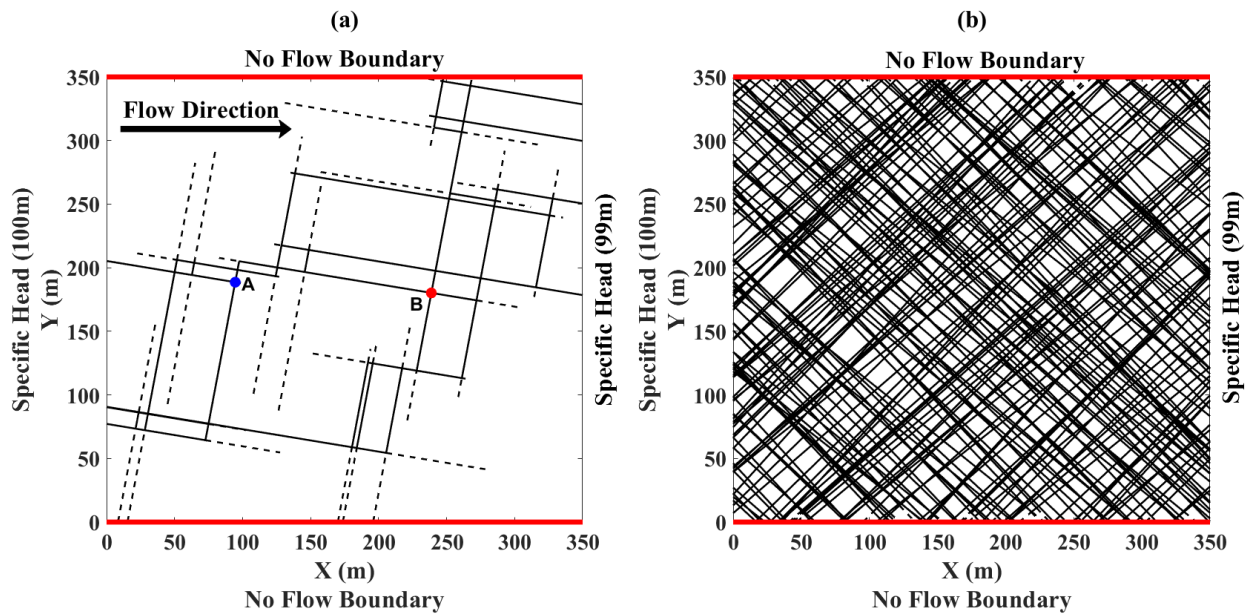


**Fig. 2-3: Synthetic fracture networks for model verification. Solid lines represent hydraulically active fractures, while dashed lines represent dead-end fractures.**

Three verification cases were run, each with different transport processes (**Table 2-1**). The TDRW model was used to verify cases 1 and 2 since it can simulate decay, while the RWPT model was used to verify case 3 since it can simulate matrix diffusion. In all three cases, the solute was injected along the west boundary using a constant injection boundary condition, and the solute mass was divided between the inlet fractures based on the proportion of total flow, which was calculated using the cubic law. **Table 2-1** shows the fracture network properties used in each verification

case. There were 10,000 particles released in the numerical simulations for the FN1 and 100,000 particles released in FN2, as more particles are required due to the higher fracture density in FN2. In Case 3, the flowrate range is  $6 \times 10^{-10} - 4 \times 10^{-8} \text{ m}^3/\text{sec}$  resulting in the  $P_e$  at the intersections ranging from 0.6 to 38 ( $\bar{P}_e = 18$ ).

**Table 2-1: Properties of the DFN for the cases used in the verification.**

Case	$\alpha$ (m)	$2b$ (m)	$2B$ (m)	$D^*$ (m <sup>2</sup> /sec)	$t_{1/2}$ (day)	$R$	$R'$	$\theta_m$	$\tau$	Mass Sharing Method	FN
1	1	0.00025	n/a	0	n/a	1, 4	0	0	n/a	CM, ST	1, 2
2			n/a	0	20, 40	1	0	0	n/a	CM, ST	1
3			1	$1 \times 10^{-9}$	n/a	1	1, 2, 3, 4	0.1	0.25	CM	1

## 2.4. Results and Discussion

The effluent BTCs calculated by the AN model for Case 1 (**Table 2-1**) and a Type 1 boundary condition are plotted against those obtained from the TDRW model for both FN1 and FN2 (**Fig. 2-4a** and **Fig. 2-4b**, respectively). The AN model results presented in **Fig. 2-4** were calculated using both the CM and ST mass sharing methods. The results show excellent agreement between the AN model and the TDRW model for both FN1 and FN2. In FN1, the CM approach results in

slightly higher dispersion, with the solute mass reaching the east boundary approximately 15% earlier. The higher dispersion calculated by the CM method is due to the assumption of complete mixing within the intersection. This is in contrast to the ST method in which mass advects along streamlines and mixing occurs within the downstream fractures resulting in less dispersion. It is noteworthy that this phenomenon is not observable in FN2 as the large number of intersections in this network have a smoothing effect on dispersion.

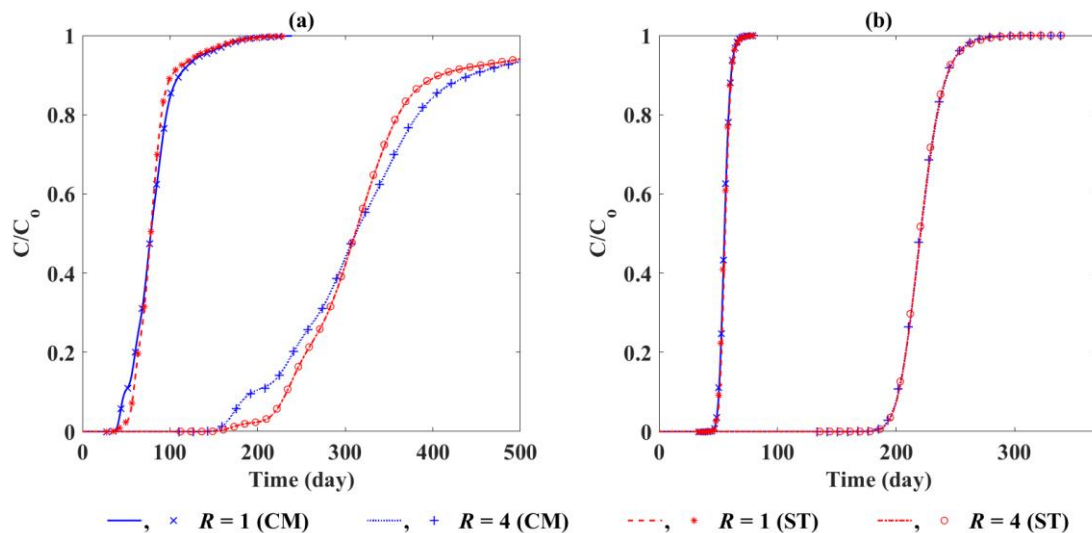


**Fig. 2-4: BTCs for Case 1 ( $t_{1/2} = n/a$ ;  $R = 1$  or  $4$ ;  $\theta = 0$ ;  $D^* = 0 \text{ m}^2/\text{sec}$ ) calculated using both CN and ST mass sharing methods in (a) FN1, and (b) FN2 with a Type 1 boundary condition. Lines represent and symbols represent AN and TDRW model simulations, respectively.**

The effluent BTCs calculated by the AN model for Case 2 (**Table 2-1**) and a Type 1 boundary condition in FN1 are plotted against those obtained from the TDRW model in **Fig. 2-5** for both the CM and ST methods of mass sharing at the intersections. These results highlight the impact of decay, and show excellent agreement between the AN and TDRW models for the range of half-lives investigated. Similar to Case 1, these results show that the CM method results in slightly higher dispersion than the ST method, with arrival times approximately 15% earlier. Additionally, the ST method results in more decay than the CM method for solutes with the same half-life, resulting in approximately 9% less mass reaching the east boundary for  $t_{1/2} = 20$  days. This discrepancy decreases as  $t_{1/2}$  increases, with approximately 2% less mass reaching the east boundary at  $t_{1/2} = 40$  days. This is likely a result of the later arrival times associated with the ST method, allowing the solute more opportunity to decay.

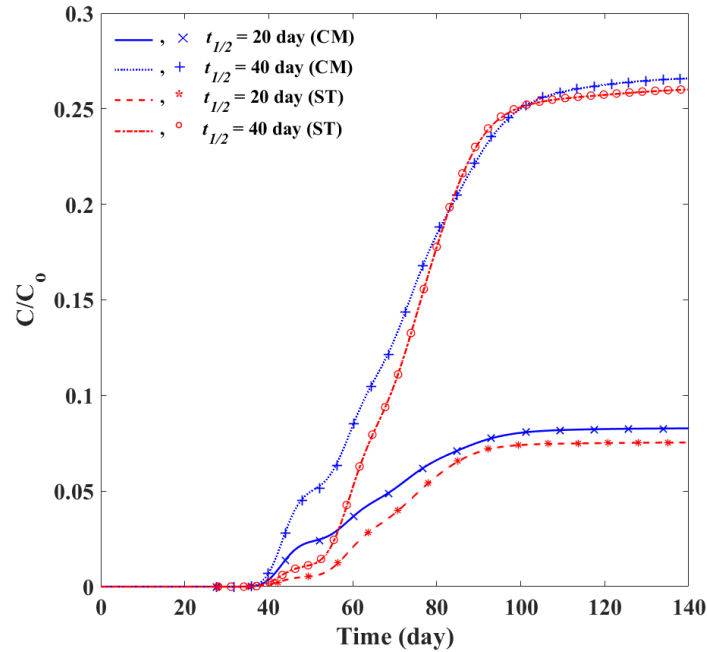


**Fig. 2-5: BTCs for Case 2 ( $t_{1/2} = 20$  or 40 days;  $R = 1$ ;  $\theta = 0$ ;  $D^* = 0$  m<sup>2</sup>/sec) calculated using both CM and ST mass sharing methods in FN1 with a Type 1 boundary condition.**

**Lines represent AN model and symbols represent TDRW model.**

The effluent BTCs calculated by the AN model for Case 3 (**Table 2-1**) and a Type 1 boundary condition in FN1 are plotted against those obtained from the RWPT model in **Fig. 2-6** using the CM method of mass sharing at the intersections. The flowrate range is  $6 \times 10^{-10} - 4 \times 10^{-8}$  m<sup>3</sup>/sec resulting in the  $P_e$  at the intersections ranging from 0.6 to 38 ( $\bar{P}_e = 18$ ). These results highlight the impacts of matrix diffusion and retardation within the matrix and show excellent agreement between the AN and RWPT models.

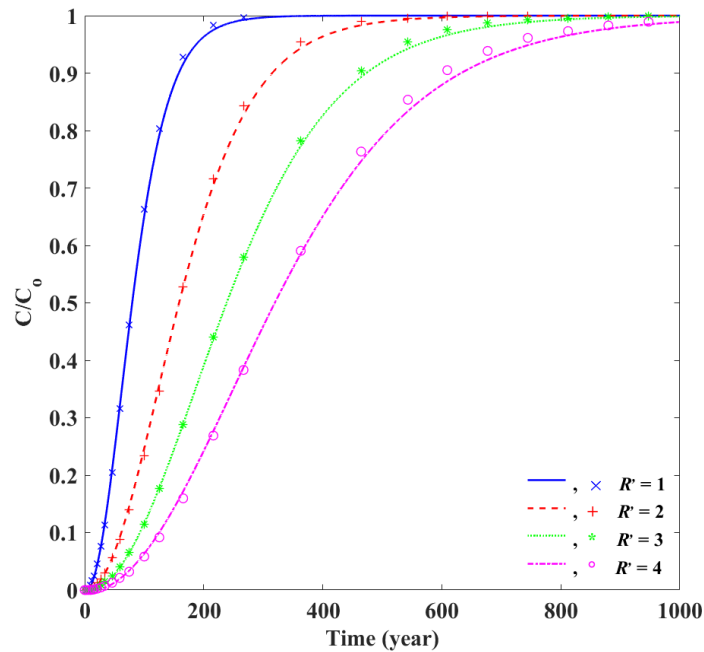


**Fig. 2-6: BTCs for Case 3 ( $t_{1/2} = n/a$ ;  $R = 1$ ;  $\theta = 0.1$ ;  $D^* = 1 \times 10^{-9} \text{ m}^2/\text{sec}$ ) calculated using the CM mass sharing method in FN1 with a Type 1 boundary condition, and  $\overline{P_e} = 18$  at the network intersections. Lines and symbols represent AN and RWPT model simulations, respectively.**

The AN model is able to calculate the complete spatial and temporal distribution of mass in the fracture network. The BTCs calculated by the AN model in FN1 at intersections A and B are shown in **Fig. 2-7** for Case 1 with a conservative tracer (**Table 2-1**), using the CM method of mass sharing at intersections, for both Type 1 and Type 2 boundary conditions. Two solute peaks are observed at both intersection A and B as each of these intersections have multiple upstream solute transport pathways. Additionally, intersection A experiences earlier mass arrival and a higher peak

concentration than intersection B. This is expected as dispersion increases with travel time and distance, and intersection B is located downstream of A; thus, the solute has experienced more dispersion by the time it arrives at B.

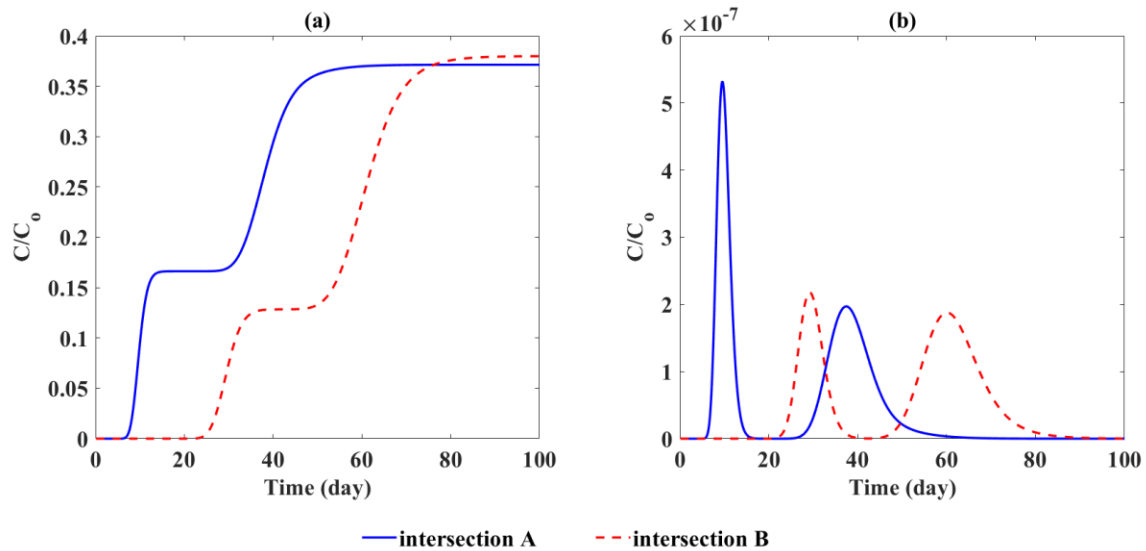


**Fig. 2-7: BTCs calculated for Case 1 ( $t_{1/2} = n/a$ ;  $R = 1$ ;  $\theta = 0$ ;  $D^* = 0$  m<sup>2</sup>/sec) by the AN model at intersections A and B (see Fig. 2-3) using the CM mass sharing method in FN1 for (a) Type 1 and (b) Type 2 boundary conditions.**

The impact of  $P_e$  on the mass sharing method applied at the intersections was investigated for a conservative tracer in FN1 under a Type 2 boundary condition both considering and excluding matrix diffusion (**Fig. 2-8**). At the low range,  $P_e$  was varied between  $3 \times 10^{-6} - 2 \times 10^{-4}$  at the intersections ( $\bar{P}_e = 9 \times 10^{-5}$ ) by changing  $Q$  ( $3 \times 10^{-13} - 2 \times 10^{-11}$  m<sup>3</sup>/sec) such that the ratio ( $D/D^*$ ) approached 1.0 (1 – 1.8;  $D^* = 1 \times 10^{-7}$  m<sup>2</sup>/sec) to ensure that diffusion dominated over

advection. When diffusion dominates (i.e.,  $P_e$  is small), the mass sharing method impacts the shape of the BTC regardless of the presence of matrix diffusion (**Fig. 2-8a, b**). Similar to case 1, the CM method produces slightly higher dispersion than the ST method and thus earlier arrival times and lower peak concentrations (for a pulse injection). These results support those of (Mourzenko et al., 2002) who investigated the applicability of the CM and ST mass sharing methods at a single intersection for a range of  $P_e$  in the absence of matrix diffusion. They also found differences between predictions based on the CM and ST mass sharing methods at low  $P_e$ , and concluded that the CM method is more accurate under these conditions. At the high range,  $P_e$  was varied between 6 – 380 at the intersections ( $\bar{P}_e = 178$ ) by changing  $Q$  ( $6 \times 10^{-10} - 4 \times 10^{-8} \text{ m}^3/\text{sec}$ ) such that the ratio ( $D/D^*$ ) was much larger than 1.0 ( $2.5 \times 10^4 - 1.5 \times 10^6$ ,  $D^* = 1 \times 10^{-10} \text{ m}^2/\text{sec}$ ) to ensure that advection dominates over diffusion. When advection dominates (i.e.,  $P_e$  is high), the CM method causes slightly more dispersion than the ST method (**Fig. 2-8c**), but not to the degree that it does at low values of  $P_e$  (i.e., **Fig. 2-7a**). Note that the differences between the BTCs in **Fig. 2-8c** are also a result of different solute transport pathways associated with the CM and ST mass sharing methods due to the differences in mass distribution at the intersections. These results also agree with those of (Mourzenko et al., 2002) who also observed significant differences between the CM and ST mass sharing methods at high  $P_e$ , and concluded that the ST method is more appropriate under these conditions. When matrix diffusion is considered at high  $P_e$  (**Fig. 2-8d**), the impact of the mass sharing method on dispersion is more pronounced at early times (i.e., rising limb) when the mass has primarily experienced advection within the fractures; however, this difference is dampened over time as a result of matrix diffusion.

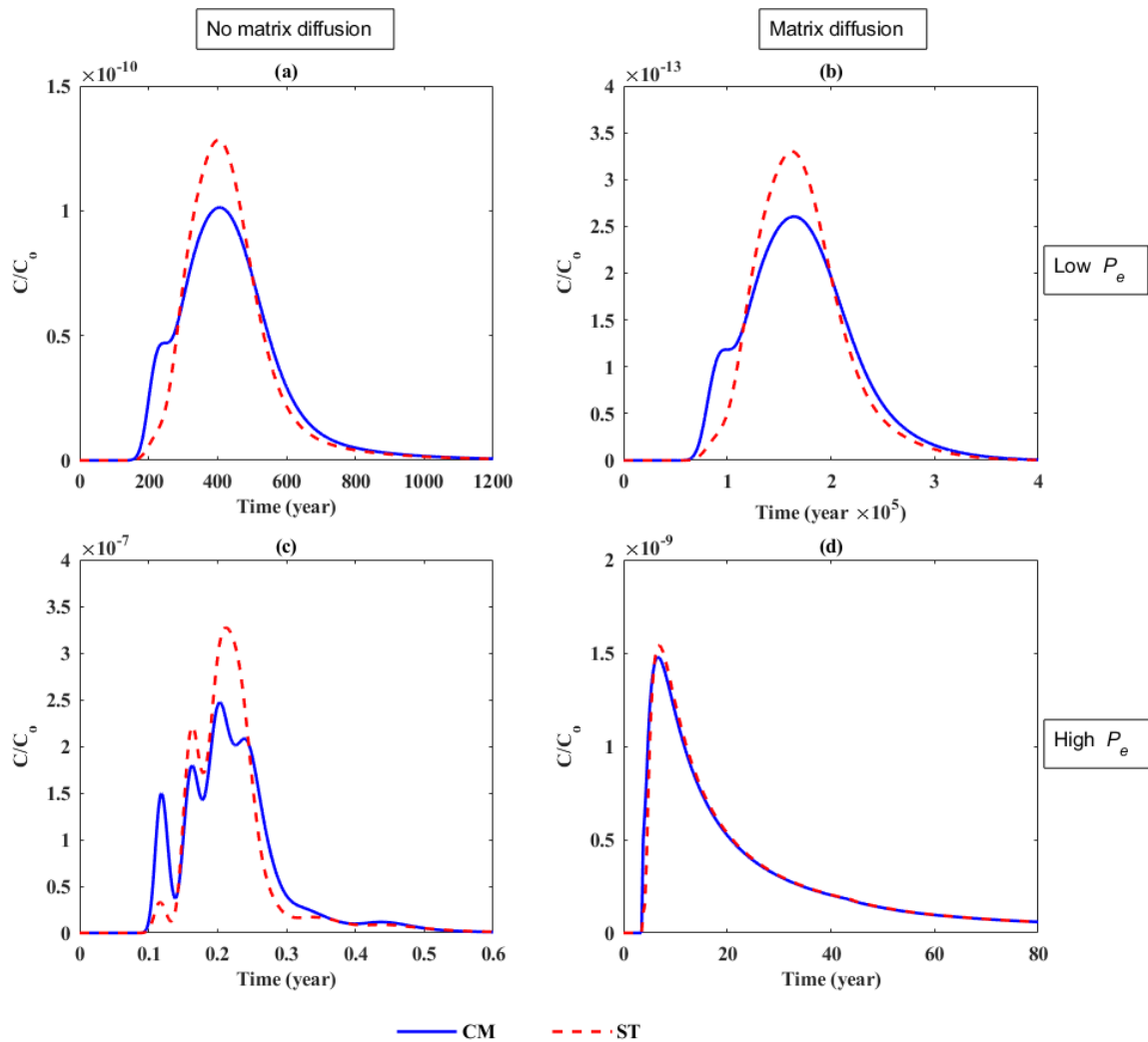


**Fig. 2-8: BTCs calculated using the AN model for Case 1 ( $t_{1/2} = n/a$ ;  $R = 1$ ;  $\theta = 0.1$ ;  $D^* = 1 \times 10^{-7}$  or  $1 \times 10^{-10} \text{ m}^2/\text{sec}$ ) using both the CM and ST mass sharing methods in FN1 based on a Type 2 boundary conditions for (a) no matrix diffusion and  $\overline{P_e} = 9 \times 10^{-5}$  at the intersections, (b) matrix diffusion and  $\overline{P_e} = 9 \times 10^{-5}$  at the intersections, (c) no matrix diffusion and  $\overline{P_e} = 178$  at the intersections, and (d) matrix diffusion and  $\overline{P_e} = 178$  at the intersections.**

The impact of the number of particles released on the convergence of the TDRW and RWPT models was investigated by comparing the effluent BTCs simulated by the AN model (Cases 1 and 3 without adsorption (**Table 2-1**)) in FN1 against those obtained from the TDRW (Type 2 boundary condition; CM mass sharing) and RWPT (Type 1 boundary condition; CM mass sharing) models with 10,000, 100,000, and 500,000 particles released (**Fig. 2-9**). The results show that, even in FN1 which is a relatively simple network, 10,000 particles are not sufficient to converge on the solution accurately. Note that the network and individual fracture parameters and conditions for the simulation shown in **Fig. 2-9a** are the same as those used by Bodin et al., (2003).

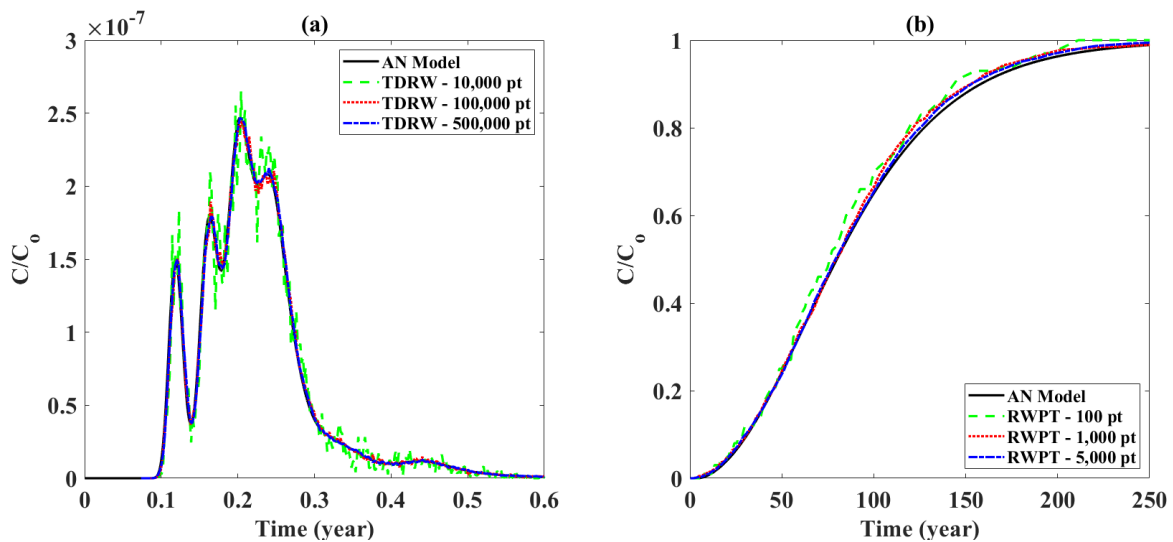


**Fig. 2-9: BTCs calculated using the CM mass sharing method in FN1 comparing AN simulations to TDRW and RWPT simulations with different numbers of particles released for (a) Case 1 with a Type 2 boundary condition ( $t_{1/2} = n/a$ ;  $R = 1$ ;  $\theta = 0$ ;  $D^* = 0 \text{ m}^2/\text{sec}$ ) and (b) Case 3 with a Type 1 boundary condition ( $t_{1/2} = n/a$ ;  $R = 1$ ;  $R' = 1$ ;  $\theta = 0.1$ ;  $D^* = 1 \times 10^{-9} \text{ m}^2/\text{sec}$ ).**

The AN model arrived at a solution in approximately 1% and 3% of the time required for FN1 to arrive at solutions using the TDRW (disregarding matrix diffusion with 500,000 particles) and RWPT approaches (including matrix diffusion with 5,000 particles), respectively. This emphasizes the computational efficiency of the AN model, which will become more pronounced as the complexity of the fracture network increases and more solute particles are required for accurate results using the TDRW and RWPT approaches.

## **2.5. Conclusion**

An analytical network (AN) model is developed to simulate solute transport in two-dimensional fracture networks considering advection and dispersion within the fracture, sorption on the fracture walls and within the matrix, matrix diffusion, and first-order decay. Mass sharing at intersections was handled using both the complete mixing (CM) and stream-tube (ST) methods, and the performance of these methods was compared under a range of  $P_e$ . The transfer function approach was applied to calculate solute transport in each fracture using the output from the mass sharing scheme as the upstream boundary condition. The AN model enables calculation of the complete spatial and temporal distribution of mass in the fracture network, and therefore a useful application is the simulation of transport behavior at multiple locations in heterogeneous fractured rock aquifers. Additionally, the AN model is the only analytical network model that considers fracture-matrix interactions and can therefore be a useful reference model for the verification of numerical solutions in dual porosity systems.

The AN model performed well when compared with simulations from TDRW and RWPT-based

numerical models in two different fracture networks – one with a high fracture density and one with a lower fracture density. The CM method results in slightly higher dispersion than the ST approach for the network with low fracture density due to the assumption of complete mixing at the intersection. While this phenomenon occurs consistently at each intersection, it is not observable in the densely fractured network as the large number of intersections in this network has a smoothing effect on dispersion. The ST mass sharing method results in more decay than the CM method for solutes with the same half-life. This is likely a result of the later arrival times associated with the ST method, allowing the solute more opportunity to decay.

It was also found that when  $P_e$  is small, the mass sharing method impacts the shape of the BTC regardless of the presence of matrix diffusion, with the CM method producing higher dispersion than the ST method. This result was also observed at high values of  $P_e$  in the absence of matrix diffusion, although the differences between the CM and ST BTCs is less pronounced under these conditions. When matrix diffusion is considered at high  $P_e$ , the increased dispersion caused by the CM approach is only observable at early times, as the effect is dampened by matrix diffusion.

Finally, the developed AN model arrived at a solution in FN1 network in less than 1% and 3% of the time required for the TDRW (without matrix diffusion) and RWPT (with matrix diffusion) approaches, respectively, emphasizing the computational efficiency of the AN model. The impact of this efficiency will become more apparent in larger, more complex networks.

## **2.6. Acknowledgment**

The financial support for the study was provided through the CaNRisk-CREATE program of the Natural Science and Engineering Research Council (NSERC) of Canada (Grant Number: CREAT-482707-2016).

## 2.7. References

- Ahmad, K., Zhao, X., & Pan, Y. (2017). Effect of surface morphology on measurement and interpretation of boundary slip on superhydrophobic surfaces. *Surface and Interface Analysis*, 49(7), 594–598. <https://doi.org/10.1002/sia.6197>
- Bear, J. (1972). *Dynamics of Fluids in Porous Media*. New York, Dover Publications, 1–783.
- Bechtold, M., Vanderborght, J., Ippisch, O., & Vereecken, H. (2011). Efficient random walk particle tracking algorithm for advective-dispersive transport in media with discontinuous dispersion coefficients and water contents. *Water Resources Research*, 47(10), 1–20. <https://doi.org/10.1029/2010WR010267>
- Bishop, P., Persaud, E., Levison, J., Parker, B., & Novakowski, K. (2020). Inferring flow pathways between bedrock boreholes using the hydraulic response to borehole liner installation. *Journal of Hydrology*, 580(May 2019), 124267. <https://doi.org/10.1016/j.jhydrol.2019.124267>
- Bodin, J. (2015). From analytical solutions of solute transport equations to multidimensional time-domain random walk (TDRW) algorithms. *Water Resources Research*, 51(3), 1860–1871. <https://doi.org/10.1002/2014WR015910>

- Bodin, J., Porel, G., & Delay, F. (2003). Simulation of solute transport in discrete fracture networks using the time domain random walk method. *Earth and Planetary Science Letters*, 208(3–4), 297–304. [https://doi.org/10.1016/S0012-821X\(03\)00052-9](https://doi.org/10.1016/S0012-821X(03)00052-9)
- Bondu, R., Cloutier, V., & Rosa, E. (2018). Occurrence of geogenic contaminants in private wells from a crystalline bedrock aquifer in western Quebec, Canada: Geochemical sources and health risks. *Journal of Hydrology*, 559, 627–637. <https://doi.org/10.1016/j.jhydrol.2018.02.042>
- Bondu, R., Cloutier, V., Rosa, E., & Benzaazoua, M. (2016). A Review and Evaluation of the Impacts of Climate Change on Geogenic Arsenic in Groundwater from Fractured Bedrock Aquifers. *Water, Air, and Soil Pollution*, 227(9). <https://doi.org/10.1007/s11270-016-2936-6>
- Cacas, M. C., Ledoux, E., de Marsily, G., Barbreau, A., Calmels, P., Gaillard, B., & Margritta, R. (1990). Modeling fracture flow with a stochastic discrete fracture network: Calibration and validation: 2. The transport model. *Water Resources Research*, 26(3), 491–500. <https://doi.org/10.1029/WR026i003p00491>
- Cherubini, C., Giasi, C. I., & Pastore, N. (2014). On the reliability of analytical models to predict solute transport in a fracture network. *Hydrology and Earth System Sciences*, 18(6), 2359–2374. <https://doi.org/10.5194/hess-18-2359-2014>

- Cvetkovic, V., Fiori, A., & Dagan, G. (2014). Solute transport in aquifers of arbitrary variability: A time-domain random walk formulation. *Water Resources Research*, 50(7), 5759–5773. <https://doi.org/10.1002/2014WR015449>
- De Dreuzy, J. R., Méheust, Y., & Pichot, G. (2012). Influence of fracture scale heterogeneity on the flow properties of three-dimensional discrete fracture networks (DFN). *Journal of Geophysical Research B: Solid Earth*, 117(11), 1–21. <https://doi.org/10.1029/2012JB009461>
- Dippenaar, M. A., van Rooy, J. L., & Diamond, R. E. (2019). Engineering, hydrogeological and vadose zone hydrological aspects of Proterozoic dolomites (South Africa). *Journal of African Earth Sciences*, 150(January 2018), 511–521. <https://doi.org/10.1016/j.jafrearsci.2018.07.024>
- Döring, S. (2020). Come rain, or come wells: How access to groundwater affects communal violence. *Political Geography*, 76(September 2019), 102073. <https://doi.org/10.1016/j.polgeo.2019.102073>
- Endo, H. K., Long, J. C. S., Wilson, C. R., & Witherspoon, P. A. (1984). A Model for Investigating Mechanical Transport in Fracture Networks. *Water Resources Research*, 20(10), 1390–1400. <https://doi.org/10.1029/WR020i010p01390>
- Fetter, C. W., Boving, T., & Kreamer, D. (2018). *Contaminant Hydrogeology*. <https://linkinghub.elsevier.com/retrieve/pii/001670379390162P>

Frampton, A., & Cvetkovic, V. (2010). Inference of field-scale fracture transmissivities in crystalline rock using flow log measurements. *Water Resources Research*, 46(11), 1–17. <https://doi.org/10.1029/2009WR008367>

Frampton, A., & Cvetkovic, V. (2011). Numerical and analytical modeling of advective travel times in realistic three-dimensional fracture networks. *Water Resources Research*, 47(2), 1–16. <https://doi.org/10.1029/2010WR009290>

Frampton, A., Hyman, J. D., & Zou, L. (2019). Advective Transport in Discrete Fracture Networks With Connected and Disconnected Textures Representing Internal Aperture Variability. *Water Resources Research*, 55(7), 5487–5501. <https://doi.org/10.1029/2018WR024322>

Freeze, R. A., & Cherry, J. A. (1980). Groundwater. In *Journal of Hydrology* (Vol. 47, Issues 1–2). [https://doi.org/10.1016/0022-1694\(80\)90057-8](https://doi.org/10.1016/0022-1694(80)90057-8)

Gentili, D., Bolognesi, G., Giacomello, A., Chinappi, M., & Casciola, C. M. (2014). Pressure effects on water slippage over silane-coated rough surfaces: Pillars and holes. *Microfluidics and Nanofluidics*, 16(6), 1009–1018. <https://doi.org/10.1007/s10404-014-1376-0>

Houseworth, J. E., Asahina, D., & Birkholzer, J. T. (2013). An analytical model for solute transport through a water-saturated single fracture and permeable rock matrix. *Water Resources Research*, 49(10), 6317–6338. <https://doi.org/10.1002/wrcr.20497>

Hyman, J. D., Aldrich, G., Viswanathan, H., Makedonska, N., & Karra, S. (2016). Fracture size and transmissivity correlations: Implications for transport simulations in sparse three-dimensional discrete fracture networks following a truncated power law distribution of fracture size. *Water Resources Research*, 52(8), 6472–6489. <https://doi.org/10.1002/2016WR018806>

Hyman, Jeffrey D., Karra, S., Makedonska, N., Gable, C. W., Painter, S. L., & Viswanathan, H. S. (2015). DfnWorks: A discrete fracture network framework for modeling subsurface flow and transport. *Computers and Geosciences*, 84, 10–19. <https://doi.org/10.1016/j.cageo.2015.08.001>

Jarrahi, M., Moore, K. R., & Holländer, H. M. (2019). Comparison of solute/heat transport in fractured formations using discrete fracture and equivalent porous media modeling at the reservoir scale. *Physics and Chemistry of the Earth*, 113(July), 14–21. <https://doi.org/10.1016/j.pce.2019.08.001>

Khafagy, M. M., Abd-Elmegeed, M. A., & Hassan, A. E. (2020). Simulation of reactive transport in fractured geologic media using random-walk particle tracking method. *Arabian Journal of Geosciences*, 13(2). <https://doi.org/10.1007/s12517-019-4952-5>

Lang, P. S., Paluszny, A., & Zimmerman, R. W. (2014). Permeability tensor of three-dimensional fractured porous rock and a comparison to trace map predictions. *Journal of Geophysical Research: Solid Earth*, 119(8), 6288–6307. <https://doi.org/10.1002/2014JB011027>

Long, J. C. S., Remer, J. S., Wilson, C. R., & Witherspoon, P. A. (1982). Porous media equivalents for networks of discontinuous fractures. *Water Resources Research*, 18(3), 645–658.  
<https://doi.org/10.1029/WR018i003p00645>

Maillot, J., Davy, P., Le Goc, R., Darcel, C., & de Dreuzy, J. R. (2016). Connectivity, permeability, and channeling in randomly distributed and kinematically defined discrete fracture network models. *Water Resources Research*, 52(11), 8526–8545.  
<https://doi.org/10.1002/2016WR018973>

Marshall, R. E., Levison, J., McBean, E. A., & Parker, B. (2019). Wastewater impacts on groundwater at a fractured sedimentary bedrock site in Ontario, Canada: implications for First Nations' source-water protection. *Hydrogeology Journal*, 27(8), 2739–2753.  
<https://doi.org/10.1007/s10040-019-02019-7>

Mourzenko, V. V., Yousefian, F., Kolbah, B., Thovert, J.-F., & Adler, P. M. (2002). Solute transport at fracture intersections. *Water Resources Research*, 38(1), 1-1-1–14.  
<https://doi.org/10.1029/2000wr000211>

Pan, L., & Bodvarsson, G. S. (2002). Modeling transport in fractured porous media with the random-walk particle method: The transient activity range and the particle transfer probability. *Water Resources Research*, 38(6), 16-1-16–17.  
<https://doi.org/10.1029/2001wr000901>

- Pan, L., Seol, Y., & Bodvarsson, G. S. (2005). Improved estimation of the activity range of particles : The influence of water flow through fracture-matrix interface. Earth Sciences Division, Lawrence Berkeley National Laboratory, Berkeley, CA 94720, USA. <https://www.osti.gov/servlets/purl/882747>
- Park, Y. J., De Dreuzy, J. R., Lee, K. K., & Berkowitz, B. (2001). Transport and intersection mixing in random fracture networks with power law length distributions. *Water Resources Research*, 37(10), 2493–2501. <https://doi.org/10.1029/2000WR000131>
- Rao, K. N., & Latha, P. S. (2019). Groundwater quality assessment using water quality index with a special focus on vulnerable tribal region of Eastern Ghats hard rock terrain, Southern India. *Arabian Journal of Geosciences*, 12(8). <https://doi.org/10.1007/s12517-019-4440-y>
- Rivera, A. (2005). How well do we understand Groundwater in Canada: A Science Case Study. In *Buried Treasure Groundwater Permitting and Pricing in Canada* (Issue 2005030).
- Roubinet, D., Russian, A., Dentz, M., & Gouze, P. (2017). Modeling reactive transport processes in fractured rock using the time domain random walk approach within a dual-porosity framework. *AGU Fall Meeting Abstracts*, 2017, H52A-04.
- Smith, L., & Schwartz, F. W. (1984). An Analysis of the Influence of Fracture Geometry on Mass Transport in Fractured Media. *Water Resources Research*, 20(9), 1241–1252. <https://doi.org/10.1029/WR020i009p01241>

Somogyvári, M., Jalali, M., Jimenez Parras, S., & Bayer, P. (2017). Synthetic fracture network characterization with transdimensional inversion. *Water Resources Research*, 53(6), 5104–5123. <https://doi.org/10.1002/2016WR020293>

Sudicky, E. A., & Frind, E. O. (1982). Contaminant transport in fractured porous media: Analytical solutions for a system of parallel fractures. *Water Resources Research*, 18(6), 1634–1642. <https://doi.org/10.1029/WR018i006p01634>

Sudicky, E. A., & Frind, E. O. (1984). Contaminant Transport in Fractured Porous Media: Analytical Solution for a Two-Member Decay Chain in a Single Fracture. *Water Resources Research*, 20(7), 1021–1029. <https://doi.org/10.1029/WR020i007p01021>

Taylor, G. (1953). Dispersion of soluble matter in solvent flowing slowly through a tube. *Proceedings of the Royal Society of London. Series A. Mathematical and Physical Sciences*, 219(1137), 186–203. <https://doi.org/10.1098/rspa.1953.0139>

Thakur, C. K., Kumari, P., Singh, M. K., & Singh, V. P. (2020). Solute transport model equation for mobile phase in semi-infinite porous media. *Groundwater for Sustainable Development*, 11(January 2019), 100411. <https://doi.org/10.1016/j.gsd.2020.100411>

Trincherro, P., Painter, S. L., Poteri, A., Sanglas, J., Cvetkovic, V., & Selroos, J. O. (2020). A Particle-Based Conditional Sampling Scheme for the Simulation of Transport in Fractured

Rock With Diffusion Into Stagnant Water and Rock Matrix. *Water Resources Research*, 56(4), 1–18. <https://doi.org/10.1029/2019WR026958>

Tsang, C.-F., Neretnieks, I., & Tsang, Y. (2015). Hydrologic issues associated with nuclear waste repositories. *Water Resources Research*, 51(9), 6923–6972. <https://doi.org/10.1002/2015WR017641>

Zafarani, A., & Detwiler, R. L. (2013). Advances in Water Resources An efficient time-domain approach for simulating Pe -dependent transport through fracture intersections. *ADVANCES IN WATER RESOURCES*, 53, 198–207. <https://doi.org/10.1016/j.advwatres.2012.11.011>

Zheng, L., Wang, L., Wang, T., Singh, K., Wang, Z. L., & Chen, X. (2020). Can homogeneous slip boundary condition affect effective dispersion in single fractures with Poiseuille flow? *Journal of Hydrology*, 581(November 2019). <https://doi.org/10.1016/j.jhydrol.2019.124385>

### **Chapter 3: Multi-Gene Genetic Programming Solution for Simulating Solute Transport in Fractures**

This chapter presents an approximate solution of the classical advection-dispersion equation for reactive transport in single, parallel-plate fractures using multi-gene genetic programming approach. The approach is employed to obtain an accurate relationship between the hydraulic, geologic, and chemical parameters of the fracture-matrix system as inputs and an ensemble of breakthrough curves as outputs. This approach is simpler and computationally more efficient than currently adopted methods and therefore it advances solute transport behavior predictions especially when the simulation increases from that of a single fracture to a network.

Authors: M. Khafagy, W. El-Dakhakhni, and S. E. Dickson-Anderson

Journal: Journal of Hydrology

DOI: 10.1016/j.jhydrol.2021.127316

#### **Chapter 3 Contributions:**

Mohamed Khafagy: Conceptualization, Methodology, Software, Formal analysis, Writing, and Original draft preparation.

Sarah Dickson-Anderson: Writing & Review & Editing, Supervision, and Funding acquisition.

Wael El-Dakhakhni: Writing & Review & Editing, Supervision, and Funding acquisition.

## **Abstract**

In lieu of process-based models, evolutionary artificial intelligence techniques can yield accurate expressions describing complex phenomena. In the current study, a closed-form solution is developed to predict solute transport in a fracture-matrix system as a function of the parameters that describe relevant physical and chemical processes. The study adopts a multi-gene genetic programming approach to approximate a solution of the classical advection-dispersion equation for reactive transport in single, parallel-plate fractures. The approach is employed to obtain an accurate relationship between the hydraulic, geological, and chemical parameters of the fracture-matrix system as inputs and an ensemble of breakthrough curves as outputs. Solutions generated by the developed model showed good agreement with those of corresponding analytical and numerical models. Computationally, the developed approach is highly efficient, particularly when compared with the analytical solution, which typically requires relatively fine discretization to calculate the long-tailed breakthrough curves. Therefore, future work could extend the developed model to simulate field-scale networks and include additional and more complex transport phenomena. Thus, this approach advances solute transport behavior predictions through being simpler and computationally more efficient than currently adopted techniques, which is important as the scale of simulation increases from that of a single fracture to a network.

**Keywords:** Closed-form solution, Fractured rock, Matrix diffusion, Multi-Gene genetic programming, Solute transport

### **3.1. Introduction**

Improper handling and disposal of hazardous material have led to the contamination of thousands of aquifers globally, resulting in extensive dissolved plumes and the diffusion of dissolved compounds into low permeability zones (e.g., rock matrix) (Muskus and Falta, 2018). Once a compound enters a low permeability zone, the options for remedial strategies are limited and reverse diffusion results in plume persistence. Dual-porosity models are required to couple the fracture and matrix systems to account for the transfer of groundwater and solute mass between them. Such models are challenging as one source of porosity (i.e., fracture) provides the transmissive path for transport with little storage, and the other (i.e., matrix) provides most of the storage capacity but its conductivity is minimal (Trincherro et al., 2020; Trincherro and Iraola, 2020). Neretnieks (1980) presented an analytical solution for solute transport in dual-porosity systems based on similar solutions for heat transport (Carslaw and Jaeger, 1959), which considers an infinite rock matrix and neglects longitudinal dispersion in the fracture. Subsequently, the solution was generalized by Tang et al. (1981) who implemented in-plane dispersion, and Sudicky and Frind (1982) who considered a finite rock matrix. More recently, other researchers (Cvetkovic, 2010; Mahmoudzadeh et al., 2013; Neretnieks, 2006) extended these analytical solutions through the incorporation of additional mechanisms and phenomena. Neretnieks (2006) developed a mathematical model that accounts for diffusion from the flowing zone into a stagnant layer adjacent to the fracture through which solutes can diffuse into the rock matrix. In addition, they considered reversible diffusion in both the stagnant layer and the matrix. They conceptualized the fractures as both tube-like and slit-like channels, and considered the presence of intersecting

fractures, but they did not consider mixing at fracture intersections. These solutions are useful for modelling solute transport in complex three-dimensional networks that consist of a large number of fractures with different properties and widely varying flow rates. Mahmoudzadeh et al. (2013) extended Neretnieks' (2006) work through exploring various contributions of the matrix and stagnant layer, and their relative significance on solute transport in fractured rocks. Their analytical model accounted for diffusion between the fracture and an adjacent matrix composed of different geological layers (limited layered matrix) through implementing a stepped diffusion process from the flowing water through the stagnant layer and subsequently the adjacent matrix. The model can be extended to describe contaminant transport in heterogeneous fractured media consisting of different fracture and matrix characteristics. They found that in narrow fractures, the stagnant water layer and adjacent rock matrix may lead to considerable retardation. Their work recommended accounting for both the stagnant layer and at least two matrix layers when assessing the performance and safety of deep geological repositories for spent nuclear fuel, as the stagnant water layer allows the solutes to access a larger fracture surface from which to diffuse into the rock. Furthermore, equilibrium between the fracture and matrix was found to be reached more rapidly when the matrix is composed of layers of altered rock and coating as opposed to being intact since the former is more porous (Moreno and Crawford, 2009). Cvetkovic (2010) conducted short- and long-term tracer studies at the Äspö Hard Rock Laboratory site (Sweden) to examine the impact of heterogeneity of the rim zone (altered rock), which experienced decreasing porosity. They concluded that the macroscopic effects of the rim zone microstructure must be considered in order to extrapolate retention properties to larger scales and longer times (Neuman, 2005).

Matrix retention is often described using retention time distributions, which are in turn derived from the above discussed analytical solutions for transport in a single fracture (e.g., Cvetkovic, 2010; Sudicky & Frind, 1982; Tang et al., 1981). These retention time distributions are typically precomputed and included in look-up tables. As these solutions consider additional mechanisms and phenomena under wider ranges of conditions, the lookup tables are more computationally intensive due to the large number of values in each table and thus require multivariate interpolation methods. It is for these reasons that numerical approaches are considered attractive alternatives to complex analytical solutions for simulating contaminant fate and transport phenomena (e.g. Hammond, Lichtner, and Rockhold 2011; Iraola et al. 2019; Stein et al. 2017). In this respect, random walk methods are particularly appealing as they are not vulnerable to numerical dispersion, they are able to accommodate complex model parameterizations, and they are numerically efficient (Khafagy et al., 2020; Noetinger et al., 2016; Painter et al., 2008). Some researchers have implemented mass retention in the matrix within random walk simulations using retention time distributions derived from analytical solutions for transport in a single fracture ( e.g., Cvetkovic, 2010; Sudicky and Frind, 1982; Tang et al., 1981). However, process-based models of fractured systems (i.e., mass balance, advection, dispersion, chemical reactions) are generally computationally intensive. Moreover, dual-porosity systems are highly nonlinear due to the difference in time scales between the fracture and matrix. As a result, numerical simulation of dual-porosity systems requires even more extensive time and resources.

Appropriately trained data-driven models have recently been proposed as an alternative approach to simulating complex physical and geochemical processes in fractured media (Esfahani and Datta,

2016). When validated, such models may substantially decrease computational time and improve feasibility and reliability of solute transport simulations. Such models can generally specify the relationship between input patterns (e.g., mass flux at system boundaries, hydraulic, geological, and chemical properties) and output patterns (i.e., solute spatiotemporal concentration variation within the system).

Genetic Programming (GP) techniques, inspired by biological evolution, were first proposed by Koza (1994). Compared to other machine learning methods, the key advantage of GP lies in its ability to optimize both the variables and constants of the candidate models, while being free of the constraints imposed by initial model structure definitions. To reach a solution, GP initially generates a random population, using various functions and terminals assigned by the user. At each subsequent generation, a new population is created by selecting the best generation, defined by the most accurate relationship between the independent and dependent variables (Heydari et al., 2016; Sheikh Khozani et al., 2020) (i.e., best gene). GP is a robust method with several advantages over other commonly employed data-driven methods (e.g., artificial neural networks) (Hadi and Tombul, 2018), including: 1) generation of explicit expressions or “glass box” models, 2) automatic discovery of model structure utilizing given data, 3) adaptive, evolutionary ability to generate global solutions without becoming trapped in local optima, and 4) not requiring any specific prior domain knowledge. As such, GP has been applied widely in water resource-related research, including hydrogeologic (Aryafar et al., 2019; Cianflone et al., 2017; Esfahani and Datta, 2016; Sadat-Noori et al., 2020), river stage (Ghorbani et al., 2018; Hadi and Tombul, 2018; Mehr and Gandomi, 2021), real-time wave forecasting (Kambekar and Deo, 2014), water quality (Jamei

et al., 2020), and rainfall-runoff modelling (Chadalawada et al., 2020; Heřmanovský et al., 2017). Multi-gene genetic programming (MGGP) advances GP through linearly combining low-depth GP blocks to improve the accuracy of solutions evolved by single-gene GP. Additionally, MGGP develops less complex models than single-gene GP as it uses fewer functions (Gandomi et al., 2015). Although MGGP is being adopted quickly, its use in water resource applications is not yet ubiquitous. A recent review of GP applications in hydrology found that the MGGP variant was used in nine of 142 papers (Danandeh Mehr et al., 2018).

The purpose of this study is to provide an accurate, closed-form data-driven solution (describing reactive solute transport in single, saturated fractures with matrix diffusion) that is substantially more computationally efficient than current methods (i.e., numerical and analytical approaches). MGGP is employed to obtain an accurate relationship between the coefficients of the lognormal distributions that describe an ensemble of breakthrough curves (BTC) as outputs (i.e., dependent variable), and the hydraulic, geological, and chemical parameters of the fracture-matrix system as inputs (i.e., independent variable). This more computationally efficient model will facilitate the simulation of complex, network-scale problems.

### **3.2. Model Development**

A dataset was generated containing an ensemble of BTCs using an analytical solution developed by Sudicky and Frind (1982), based on a set of input parameters that span a specified range for the hydraulic, geological, and chemical properties. Subsequently, MGGP is used to generate a solution that accurately describe the relationship between the inputs (i.e., hydraulic, geological, and

chemical properties) and the outputs (i.e., parameters of the lognormal distribution describing the BTC ensemble).

The analytical solution (Sudicky and Frind, 1982) simulates solute transport in one-dimensional fractures with a constant concentration at the inlet boundary. The solution considers advection, molecular diffusion and mechanical dispersion within the fracture, lateral matrix diffusion, adsorption within the matrix and on the fracture wall, and decay, and provides the BTCs at a specified distance from the injection source (see Appendix A for further details).

### **3.2.1 Dataset**

The dataset consists of the BTCs calculated using **Eq. (A.2.1)** with the parameter values listed in **Table 3-1**, which provide a possible 352,800 combinations of hydraulic, geological, and chemical properties. The ranges of these properties are selected to represent the values most commonly observed in recent literature (as referenced in **Table 3-1**). The integrals in **Eq. (A.2.1)** were solved numerically using a scanning procedure to determine the numerically significant ranges of  $\epsilon$  and  $\xi$ . Subsequently, the midpoint rule was employed to discretize the integration function into 50,000 and 1,000 connected rectangles for  $\epsilon$  and  $\xi$ , respectively, within the significant range. This approach is expected to result in more efficient integration with minimal loss in accuracy as each integral is only discretized within the significant range. However, even with this discretization procedure, it would take many years to conduct all of these simulations on a typical PC. As such, the Shared Hierarchical Academic Research Computing Network (SHARCNET) was used. The

input file for the script contains approximately 350 sub input files which are distributed amongst three computing clusters to generate the BTCs via parallel processing.

**Table 3-1: Range of values for fracture and solute properties.**

${}^3L$	${}^1V$	$D^* = 1 \times 10^{-n}$	${}^2b$	$2B$	${}^3\alpha$	${}^4\theta$
(m)	(m/day)	(m <sup>2</sup> /sec)	( $\mu$ m)	(m)	(m)	(-)
1, 5, 10,	1, 5, 10,					0.005,
50, 100,	50, 100,	n = 12, 10, 8,	1, 5, 10, 50,	0.5, 1, 2,	0.1, 0.5,	0.01,
500,	500,	6, 4, 3	100, 500,	5, 10, 20	1, 5, 10	0.05,
1000	1000,		1000, 5000			0.1, 0.5
	5000					

<sup>1</sup>Based on Worthington and Foley, (2021); Guimerà and Carrera, (2000); Wang et al., (2018)

<sup>2</sup>Based on Wang et al., (2020); Medici et al., (2019); Ren et al., (2018)

<sup>3</sup>Based on Zech et al., (2015)

<sup>4</sup>Based on Worthington and Foley, (2021); Zhou et al., (2007)

where  $L$  [L] is the fracture length,  $V$  [L/T] is groundwater velocity in the fracture,  $D^*$  [L<sup>2</sup>/T] is the molecular diffusion coefficient for the solute in water,  ${}^2b$  [L] is the aperture width,  $2B$  [L] is the distance between centerline of two fractures,  $\alpha$  [L] is the dispersivity, and  $\theta$  [-] is the matrix porosity.

A lognormal distribution was fit to each BTC using non-linear least squares regression, and the best fitting parameters were calculated by minimizing the root mean square error (RMSE) between the analytical solution BTC and the corresponding lognormal distribution as follows:

$$RMSE = \sqrt{\frac{\sum_{i=1}^n (C_{1,i} - C_{2,i})^2}{n}} \quad (3-1)$$

where  $C_{1,i}$  and  $C_{2,i}$  are the solute concentrations calculated at the fracture outlet at a specified time ( $i$ ), obtained from the analytical solution and the appropriate lognormal distribution, respectively, and  $n$  is the number of concentration points on the curve used in this analysis.

Matrix retardation is implemented in the PDF and CDF of the lognormal distribution by dividing the time,  $t$ , by the retardation coefficient ( $R_m$ ) (Khafagy et al. 2020; Zhang et al. 2012) as follows:

$$\text{PDF: } \frac{1}{\frac{t}{R_m} \sigma \sqrt{2\pi}} \exp\left(-\frac{\left[\ln\left(\frac{t}{R_m}\right) - \mu\right]^2}{2\sigma^2}\right) \quad (3-2)$$

$$\text{CDF: } \frac{1}{2} + \frac{1}{2} \operatorname{erf}\left(-\frac{\ln\left(\frac{t}{R_m}\right) - \mu}{\sqrt{2}\sigma}\right) \quad (3-3)$$

where  $\mu$  [ $\ln(T)$ ] is the mean,  $\sigma$  [ $\ln(T)$ ] is the standard deviation, and  $t$  [ $T$ ] is the solute arrival time at the outlet. The matrix tortuosity ( $\tau$ ) is accounted for in the matrix diffusion coefficient,  $D_m$ , which is obtained by multiplying the molecular diffusion coefficient,  $D^*$ , by  $\tau$ .

### 3.2.2 Multi-gene Genetic Programming

Evolutionary Algorithms (EAs) are capable of approximately simulating complex models effectively using stochastic search methods. GP models are a class of EAs considers elements composed from either a function (tree) or terminal (leaf) set. Function sets may include arithmetic operators (+, -,  $\times$ , or  $\div$ ), mathematical functions (sin, cos, tanh, ln, etc.), Boolean operators (AND, OR, NOT, etc.), logical expressions (IF or THEN) or any other suitable functions defined by the

user, whereas terminal sets include variables, constants, or both (**Fig. 3-1**). The GP tree is randomly formed from chosen functions and terminals. The root node is functional and has one or more branches extending from it that end in terminal nodes.

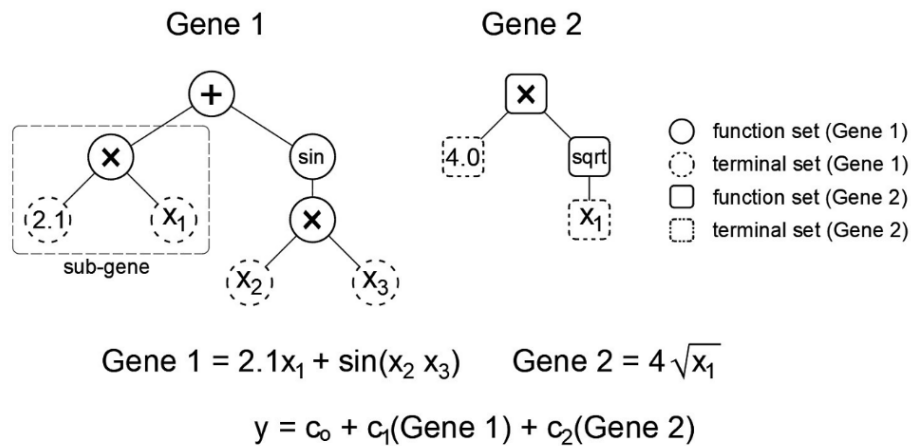


**Fig. 3-1: Example of a multigene symbolic model.**

Initially, a set of GP trees are randomly generated using functions and terminals determined by the user. The number of GP trees initially generated forms the initial population size (initial GP gene) and is based on the maximum allowable number of genes as defined by the user. MGGP models provide solutions through a linear combination of the individual genes (sub-genes). A sub-gene is a mathematical solution linking some or all of the input and output parameters, and each sub-gene forms a part of the solution for its generation (**Fig. 3-1**). The multi-gene model shown in **Fig. 3-1** predicts an output variable ( $y$ ) using input variables  $x_1$ ,  $x_2$ , and  $x_3$ . This model structure contains non-linear terms (i.e., sine and square root) but is linear in terms of the coefficients  $c_0$ ,  $c_1$ , and  $c_2$ .

The linear combination of these genes is referred to as a multi-gene; the linear coefficients (weights of genes) and the model bias are obtained from the training data using ordinary least squares regression.

The initial population of the MGGP model is generated from individuals that contain randomly evolved genes, and similar to the standard GP model, the MGGP population is subjected to evolution mechanisms (i.e., reproduction, crossover, mutation, and architecture-altering operations) to generate an enhanced generation. The evolved (improved) population replaces the existing population. These evolutionary mechanisms mimic biological evolution (natural selection) processes reflecting “survival of the fittest”. However, some special crossover mechanisms, in addition to the standard evolution mechanisms, are introduced to allow exchange of genes (mutation) between individuals. The mutation operation provides six methods for mutation between genes: (1) sub-tree mutation; (2) mutation of constants using an additive Gaussian perturbation; (3) substitution of a randomly selected input node with another randomly selected input node; (4) set a randomly selected constant to zero; (5) substitute a randomly selected constant with another randomly generated constant; and (6) set a randomly selected constant to one. The evolutionary mechanisms are grouped into categories referred to as events and set by the user in the form of probabilities, such that the sum of reproduction, crossover, and mutation probabilities is 1. The reader is referred to (Searson et al., 2010) for a more detailed explanation of MGGP and the evolutionary mechanisms.

The fitness function describes the accuracy between the individual (input) and the target output and is evaluated by an objective function that is pre-defined by the user (e.g.,  $r^2$ , RMSE). GP

continues to produce new generations until it reaches a specified termination criterion based on either the desired fitness function or a maximum number of generations as defined by the user. It is important to consider the trade-off between accuracy and complexity in MGGP model development, which are influenced by the maximum depth of the GP tree that reflects the number of nodes, and the maximum allowable number of genes as specified by the user, respectively. **Fig. 3-2** shows the flowchart of the MGGP method for obtaining the best-fit model.

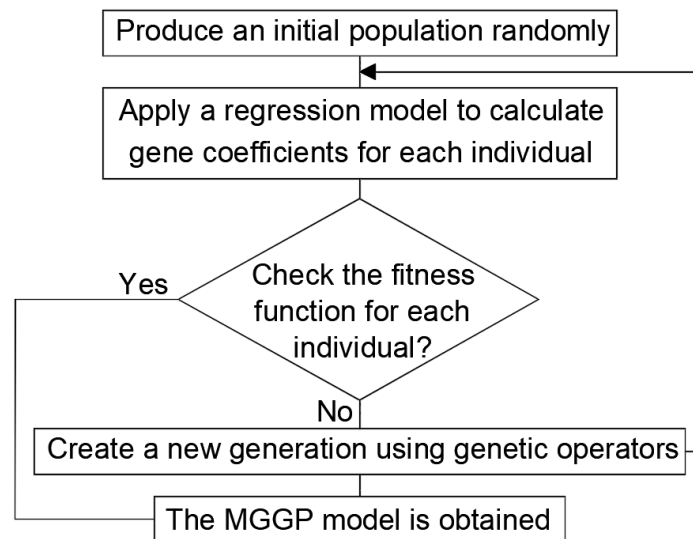


**Fig. 3-2: MGGP flowchart.**

Two MGGP models were developed in this work to establish a closed-form solution reflecting the relationships between the hydraulic, geological, and chemical parameters (i.e., input variables) and lognormal distribution parameters (i.e., mean ( $\mu_o$ ) and standard deviation ( $\sigma_o$ )) as output variables. In this study, the GPTIPS toolbox (Searson et al., 2010) for MATLAB (version 2021a) was used

to develop the MGGP models based on the parameters and settings in **Table 3-2**. The data were classified into training (80%), validation (10%) and testing (10%) sets to avoid overfitting. K-fold cross-validation was conducted using the training and validation datasets with 500 realizations to ensure model robustness. In each of the 500 realizations, the training and validation sets (i.e., 90% of the dataset) are divided into nine folds such that eight folds (i.e., 80% of the dataset) are used to train the MGGP model and one fold (i.e., 10% of the dataset) is used to validate the trained model. The fitness of each model was determined based on the minimized objective function, which was the RMSE between the predicted and actual values of the lognormal distribution parameters with a termination value of 0.0002. If the objective function did not reach the termination value, the optimal model was achieved when the MGGP procedure reached 1000 generations (**Table 3-2**). The “best” model from the 500 realizations was selected based on the lowest RMSE. This process was repeated until either the fitness termination value (0.0002) or the maximum number of generations (1000) was reached. The testing dataset was then used to select a single optimal MGGP model from the “best” models representing each generation to minimize individual effects of random data assignment to folds, and to ensure the model was not overfit. This optimal MGGP model is hereafter referred to as the single fracture solute transport (MGGP SF-ST) model. It must be noted that increasing the MGGP model accuracy, by specifying the population size and maximum number of generations, leads to increasing model complexity. As such, there is a trade-off between model accuracy and complexity, the latter of which is controlled by specifying the maximum number of genes and the tree depth. This trade-off was achieved herein by limiting both the maximum number of generations and population size to 1000 (for accuracy)

and the maximum tree depth and maximum number of genes to five and 10, respectively (to minimize model complexity).

**Table 3-2: Parameter and setting for best MGGP models.**

<b>Parameter</b>	<b>Setting</b>
<b>Population size</b>	1000
<b>Maximum number of generations</b>	1000
<b>Maximum number of genes</b>	10
<b>Maximum tree depth</b>	5
<b>Maximum sub-tree depth</b>	2
<b>Selection type</b>	Tournament
<b>Tournament size</b>	10
<b>Reproduction events</b>	0.05
<b>Crossover events</b>	0.85
<b>Mutation events</b>	0.1
<b>Ephemeral random constants</b>	-100 to 100
<b>Function set</b>	+, -, ×, /, power, ln, sqrt, exp

The closed-form solution generated using MGGP will develop  $\mu_p$  and  $\sigma_p$  that can be implemented in **Eq. (3-2)** and **Eq. (3-3)** to calculate the BTCs for pulse and constant solute injections, respectively. A sensitivity analysis was conducted using variance-based global sensitivity analysis to identify the level of influence of each input variable on the model by calculating their total sensitivity indices. The indices are calculated by generating a random value (uniformly distributed) for each variable within the specified range in the model and considering the contribution of the other variables on the simulation. Ten thousand samples are generated for each variable using a quasi-random Monte Carlo simulation to calculate the total sensitivity indices.

The MGGP SF-ST model was verified against both the analytical solution (**Eq. (A.2.1)**) and the random walk particle tracking (RWPT) model described by Khafagy et al., (2020) with an instantaneous release of 10,000 particles at the upstream end of the fracture. The hydraulic, geological, and chemical properties used in the validation process are  $L = 30$  m;  $V = 1$  m/day;  $D^* = 1 \times 10^{-9}$  m<sup>2</sup>/sec;  $2b = 80$   $\mu$ m;  $2B = 1$  m;  $\alpha = 1$  m;  $\theta = 0.1$ ;  $\tau = 1$ ;  $R = 1$ ; and  $R_m = 1, 2, 3$ , where  $R$  [-] is the retardation coefficient in the fracture.

### 3.3. Results and Discussion

The final dataset contained 101,740 BTCs of the potential 352,800 parameter combinations. While some of the BTCs generated required more refined discretization of the analytical solution (**Eq. (A.2.1)**) for the parameter combinations they represent, the computational time required for all 352,800 possible parameter combinations exceeded the computational time available through SHARCNET. Thus, the remaining 251,060 BTCs were not generated. Nevertheless, the 101,740

BTCs that form the dataset are based on the full range of all parameters listed in **Table 3-2**, and thus the volume and range of data generated are sufficient to implement MGGP. In parallel to the dataset generation, it was important to determine which combinations of parameters required further discretization. As such, the parameter combinations for the BTCs in the final dataset were visualized through a network graph (i.e., nodes and edges) using the network analysis software Gephi (version 0.9.2) (**Fig. 3-3**). The nodes are identified as the hydraulic, geological, and chemical property values and the edges are connections between the nodes that form a unique set of parameter combinations representing a BTC. The line (edge) thickness between each two nodes in **Fig. 3-3** is based on the weighted adjacency, and represents the number of BTCs generated based on combinations of the two nodes. For example, the properties  $2B$  and  $L = 1000\text{m}$  have a thinner edge than  $2B$  and  $L = 1\text{m}$  (**Fig. 3-3**) indicating fewer BTCs were generated using the former combination. The nodes are sized based on their degree centrality, which reflects the number of connections to other nodes. Properties with similar weighted adjacency and degree centrality for all values investigated were combined into a single node (i.e.,  $2B$ ,  $\alpha$ , and  $\theta$ ). Note that **Fig. 3-3** shows only the links that all properties share with  $2B$ ,  $\alpha$ , and  $\theta$  to maintain readability of the figure.

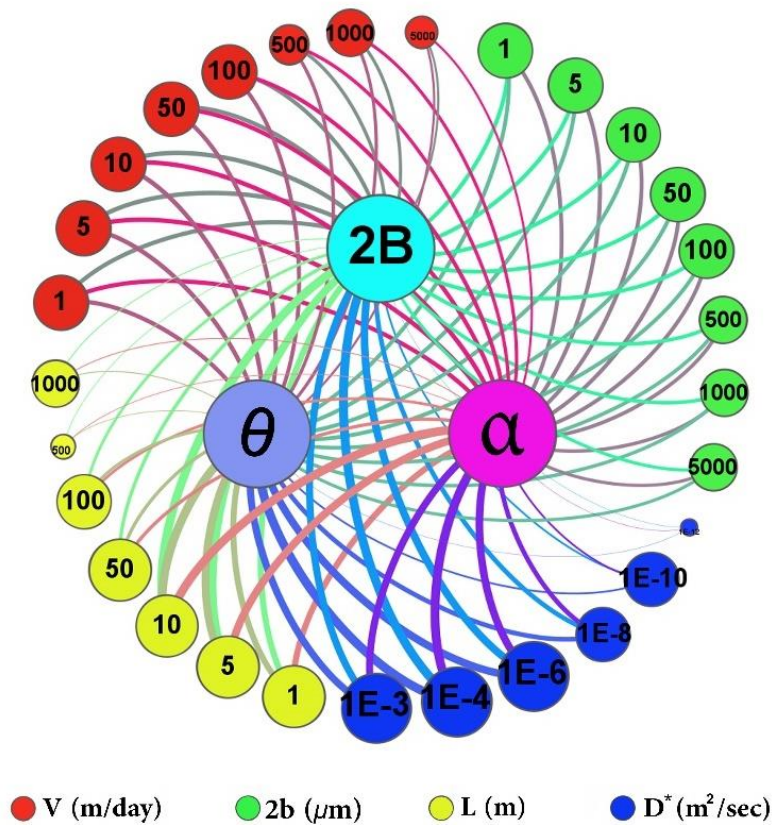


**Fig. 3-3: Network analysis based on weighted adjacency representing the final dataset.**

**Fig. 3-3** shows that the weighted adjacency (i.e., number of BTCs generated) decreases with increasing velocity, increasing fracture length, decreasing molecular diffusion coefficient, and increasing aperture size. This is because the  $\epsilon$  and  $\xi$  curves (Appendix A), which describe the integrals in **Eq. (A.2.1)**, tend to be more complex within these parameter ranges. This is demonstrated in **Fig. 3-4**, which shows the concentration vs.  $\log(\epsilon)$  curves for two select cases (Cases A and B) from the network analysis (**Fig. 3-3**), each discretized into 50,000 points. A log-

scale was chosen because the discretization is not the same among curves; it decreases with increasing  $\epsilon$ . The parameters in Case A were selected to reflect a combination with a low weighted adjacency, indicating that finer discretization is typically required to generate an accurate  $\epsilon$  curve for this parameter combination ( $L = 0.5$  m;  $V = 0.1$  m/day;  $D^* = 1 \times 10^{-6}$  m<sup>2</sup>/sec;  $2b = 0.001$   $\mu$ m;  $2B = 1$  m;  $\alpha = 10$  m;  $\theta = 0.1$ ;  $\tau = 1$ ;  $R = 1$ ;  $R_m = 1$ ). These parameter combinations also typically resulted in long-tailed breakthrough curves generally due to a very small diffusion coefficient ( $\sim < 1 \times 10^{-10}$  m<sup>2</sup>/sec) with a corresponding high velocity ( $\sim > 10$  m/day). The parameters in Case B were selected to reflect a high weighted adjacency, indicating that the discretization applied normally generated an accurate  $\epsilon$  curve for this parameter combination ( $L = 50$  m;  $V = 5$  m/day;  $D^* = 1 \times 10^{-9}$  m<sup>2</sup>/sec;  $2b = 10$   $\mu$ m;  $2B = 1$  m;  $\alpha = 1$  m;  $\theta = 0.1$ ;  $\tau = 1$ ;  $R = 1$ ;  $R_m = 1$ ). As a result, Case B was generated for the dataset, but Case A was not as there were not sufficient computing resources to implement the additional discretization required for all similar cases in the dataset.

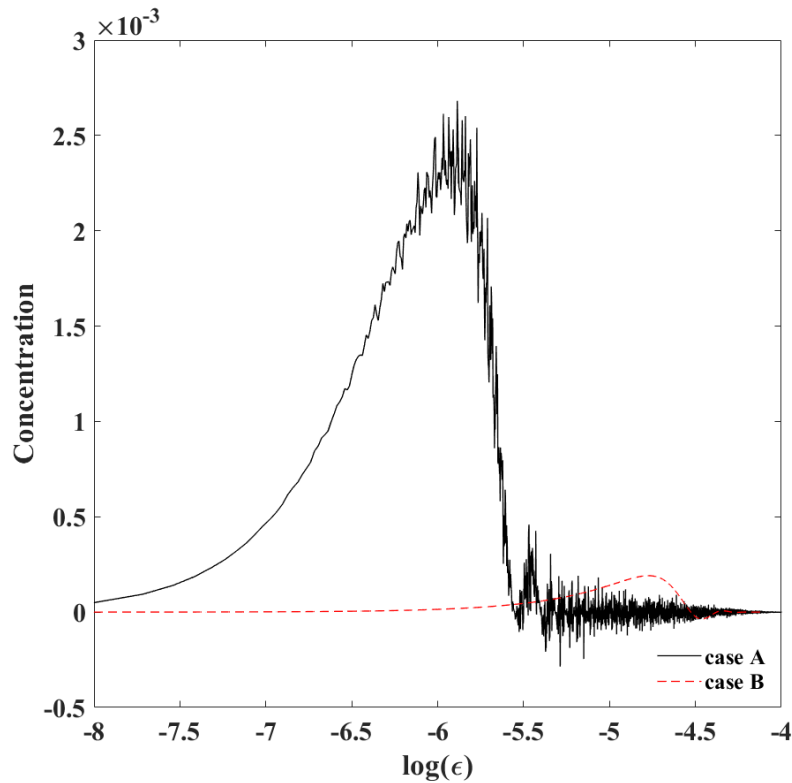


**Fig. 3-4: Solute concentration vs  $\log(\epsilon)$  at  $t = 5 \times 10^4$  years for case A and  $t = 450$  years for case B. Case A represents a parameter combination for which the midpoint rule requires additional discretization (i.e., more than 50,000 points) to generate an accurate curve defining the  $\epsilon$  integral. Case B represents a parameter combination for which the midpoint rule with the prescribed 50,000 discretization points can generate an accurate curve defining the  $\epsilon$  integral.**

The RMSE and  $r^2$  for the lognormal distribution describing each BTC generated for the dataset (i.e., 101,740 BTCs) exhibit excellent accuracy compared to the analytical solution. The median and highest RMSE are approximately 0.0051 and 0.023, respectively, and the median and lowest  $r^2$  values are approximately 0.9995 and 0.9932, respectively (**Fig. 3-5**).

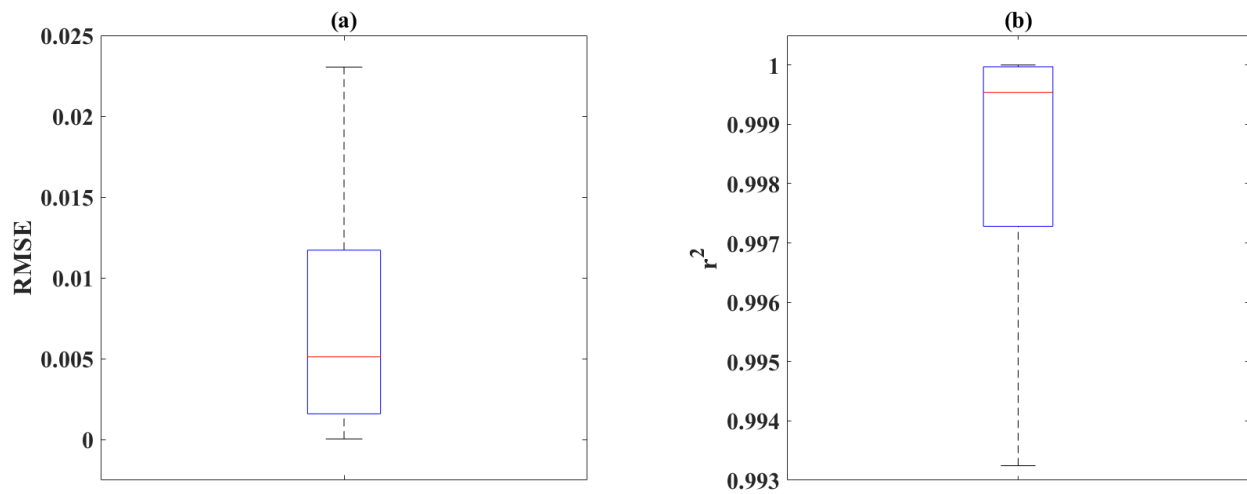


**Fig. 3-5: Boxplot of (a) RMSE and (b)  $r^2$  for the generated BTCs using lognormal distribution.**

### 3.3.1 MGGP Model Structure and Evaluation

MGGP was employed to develop a relationship considering various combinations of fracture properties (i.e.,  $L$ ,  $V$ ,  $D^*$ ,  $2b$ ,  $2B$ ,  $\alpha$ , and  $\theta$ ) and the parameters describing the lognormal distribution of the generated dataset (i.e.,  $\mu_o$  and  $\sigma_o$ ). The best set of variable combinations, represented by  $X_1$  to  $X_7$ , was selected considering the most accurate relationship between those

combinations and the parameters describing the lognormal distribution of the generated dataset (i.e.,  $\mu_o$  and  $\sigma_o$ ). This relationship, hereafter referred to as the MGGP SF-ST model, is described by the expressions for  $\mu_p$  and  $\sigma_p$  in in **Eqs.** (3-4) and (3-5):

$$\begin{aligned}
 \mu_p = & 0.0431 X_4 - 0.999 X_2 - 0.224 X_1 - 0.542 e^{(X_7 - X_1 - X_3)} - 0.267 e^{-e^{-X_1}} \\
 & + 0.0431 e^{-X_3^2} + 0.267 e^{X_7} - 0.903 \sqrt{X_3 + X_4 + e^{-e^{-X_4}}} \\
 & - 8.81 \times 10^{-6} (X_5 + X_1)^2 - 0.812 \sqrt{X_3 + e^{-e^{-X_4}}} \\
 & - 0.143 e^{(-X_1 - X_3)} (2 X_1 + 2 X_3 + X_3^2) \\
 & + 0.174 \sqrt{(X_7 - X_1)^2 + X_1^2 + X_3^2} + 0.0862 \sqrt{X_1} \\
 & - 0.402 \sqrt{3 X_1 + e^{-X_1} + e^{-X_4}} + 1.94
 \end{aligned} \tag{3-4}$$

$$\begin{aligned}
 \sigma_p = & 1.16 e^{(-X_3^{0.5 \sqrt{X_4}})} - 1.01 e^{(-X_1 - \sqrt{X_3})} + 0.947 e^{-e^{-X_4}} - 0.0573 X_3 \ln(\sqrt{X_3}) \\
 & - 0.00105 X_1 e^{(-X_3)} + 0.00209 X_4 e^{(-X_3)} + 1.31 \sqrt{X_3} e^{-e^{-X_1}} \\
 & + 3.07 \sqrt{e^{(-X_1)}} - 3.91 e^{(-X_1)^{\frac{1}{4}}} \\
 & + 3.84 \times 10^{-6} (X_4 - X_1 + \sqrt{X_6})(X_4 - X_1 + X_3^2) \\
 & + 3.35 \times 10^{-6} X_1 X_3 (X_1 - X_3)(X_3 - e^{(-X_3)}) + 1.05
 \end{aligned} \tag{3-5}$$

where:

$$\begin{aligned}
 X_1 &= \frac{V 2b 2B}{L D^* \theta} & X_2 &= \ln \left( \frac{V 2b}{L 2B \theta} \right) & X_3 &= \frac{\alpha}{L} & X_4 &= \frac{D^*}{V L} \\
 X_5 &= \ln (L) & X_6 &= D^* & X_7 &= 2b
 \end{aligned}$$

where  $V$  is in meters/year,  $L$  is in meters,  $D^*$  is in meters<sup>2</sup>/year,  $2B$  is in meters,  $2b$  is in meters,  $\alpha$  is in meters. The effluent BTC represents normalized concentration versus years and is obtained by substituting **Eqs.** (3-4) and (3-5) into either **Eq.** (3-2) or **Eq.** (3-3) for pulse or constant injections, respectively. Note that the MGGP technique is empirical, and thus the resulting MGGP SF-ST model is not dimensionally consistent – attention must thus be paid to utilize the correct input and output units (e.g., Hadi and Tombul, 2018; Jamei et al., 2020; Yan et al., 2021). It is also worth noting the physical meanings of some variable combinations. Specifically,  $X_1$  represents a modified Péclet number ( $P_e$ ) for the matrix,  $X_3$  represents the unique correlation between dispersivity and fracture length that has been observed in lab experiments (e.g., Zech et al., 2015), and  $X_4$  is the reciprocal of  $P_e$  in the fracture.

**Fig. 3-6** and **Fig. 3-7** show the MGGP tree structures of each gene in the generated expressions for the mean and standard deviation, respectively. Each expression was developed from seven input variables (i.e.,  $X_1, X_2, X_3, X_4, X_5, X_6, X_7$ ), and has ten genes and a bias as shown in **Eq.** (3-4) (mean) and **Eq.** (3-5) (standard deviation).

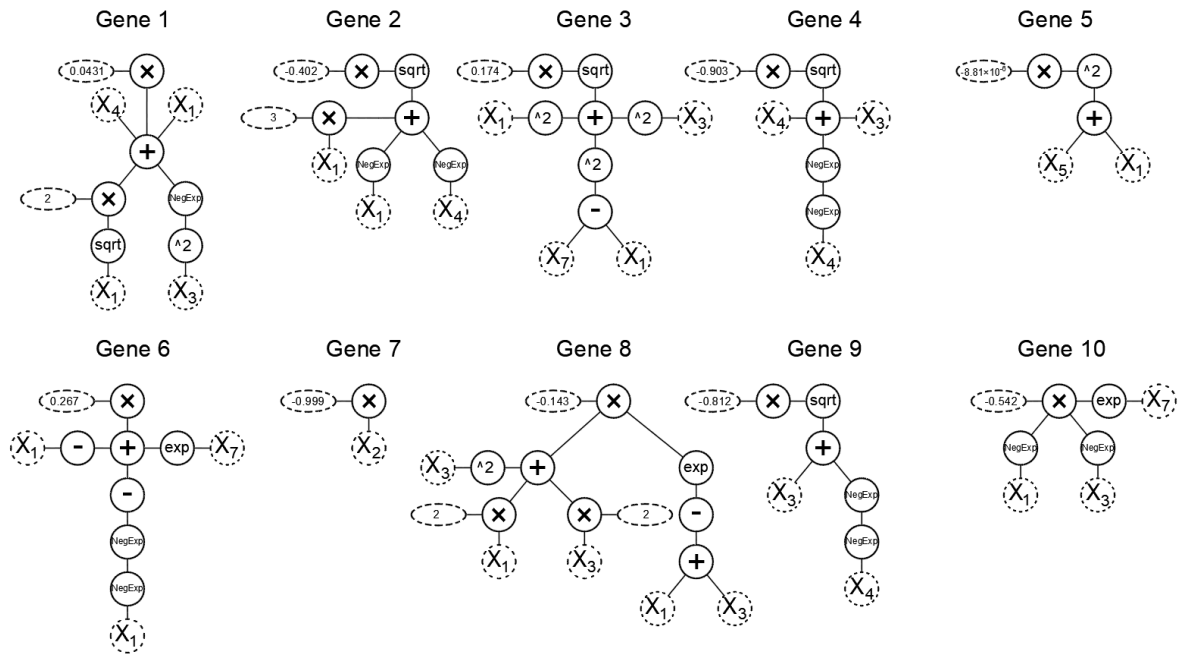


**Fig. 3-6: MGGP tree structure representing the expression for  $\mu_p$ .**

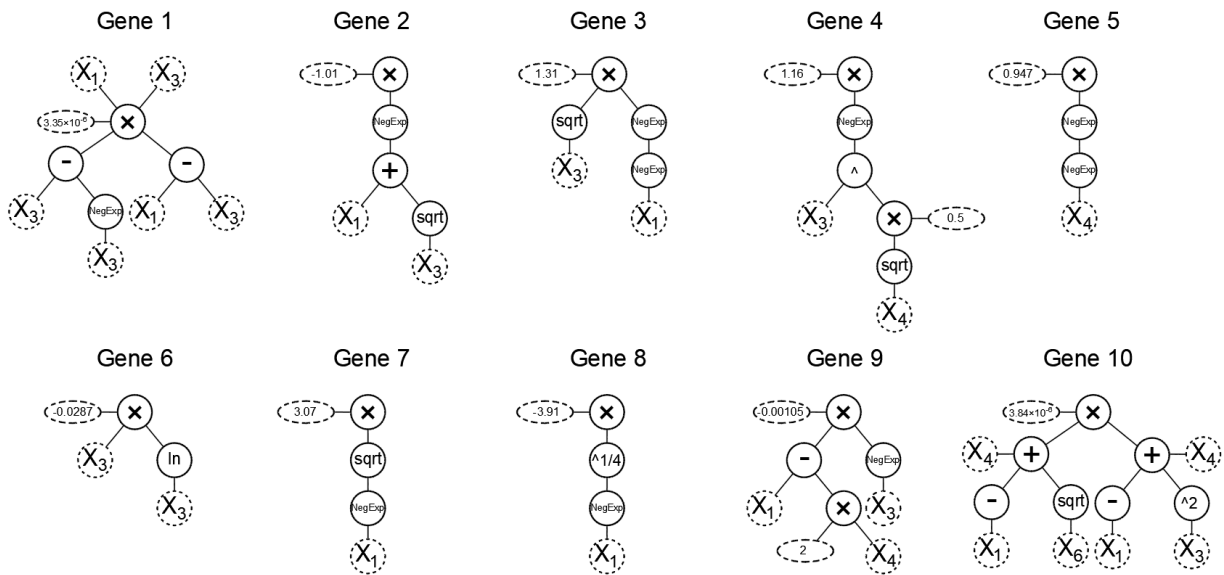


**Fig. 3-7: MGGP tree structure representing the expression for  $\sigma_p$ .**

**Table 3-3** shows the Pearson correlation coefficients ( $r$ ) between the input variables ( $X_1$  to  $X_7$ ) and the coefficients of the lognormal distributions from the dataset (i.e.,  $\mu_o$  and  $\sigma_o$ ).

**Table 3-3: Pearson correlation coefficients ( $r$ ) between input and output parameters.**

<b>Lognormal distributions coefficients</b>	$X_1$	$X_2$	$X_3$	$X_4$	$X_5$	$X_6$	$X_7$
<b>Mean</b>	-0.18	-0.56	-0.21	-0.09	0.39	-0.19	-0.26
<b>Standard deviation</b>	0.47	0.11	0.49	0.08	-0.51	-0.25	-0.04

The best fitness RMSE values are plotted against MGGP generation for the expressions representing  $\mu_p$  and  $\sigma_p$  (**Fig. 3-8**). This analysis shows that the model accuracy is not significantly improved beyond 290 and 220 generations for expressions representing  $\mu_p$  and  $\sigma_p$ , respectively. The selected models representing  $\mu_p$  and  $\sigma_p$  have RMSEs of 0.0493 and 0.0425, respectively, which correspond to generations 870 and 842, respectively. While the selected model accuracies are slightly lower than those achieved by models with a larger number of generations, they were chosen to balance accuracy with complexity.

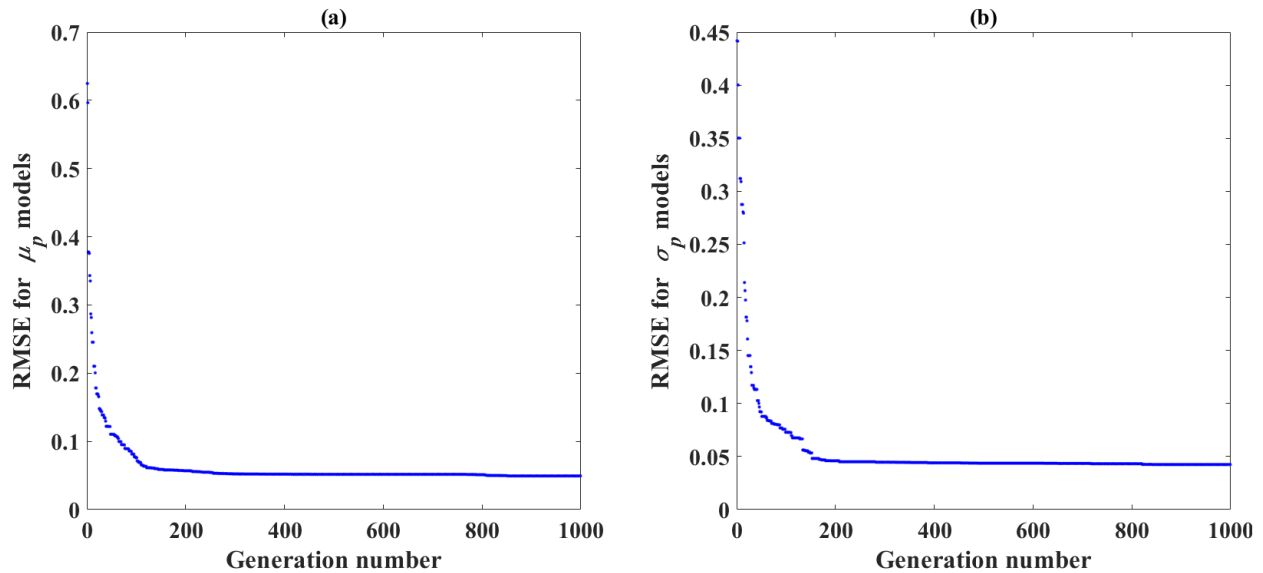


**Fig. 3-8: Best fitness (RMSE) versus generation number for (a)  $\mu_p$  and (b)  $\sigma_p$  components of the MGGP models.**

**Fig. 3-9** compares the BTCs predicted by the MGGP SF-ST model (Eqs. (3-4) and (3-5)) to the observed “best fitting” lognormal BTCs for all 101,740 datapoints in the dataset. The observed and predicted  $\mu$  and  $\sigma$  for the entire dataset achieved  $r^2 = 0.9998$  and  $r^2 = 0.9974$ , respectively. Note that of the 101,740 data points, only ~18,847 (18%) have a  $\sigma$  greater than two.

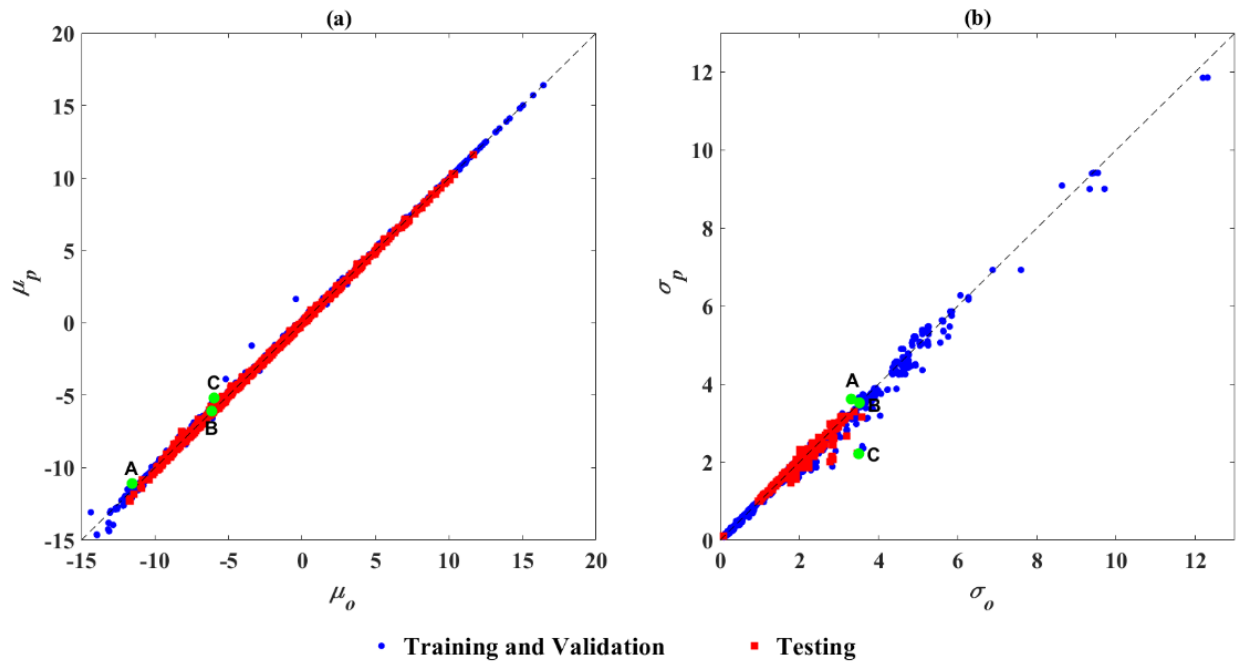


**Fig. 3-9: Observed versus predicted values of (a)  $\mu$  and (b)  $\sigma$  of the lognormal distribution.**

Blue dots represent training and validation data, and red dots represent testing data.

Points A, B, and C represent BTCs with overpredicted, well-predicted, and underpredicted  $\sigma$ , respectively.

**Fig. 3-9b** shows that of the BTCs with  $\sigma$  greater than two, the MGGP SF-ST model both over- and under-estimates  $\sigma$  values. Values of  $\sigma$  greater than two are associated with long-tailed BTCs, for which the analytical solution typically requires additional discretization to achieve sufficient accuracy. In this dataset, curves with a large dispersion (i.e.,  $>2$ ) represent a small fraction of the total number of curves ( $\sim 18\%$ ). **Fig. 3-10** shows the specific BTCs associated with points A, B, and C in **Fig. 3-9** to demonstrate the model sensitivity to the range of standard deviation residuals.

The comparison between the observed and predicted BTCs shows very good agreement, even for the cases in which  $\sigma$  is overestimated or underestimated (i.e., cases a and c, respectively).

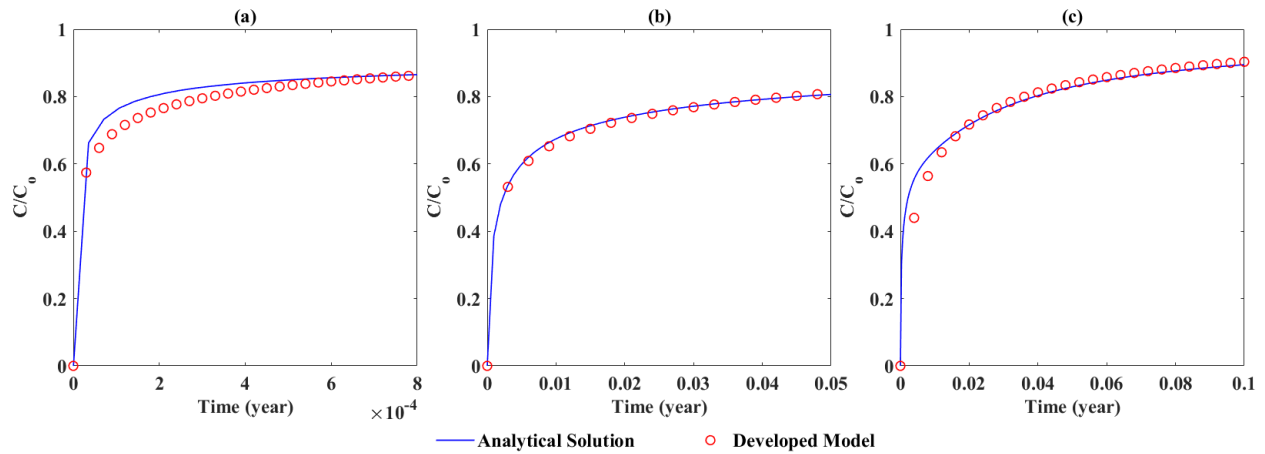


**Fig. 3-10: Observed and predicted BTCs for (a) overestimated, (b) well-estimated, and (c) underestimated  $\sigma$  of the lognormal distribution (points A, B, and C, respectively, from Fig. 3-9).**

The MGGP SF-ST model is assessed using non-parametric statistical tests at a 95% confidence level to compare the mean and variance of  $\mu_p$  and  $\sigma_p$  with that of  $\mu_o$  and  $\sigma_o$ . Specifically, the Wilcoxon rank-sum method (Bickel and Lehmann, 1975; Conover and Iman, 1980) evaluates the difference between the means of the observed and predicted parameters, whereas Levene's test (Levene, 1960) evaluates the difference between the variances of the observed and predicted parameters. The complete dataset (training, validation, and testing sets) is used for these statistical tests. With respect to the difference between the observed and predicted means, the p-values at the 95% confidence level are above 0.05 (**Table 3-4**) indicating that the model error is insignificant.

The calculated p-values for difference between the variances are also above 0.05 at the 95% confidence level (**Table 3-4**), indicating that the MGGP SF-ST model variability is not significantly different from the observed data. Thus, the MGGP SF-ST model is able to predict the observed data at a 95% confidence level.

**Table 3-4: p-values for Wilcoxon rank-sum and Levene’s tests (95% confidence level).**

Comparison of observed and predicted lognormal distribution coefficients	p-value (Wilcoxon rank-sum test)	p-value (Levene’s test)
<b>Mean (<math>\mu_o, \mu_p</math>)</b>	0.471	0.809
<b>Standard Deviation (<math>\sigma_o, \sigma_p</math>)</b>	0.128	0.2

A residual analysis was performed to ensure that the relationship between the genes and lognormal parameters is linear (i.e., the MGGP SF-ST model is linear) and the residuals are independent (**Fig. 3-11**). The box and whisker plots showing residuals from the training and validation datasets and testing dataset show that they are all mostly clustered around zero and are approximately normally distributed, indicating that the model is independent of the residuals and therefore valid. The box and whisker plots also show that  $\mu$  residuals from the testing dataset have a slightly higher standard deviation and median (e.g., standard deviation = 0.1044, median = 0.0303) than those from the training and validation datasets (e.g., standard deviation = 0.0542, median = - 0.005). However, these parameters are within an acceptable range for all datasets.

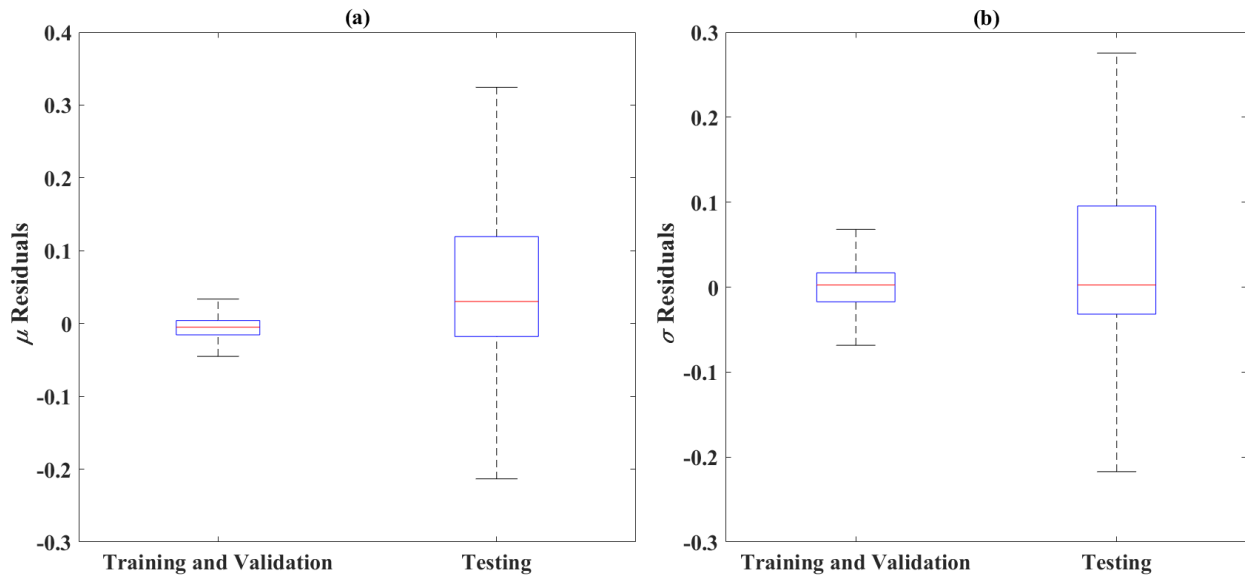


**Fig. 3-11: Box and whisker plots of residuals for the lognormal distribution parameters (a)  $\mu$  and (b)  $\sigma$ .**

**Fig. 3-12** illustrates the influence of each input variable on the MGGP SF-ST model using the variance-based global sensitivity analysis. The results show that  $X_1$ ,  $X_2$ , and  $X_4$  have the greatest impact on the  $\mu$  expression, while  $X_1$  and  $X_3$  have the greatest impact on the  $\sigma$  expression.

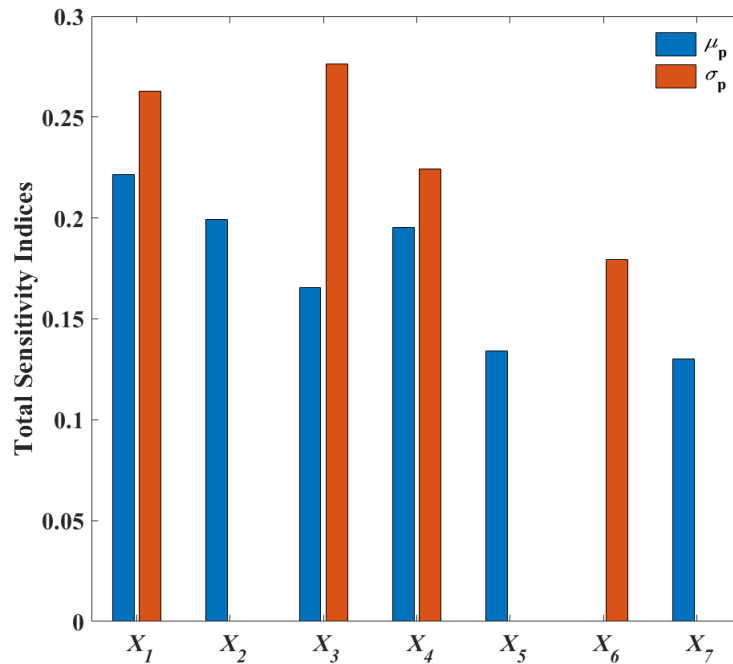


**Fig. 3-12: Sensitivity of the MGGP SF-ST ( $\mu_p$  and  $\sigma_p$ ) model to each of the input variables ( $X_1$  to  $X_7$ ).**

### 3.3.2 MGGP Model Verification

The comparisons between the MGGP SF-ST model, analytical solution, and RWPT simulations show excellent agreement, with the MGGP SF-ST model predicting slightly later arrival times ( $\sim 1.3\%$  later on average based on  $t_{50}$ ) than the analytical solution (**Fig. 3-13**). The MGGP SF-ST demonstrated excellent computational efficiency; it can predict the BTC for any combination of fracture properties (within the developed model parameter range) in less than one second through MATLAB (version 2021a). In comparison, the analytical solution and RWPT-based models

compute the same BTCs in the order of hours, in part due to the fact that the analytical solution typically requires more refined discretization to calculate the long-tailed BTCs. This efficiency becomes extremely important as the scale of a problem increases from that of a single fracture to a network, as it will be magnified.

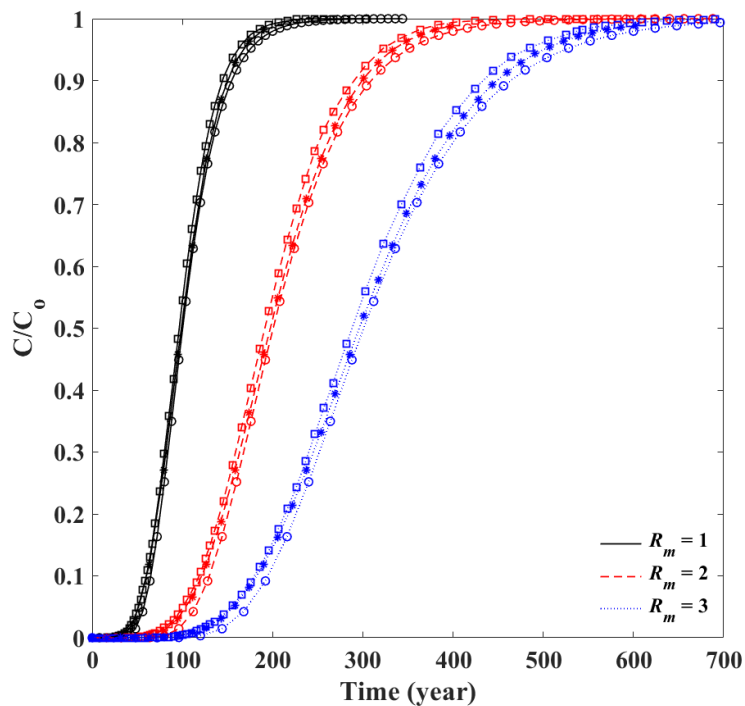


**Fig. 3-13: MGGP SF-ST model (circles) vs analytical solution (asterisks) vs RWPT model (squares) for transport in a single fracture.**

### 3.4. Conclusion

MGGP was employed to develop a closed-form solution (MGGP SF-ST model) to simulate reactive transport in a single, parallel plate fracture under a range of hydraulic, geological and chemical conditions for either a constant concentration or pulse injection at the inlet. The model was developed based on a large dataset of BTCs (101,740 datapoints) generated from a published analytical solution for solute transport in a single fracture under a range of conditions (i.e., velocity, dispersion along the fracture, molecular diffusion within the fracture and into the matrix, and adsorption within the matrix). A network graph was created to visualize the combinations of parameters for which BTCs were generated in the dataset. This analysis showed that the analytical solution for certain parameter combinations (typically those that result in long-tailed BTCs) require more refined discretization, which facilitated the generation of BTC for the full range of parameter combinations. The dataset was split into training, validation, and testing datasets and MGGP was employed to develop the model due to the nonlinear relationship between the model inputs ( $X_1$  to  $X_7$ ) and outputs (i.e.,  $\mu_o$  and  $\sigma_o$ ). A lognormal distribution was fit to each curve in the dataset (best-fitting curves) and the parameters (i.e.,  $\mu_o$  and  $\sigma_o$ ) were compared to those predicted by the MGGP SF-ST model (i.e.,  $\mu_p$  and  $\sigma_p$ ). The plot of the observed versus predicted  $\mu$  and  $\sigma$  for the entire dataset (**Fig. 3-9**) achieved  $r^2$  values of 0.9998 and 0.9974, respectively.

The MGGP SF-ST model was evaluated through nonparametric tests and an examination of the residuals. Wilcoxon rank-sum and Levene's tests were used to assesses the differences between the means and variances of the of the observed and predicted parameters, respectively, at the 95% confidence level and found the model errors to be insignificant. The residual analysis confirmed

that the relationship between the genes and lognormal parameters is linear and the residuals are independent. The MGGP SF-ST model was then validated against an analytical solution and a RWPT-based model, and the comparisons showed good agreement between all three models. The MGGP SF-ST model represents an important contribution as it is relatively easy to implement and provides a computationally efficient tool relative to existing analytical solutions and numerical models. This is particularly important as simulations increase in complexity and scale (i.e., from a single fracture to a network).

### **3.5. Acknowledgment**

The financial support for the study was provided through the CaNRisk-CREATE program of the Natural Science and Engineering Research Council (NSERC) of Canada (Grant Number: CREAT-482707-2016).

### 3.6. References

- Aryafar, A., Khosravi, V., Zarepourfard, H., Rooki, R., 2019. Evolving genetic programming and other AI-based models for estimating groundwater quality parameters of the Khezri plain, Eastern Iran. *Environ. Earth Sci.* 78, 1–13. <https://doi.org/10.1007/s12665-019-8092-8>
- Bickel, P.J., Lehmann, E.L., 1975. Descriptive Statistics for Nonparametric Models II. Location. *Ann. Stat.* 3, 1045–1069. <https://doi.org/10.1214/aos/1176343240>
- Carslaw, H.S., Jaeger, J.C., 1959. *Conduction of heat in solids*, Oxford science publications.
- Chadalawada, J., Herath, H.M.V.V., Babovic, V., 2020. Hydrologically Informed Machine Learning for Rainfall-Runoff Modeling: A Genetic Programming-Based Toolkit for Automatic Model Induction. *Water Resour. Res.* 56, 1–23. <https://doi.org/10.1029/2019WR026933>
- Cianflone, S.P.L., Dickson, S.E., Mumford, K.G., 2017. On the Importance of Gravity in DNAPL Invasion of Saturated Horizontal Fractures. *Groundwater* 55, 27–37. <https://doi.org/10.1111/gwat.12441>
- Conover, W.J., Iman, R.L., 1980. The Rank Transformation as a Method of Discrimination with Some Examples. *Commun. Stat. - Theory Methods* 9, 465–487. <https://doi.org/10.1080/03610928008827895>
- Cvetkovic, V., 2010. Significance of fracture rim zone heterogeneity for tracer transport in crystalline rock. *Water Resour. Res.* 46, 1–12. <https://doi.org/10.1029/2009WR007755>

- Danandeh Mehr, A., Nourani, V., Kahya, E., Hrnjica, B., Sattar, A.M.A., Yaseen, Z.M., 2018. Genetic programming in water resources engineering: A state-of-the-art review. *J. Hydrol.* 566, 643–667. <https://doi.org/10.1016/j.jhydrol.2018.09.043>
- Esfahani, H.K., Datta, B., 2016. Linked optimal reactive contaminant source characterization in contaminated mine sites: Case study. *J. Water Resour. Plan. Manag.* 142, 1–14. [https://doi.org/10.1061/\(ASCE\)WR.1943-5452.0000707](https://doi.org/10.1061/(ASCE)WR.1943-5452.0000707)
- Freeze, R.A., Cherry, J.A., 1980. Groundwater, *Journal of Hydrology.* [https://doi.org/10.1016/0022-1694\(80\)90057-8](https://doi.org/10.1016/0022-1694(80)90057-8)
- Gandomi, A.H., Alavi, A.H., Ryan, C., 2015. Handbook of genetic programming applications. *Handb. Genet. Program. Appl.* 1–593. <https://doi.org/10.1007/978-3-319-20883-1>
- Ghorbani, M.A., Khatibi, R., Danandeh Mehr, A., Asadi, H., 2018. Chaos-based multigene genetic programming: A new hybrid strategy for river flow forecasting. *J. Hydrol.* 562, 455–467. <https://doi.org/10.1016/j.jhydrol.2018.04.054>
- Guimerà, J., Carrera, J., 2000. A comparison of hydraulic and transport parameters measured in low- permeability fractured media. *J. Contam. Hydrol.* 41, 261–281. [https://doi.org/10.1016/S0169-7722\(99\)00080-7](https://doi.org/10.1016/S0169-7722(99)00080-7)
- Hadi, S.J., Tombul, M., 2018. Monthly streamflow forecasting using continuous wavelet and multi-gene genetic programming combination. *J. Hydrol.* 561, 674–687. <https://doi.org/10.1016/j.jhydrol.2018.04.036>
- Hammond, G.E., Lichtner, P.C., Rockhold, M.L., 2011. Stochastic simulation of uranium

migration at the Hanford 300 Area. *J. Contam. Hydrol.* 120–121, 115–128.

<https://doi.org/10.1016/j.jconhyd.2010.04.005>

Heřmanovský, M., Havlíček, V., Hanel, M., Pech, P., 2017. Regionalization of runoff models derived by genetic programming. *J. Hydrol.* 547, 544–556.

<https://doi.org/10.1016/j.jhydrol.2017.02.018>

Heydari, F., Saghafian, B., Delavar, M., 2016. Coupled Quantity-Quality Simulation-Optimization Model for Conjunctive Surface-Groundwater Use. *Water Resour. Manag.* 30, 4381–4397.

<https://doi.org/10.1007/s11269-016-1426-3>

Iraola, A., Trinchero, P., Karra, S., Molinero, J., 2019. Assessing dual continuum method for multicomponent reactive transport. *Comput. Geosci.* 130, 11–19.

<https://doi.org/10.1016/j.cageo.2019.05.007>

Jamei, M., Ahmadianfar, I., Chu, X., Yaseen, Z.M., 2020. Prediction of surface water total dissolved solids using hybridized wavelet-multigene genetic programming: New approach. *J. Hydrol.* 589, 125335.

<https://doi.org/10.1016/j.jhydrol.2020.125335>

Kambekar, A.R., Deo, M.C., 2014. Real Time Wave Forecasting Using Wind Time History and Genetic Programming. *Int. J. Ocean Clim. Syst.* 5, 249–259.

<https://doi.org/10.1260/1759-3131.5.4.249>

Khafagy, M.M., Abd-Elmegeed, M.A., Hassan, A.E., 2020. Simulation of reactive transport in fractured geologic media using random-walk particle tracking method. *Arab. J. Geosci.* 13.

<https://doi.org/10.1007/s12517-019-4952-5>

- Koza, J.R., 1994. Genetic programming as a means for programming computers by natural selection. *Stat. Comput.* 4, 87–112. <https://doi.org/10.1007/BF00175355>
- Mahmoudzadeh, B., Liu, L., Moreno, L., Neretnieks, I., 2013. Solute transport in fractured rocks with stagnant water zone and rock matrix composed of different geological layers - Model development and simulations. *Water Resour. Res.* 49, 1709–1727. <https://doi.org/10.1002/wrcr.20132>
- Medici, G., West, L.J., Banwart, S.A., 2019. Groundwater flow velocities in a fractured carbonate aquifer-type: Implications for contaminant transport. *J. Contam. Hydrol.* 222, 1–16. <https://doi.org/10.1016/j.jconhyd.2019.02.001>
- Mehr, A.D., Gandomi, A.H., 2021. MSGP-LASSO: An improved multi-stage genetic programming model for streamflow prediction. *Inf. Sci. (Ny)*. 561, 181–195. <https://doi.org/10.1016/j.ins.2021.02.011>
- Moreno, L., Crawford, J., 2009. Can we use tracer tests to obtain data for performance assessment of repositories for nuclear waste? *Hydrogeol. J.* 17, 1067–1080. <https://doi.org/10.1007/s10040-008-0418-7>
- Muskus, N., Falta, R.W., 2018. Semi-analytical method for matrix diffusion in heterogeneous and fractured systems with parent-daughter reactions. *J. Contam. Hydrol.* 218, 94–109. <https://doi.org/10.1016/j.jconhyd.2018.10.002>
- Neretnieks, I., 2006. Channeling with diffusion into stagnant water and into a matrix in series. *Water Resour. Res.* 42, 1–15. <https://doi.org/10.1029/2005WR004448>

- Neretnieks, I., 1980. Diffusion in the rock matrix: An important factor in radionuclide retardation? *J. Geophys. Res. Solid Earth* 85, 4379–4397. <https://doi.org/10.1029/JB085iB08p04379>
- Neuman, S.P., 2005. Trends, prospects and challenges in quantifying flow and transport through fractured rocks. *Hydrogeol. J.* 13, 124–147. <https://doi.org/10.1007/s10040-004-0397-2>
- Noetinger, B., Roubinet, D., Russian, A., Le Borgne, T., Delay, F., Dentz, M., de Dreuzy, J.R., Gouze, P., 2016. Random Walk Methods for Modeling Hydrodynamic Transport in Porous and Fractured Media from Pore to Reservoir Scale. *Transp. Porous Media* 115, 345–385. <https://doi.org/10.1007/s11242-016-0693-z>
- Levene, H. (1960). In *Contributions to Probability and Statistics: Essays in Honor of Harold Hotelling*, I. Olkin et al. eds., Stanford University Press, pp. 278-292.
- Painter, S., Cvetkovic, V., Mancillas, J., Pensado, O., 2008. Time domain particle tracking methods for simulating transport with retention and first-order transformation. *Water Resour. Res.* 44, 1–11. <https://doi.org/10.1029/2007WR005944>
- Ren, S., Gragg, S., Zhang, Y., Carr, B.J., Yao, G., 2018. Borehole characterization of hydraulic properties and groundwater flow in a crystalline fractured aquifer of a headwater mountain watershed, Laramie Range, Wyoming. *J. Hydrol.* 561, 780–795. <https://doi.org/10.1016/j.jhydrol.2018.04.048>
- Sadat-Noori, M., Glamore, W., Khojasteh, D., 2020. Groundwater level prediction using genetic programming: the importance of precipitation data and weather station location on model accuracy. *Environ. Earth Sci.* 79, 1–10. <https://doi.org/10.1007/s12665-019-8776-0>

Searson, D.P., Leahy, D.E., Willis, M.J., 2010. GPTIPS: An open source genetic programming toolbox for multigene symbolic regression. Proc. Int. MultiConference Eng. Comput. Sci. 2010, IMECS 2010 77–80.

Sheikh Khozani, Z., Safari, M.J.S., Danandeh Mehr, A., Wan Mohtar, W.H.M., 2020. An ensemble genetic programming approach to develop incipient sediment motion models in rectangular channels. J. Hydrol. 584, 124753. <https://doi.org/10.1016/j.jhydrol.2020.124753>

Stein, E.R., Frederick, J.M., Hammond, G.E., Kuhlman, K.L., Mariner, P.E., Sevougian, S.D., 2017. MODELING COUPLED REACTIVE FLOW PROCESSES IN FRACTURED CRYSTALLINE ROCK Emily R. Stein, Jennifer M. Frederick, Glenn E. Hammond, Kristopher L. Kuhlman, Paul E. Mariner, S. David Sevougian.

Sudicky, E.A., Frind, E.O., 1982. Contaminant transport in fractured porous media: Analytical solutions for a system of parallel fractures. Water Resour. Res. 18, 1634–1642. <https://doi.org/10.1029/WR018i006p01634>

Tang, D.H., Frind, E.O., Sudicky, E.A., 1981. Contaminant Transport in Fractured Porous Media: Analytical Solution for a Single Fracture. Comput. Geosci. 38, 80–86. <https://doi.org/10.1016/j.cageo.2011.05.008>

Trincherro, P., Iraola, A., 2020. Models for the assessment of transport of naturally-occurring nuclides in fractured media. J. Hydrol. 580, 124322. <https://doi.org/10.1016/j.jhydrol.2019.124322>

Trincherro, P., Painter, S.L., Poteri, A., Sanglas, J., Cvetkovic, V., Selroos, J.O., 2020. A Particle-

Based Conditional Sampling Scheme for the Simulation of Transport in Fractured Rock With Diffusion Into Stagnant Water and Rock Matrix. *Water Resour. Res.* 56, 1–18. <https://doi.org/10.1029/2019WR026958>

Wang, M., Zhao, W. dong, Garrard, R., Zhang, Y., Liu, Y., Qian, J. zhong, 2018. Revisit of advection-dispersion equation model with velocity-dependent dispersion in capturing tracer dynamics in single empty fractures. *J. Hydrodyn.* 30, 1055–1063. <https://doi.org/10.1007/s42241-018-0134-2>

Wang, Z., Bi, L., Kwon, S., Qiao, L., Li, W., 2020. The effects of hydro-mechanical coupling in fractured rock mass on groundwater inflow into underground openings. *Tunn. Undergr. Sp. Technol.* 103, 103489. <https://doi.org/10.1016/j.tust.2020.103489>

Worthington, S.R.H., Foley, A.E., 2021. Deriving celerity from monitoring data in carbonate aquifers. *J. Hydrol.* 598, 126451. <https://doi.org/10.1016/j.jhydrol.2021.126451>

Yan, X., Mohammadian, A., Khelifa, A., 2021. Modeling spatial distribution of flow depth in fluvial systems using a hybrid two-dimensional hydraulic-multigene genetic programming approach. *J. Hydrol.* 600, 126517. <https://doi.org/10.1016/j.jhydrol.2021.126517>

Zech, A., Attinger, S., Cvetkovic, V., Dagan, G., Dietrich, P., Fiori, A., Rubin, Y., Teutsch, G., 2015. Is unique scaling of aquifer macrodispersivity supported by field data? *Water Resour. Res.* 51, 7662–7679. <https://doi.org/10.1002/2015WR017220>

Zhang, Y., LaBolle, E., Reeves, D.M., Russell, C., 2012. Development of RWHet to Simulate Contaminant Transport in Fractured Porous Media. Nevada University, Reno, NV (United

States). <https://doi.org/10.2172/1091944>

Zhou, Q., Liu, H.H., Molz, F.J., Zhang, Y., Bodvarsson, G.S., 2007. Field-scale effective matrix diffusion coefficient for fractured rock: Results from literature survey. *J. Contam. Hydrol.* 93, 161–187. <https://doi.org/10.1016/j.jconhyd.2007.02.002>

## **Chapter 4: A Rapid, Simplified, Hybrid Modeling Approach for Simulating Solute Transport in Discrete Fracture Networks**

This chapter discusses the development of a numerical model to simulate spatial and temporal solute transport in discrete fracture networks with implementing the mass exchange between the fracture and the surrounding matrix. The developed model considers three mechanisms: advection and dispersion along the fracture, molecular diffusion within the fracture and into the matrix, and adsorption within the matrix. The developed model predictions are compared to those of an existing analytical model and a computational fluid dynamics (CFD) model employing Navier Stokes equations. The model will facilitate solute transport simulations in complex fracture networks as a result of the pronounced computational efficiency in predicting solute transport.

Authors: M. Khafagy, S. E. Dickson-Anderson, W. El-Dakhakhni

Journal: Computers and Geotechnics

Status: Submitted, and received minor comments from the journal

### **Chapter 4 Contributions:**

Mohamed Khafagy: Conceptualization, Methodology, Software, Formal analysis, Writing, and Original draft preparation.

Sarah Dickson-Anderson: Writing & Review & Editing, Supervision, and Funding acquisition.

Wael El-Dakhakhni: Writing & Review & Editing, Supervision, and Funding acquisition.

## **Abstract**

In this paper, a hybrid model is developed to simulate the transport of solute in discrete fracture networks. The mass exchange between the fracture and the surrounding matrix is implemented. The developed model considers three mechanisms: advection and dispersion along the fracture, molecular diffusion within the fracture and into the matrix, and adsorption within the matrix. Furthermore, the developed model can predict solute transport at fracture intersections and at the discrete fracture network outlet for both constant and pulse injections at inlet boundaries. The developed model predictions are compared to those of an existing analytical model and the results indicated the former is approximately 250 times faster than the latter, and this efficiency increases with network complexity. In addition, the developed model is compared to a computational fluid dynamics (CFD) model, employing Navier Stokes equations, and the comparison indicates the former has a lower dispersion compared to the latter. Nonetheless, the developed model can approximately predict the solute transport as the CFD model when assuming a higher value of dispersivity. Finally, the results in a high fracture density DFN indicated that the large diffusion coefficient, small fracture aperture, and high fracture spacings reduce the solute migration at a fractured medium.

**Key words:** solute transport, discrete fracture network, matrix diffusion, dual porosity

## 4.1. Introduction

Fractured porous media formations are critically important for multiple sectors, including potable water supply (e.g., Makungo et al., 2021; Nakayama et al., 2021), agriculture (e.g., Ju et al., 2020; Mahmoud et al., 2021; Paradis et al., 2018), oil and gas recovery (e.g., Ahmed et al., 2015; Alexandrov et al., 2020; Jongkittinarukorn et al., 2021; Li et al., 2021), carbon sequestration (e.g., Zakharova et al., 2020; Sharma et al., 2021; Wu et al., 2021; Nguyen et al., 2021), geothermal energy supply (e.g., Akdas and Onur, 2022; Eidesgaard et al., 2019; Schill et al., 2017; Wei et al., 2021), and radioactive waste management (e.g., Chittenden et al., 2016; Metcalfe et al., 2021; Stein et al., 2017; Watson et al., 2016). As such, increasing efforts have been devoted to the study of fractured rock environments over the past few decades. A good understanding of the physical processes that influence groundwater flow and solute transport in these environments is key to understand the compound and intersecting impacts on groundwater quantity and quality that result from these competing needs.

Solute transport through fractured formations is influenced by spatial heterogeneities from the macro-scale to the micro-scale, the confounding effects of which are characterized by the effective dispersion coefficient ( $D$ ). More specifically,  $D$  represents the collective solute spreading due to i) velocity variations across the fracture length caused by surface roughness; ii) macro-dispersion resulting from spatial heterogeneities that cause flow channeling; and iii) the Poiseuille velocity profile across the fracture aperture due to friction at the fracture walls (Taylor dispersion) (Wang and Cardenas, 2014; Detwiler et al., 2000; Wang et al., 2020; Khafagy et al., 2022a):

$$D = \tau D^* + D_{macro} + D_{Taylor} \quad (4-1)$$

where  $\tau$  [-] is tortuosity,  $D^*$  [ $L^2/T$ ] is the molecular diffusion coefficient,  $D_{macro}$  [ $L^2/T$ ] is the macro-dispersion coefficient, and  $D_{Taylor}$  [ $L^2/T$ ] is the Taylor dispersion coefficient. As the Peclet number ( $P_e$  [-]) increases, the dominance of each term in **Eq. (4-1)** increases; molecular diffusion ( $\tau D^*$ ) dominates at low  $P_e$  ( $10^{-3}$  to  $10^{-1}$ ), macro-dispersion dominates at intermediate  $P_e$  ( $10^{-1}$  to  $10^3$ ), and Taylor dispersion dominates at high  $P_e$  ( $>10^3$ ) (Wang 2014).

The porous matrix is orders of magnitude less conductive than the fractures (Iraola et al., 2019), but represents a majority of the reservoir storage capacity (Berre et al., 2019; Hawez et al., 2021). Solutes enter the matrix by molecular diffusion, which results in higher solute residence times (retardation) and more retention due to the large surface area. Consequently, the breakthrough curves (BTCs) in these systems have much more pronounced tails compared to their unconsolidated formations.

Discrete fracture network (DFN) modelling explicitly represents the geometry of relevant fractures (Hu et al., 2022), and is a conditionally accurate approach for simulating flow and transport in fractured rock systems (Viswanathan et al., 2018). In recent years, the DFN approach has been widely used to model flow and transport in fractured media due to the improved integration of accurate geological, fracture geometry, and aquifer parameters into these models (Dong et al., 2018; Feng et al., 2020; Maillot et al., 2016). While the geometric complexity of fractures in consolidated porous media make it practically impossible to obtain their true structure (Jing et al.,

2013), their geometric properties (e.g., location, length, orientation, aperture) can be represented by a statistical distribution (Liu et al., 2015; Miao et al., 2015; Sornette et al., 1990). The consideration of the detailed fracture geometry and connectivity in the network results in a more accurate representation and robust predictive simulation of flow and transport compared to the continuum approach, which parameterizes the continuum model parameters (e.g., permeability) (Hyman et al., 2019; Iraola et al., 2019). However, the DFN approach is typically implemented at significantly smaller scales than the continuum approach because it is computationally intensive due to the large number of flow and transport parameters required for the simulation (Larsson et al., 2013).

A substantial body of literature has been developed over the past decade investigating solute transport using DFN approach (e.g., Howroyd and Novakowski, 2022; Hu et al., 2022; Lei et al., 2017; Zhou et al., 2017; Zhu et al., 2016). For these approaches to be simple and feasible, they assume that i) diffusion in the matrix occurs only in the transverse direction (i.e., perpendicular to flow), and ii) transverse dispersion in the fracture is negligible due to relatively rapid mixing within the small aperture. However, fracture-matrix systems exist in which these assumptions are not valid. For example, transverse dispersion plays an important role in karst aquifers where apertures are large (Mohammadi et al., 2021). Rezaei and Zare, (2016) found that the influence of longitudinal (i.e., parallel to flow) diffusion in the matrix depends on the fracture-matrix spacing and the Peclet number. Chen et al., (2018) also investigated the influence of diffusion in parallel fracture-matrix systems and found that: i) incorrect estimates of longitudinal diffusion lead to overestimation the concentration near the fracture inlet and underestimation of the concentration

near the fracture outlet when the Peclet number is small ( $P_e \leq 10^{-3}$ ); ii) increasing the ratio of transverse diffusion in the matrix to that in the fracture increases the mass flux between the fracture and the matrix (Zhu et al., 2016); and iii) retardation and first-order decay in the matrix reduce the effect of longitudinal diffusion in the matrix to the point where it may be negligible. Somogyvári et al., (2017) modeled conservative tracer transport neglecting matrix diffusion using a finite difference model. They identified the main transport pathways in the network through evolving the network variants by geometry updates to fit the experimental tracer data during calibration. Despite these efforts towards the study of solute transport in fracture-matrix systems using the DFN approach, the application of DFNs is still at an early stage.

The goal of this study is to develop an accurate and efficient model to simulate solute transport through single fractures to improve the overall understanding of solute transport, and particularly to quantify the dispersion coefficient used in the advection–dispersion equation. To achieve this goal, a numerical model is developed to simulate solute transport in a two-dimensional DFN that considers one-dimensional (transverse) diffusion in the surrounding matrix.

## **4.2. Model Development**

Solving the classical advection-dispersion equation (ADE) directly within fractures while considering interactions with the surrounding matrix remains challenging. This is not only because the solution requires significant computational resources, but also because the ADE suffers from numerical dispersion in the high-Peclet-number ( $P_e$ ) regime (Wang et al., 2020). To minimize computational resources required without risking numerical dispersion, the developed numerical

network model is based on a closed-form solution that approximate the ADE solution (Khafagy et al., 2022b) in single fractures. Complete mixing is assumed at fracture intersections, and the transfer function approach is then applied numerically, using the midpoint rule for integration, to calculate the BTC on the downstream side of each fracture intersection. This BTC is then applied as the inlet boundary condition in the downstream fractures (Khafagy et al., 2022a).

The closed-form solutions represent the relationship between the hydraulic, geological, and chemical parameters of the fracture-matrix system as inputs and an ensemble of BTCs as outputs (See Section 3.2). This solution was obtained by employing the multi-gene genetic programming (MGGP) approach (Khafagy et al., 2022b), and consider advection, longitudinal mechanical dispersion and molecular diffusion within the fracture, transverse molecular diffusion into and within the matrix, and adsorption within the matrix for a single, parallel plate fracture-matrix system. The solution is available for either a constant concentration (Type 1) or pulse injection (Type 2) at the inlet boundary. The BTCs which are described by the probability density function (PDF) and the cumulative distribution function (CDF) of the lognormal distribution, respectively, are (Khafagy et al., 2022b):

$$\text{PDF: } \frac{1}{R_m \sigma \sqrt{2\pi}} \exp\left(-\frac{\left[\ln\left(\frac{t}{R_m}\right) - \mu\right]^2}{2\sigma^2}\right) \quad (4-2)$$

$$\text{CDF: } \frac{1}{2} + \frac{1}{2} \operatorname{erf}\left(-\frac{\ln\left(\frac{t}{R_m}\right) - \mu}{\sqrt{2}\sigma}\right) \quad (4-3)$$

where  $\mu$  is the mean,  $\sigma$  is the standard deviation,  $t$  [T] is the solute arrival time at the outlet in years, and  $R_m$  [-] is the retardation in the matrix. The expressions for the mean and standard deviation, respectively, are:

$$\begin{aligned} \mu = & 0.0431 X_4 - 0.999 X_2 - 0.224 X_1 - 0.542 e^{(X_7 - X_1 - X_3)} - 0.267 e^{-e^{-X_1}} \\ & + 0.0431 e^{-X_3^2} + 0.267 e^{X_7} - 0.903 \sqrt{X_3 + X_4 + e^{-e^{-X_4}}} \\ & - 8.81 \times 10^{-6} (X_5 + X_1)^2 - 0.812 \sqrt{X_3 + e^{-e^{-X_4}}} \\ & - 0.143 e^{(-X_1 - X_3)} (2 X_1 + 2 X_3 + X_3^2) \\ & + 0.174 \sqrt{(X_7 - X_1)^2 + X_1^2 + X_3^2} + 0.0862 \sqrt{X_1} \\ & - 0.402 \sqrt{3 X_1 + e^{-X_1} + e^{-X_4}} + 1.94 \end{aligned} \quad (4-4)$$

$$\begin{aligned} \sigma = & 1.16 e^{(-X_3^{0.5} \sqrt{X_4})} - 1.01 e^{(-X_1 - \sqrt{X_3})} + 0.947 e^{-e^{-X_4}} - 0.0573 X_3 \ln(\sqrt{X_3}) \\ & - 0.00105 X_1 e^{(-X_3)} + 0.00209 X_4 e^{(-X_3)} + 1.31 \sqrt{X_3} e^{-e^{-X_1}} \\ & + 3.07 \sqrt{e^{(-X_1)}} - 3.91 e^{(-X_1)^{\frac{1}{4}}} \\ & + 3.84 \times 10^{-6} (X_4 - X_1 + \sqrt{X_6})(X_4 - X_1 + X_3^2) \\ & + 3.35 \times 10^{-6} X_1 X_3 (X_1 - X_3)(X_3 - e^{(-X_3)}) + 1.05 \end{aligned} \quad (4-5)$$

where:

$$\begin{aligned} X_1 &= \frac{V 2b 2B}{L D^* \theta} & X_2 &= \ln \left( \frac{V 2b}{L 2B \theta} \right) & X_3 &= \frac{\alpha}{L} & X_4 &= \frac{D^*}{V L} \\ X_5 &= \ln(L) & X_6 &= D^* & X_7 &= 2b \end{aligned}$$

and  $V$  [L/T] is the average velocity in the fracture,  $2b$  [L] is the aperture size,  $2B$  [L] is the spacing between the fractures,  $D^*$  [L<sup>2</sup>/T] is the molecular diffusion coefficient for the solute in water,  $\alpha$  [L] is the longitudinal dispersivity,  $\tau$  [-] is the matrix tortuosity, and  $\theta$  [-] is the matrix porosity. Further details are provided in Khafagy et al., (2022b).

The single fracture BTCs are connected across the network using the framework proposed by Khafagy et al., (2022a). At each intersection in the network, the effluent BTCs for the upstream fractures based on a Type 2 influent boundary condition (BC) are summed to obtain the BTC at the intersection. Subsequently, solute mixing and mass redistribution at fracture intersections are handled using the complete mixing (CM) method, which has been widely adopted for modeling solute transport in DFNs (e.g., Bodin et al., 2007; Cvetkovic and Frampton, 2012; Frampton et al., 2019; Zhao et al., 2013, 2011; Zou et al., 2017). Once the solute mass at an intersection has been partitioned between the downstream fractures, connectivity is established between the upstream and downstream fractures by setting the inlet boundary of each downstream fracture as the injected BTC based on the mass partitioned to that fracture. The final effluent BTC for the downstream fracture is then determined by numerically applying a transfer function approach between influent BTCs and the mass transfer probability of reaching the fracture outlet based on a Type 2 influent BC as follows:

$$C_{final}(t) = \int_0^{\infty} C_1(\tau) C_2(t - \tau) d\tau \quad (4-6)$$

where,  $C_1$  [M/L<sup>3</sup>] is the solute concentration at time  $\tau$  at the fracture inlet,  $C_2$  [-] is the mass transfer probability of reaching the fracture outlet shifted by  $t$ , and  $C_{final}$  [M/L<sup>3</sup>] is the solute concentration at the fracture outlet after applying the transfer function approach between the solute concentrations at the fracture inlet and outlet. The model is developed using MATLAB.

The developed model calculates the solute mass at fracture intersections over time. To preserve

the solute mass balance in the network, the mass retained in the matrix block associated with each fracture is considered over time, and was calculated as the difference in mass within the fracture between the outlet and inlet, and the coordinates of this mass are assumed to be distributed equally along the fracture length.

### **4.3. Model Verification and Validation**

The developed model was verified by comparing simulation results to those obtained from the analytical network (AN) model developed by Khafagy et al., (2022a) using the CM method of mass sharing at intersections. Solute transport in the AN model is based on two analytical solutions (i.e., Bear, 1972; Sudicky and Frind, 1982) that consider advection and longitudinal hydrodynamic dispersion within the fractures, transverse matrix diffusion, sorption in the matrix, and first-order decay for a single constituent. A synthetic two-dimensional fracture network (DFN1) is used to demonstrate the efficiency of the developed model. DFN1 sits within a square domain of 350 m x 350 m (**Fig. 4-1**) with two equally distributed orientation sets in the probability density – (40° - 50°) and (130° - 140°) and a fracture density of 0.078 m/m<sup>2</sup> (the sum of the fracture lengths divided by the fracture network area). DFN1 includes 355 hydraulically active fractures and 92 dead-end fractures. The flow is from west to east with a 1 m head difference across these boundaries, with the north and south boundaries representing no-flow boundaries.

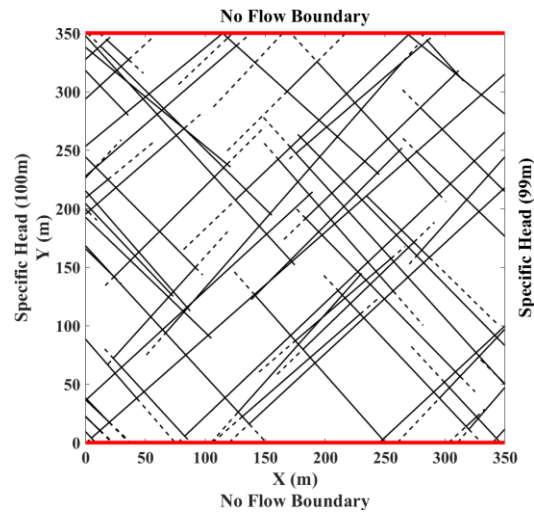


**Fig. 4-1: Synthetic fracture network (DFN1) for model verification. Solid lines represent hydraulically active fractures, while dashed lines represent dead-end fractures.**

The verification was conducted based on Cases 1 and 2 (**Table 4-1**) considering advection and hydrodynamic dispersion within the fractures, matrix diffusion, and sorption in the matrix. In these simulations, solute was injected along the west boundary using Type 1 and Type 2 influent boundary conditions, and the solute mass was divided between the inlet fractures based on their proportional volumetric flow rates.

**Table 4-1: Properties of the DFN for the Cases used in the verification and validation.**

Case	$\alpha$ (m)	$2b$ ( $\mu\text{m}$ )	$2B$ (m)	$D^*$ ( $\text{m}^2/\text{sec}$ )	$R_m$ (-)	$\theta$ (-)	$\tau$ (-)	$D_e$ ( $\text{m}^2/\text{sec}$ )	$\lambda$ ( $\text{day}^{-1}$ )	Mass Sharing Method
1	5	250	1	$1 \times 10^{-7}$	1 - 5	0.1	1	$1 \times 10^{-7}$	n/a	CM
2			1 - 5							
3			13.7							

Notes:

1.  $D_e = \tau D^*$  is the effective diffusion coefficient
2.  $\lambda$  is the first-order decay constant

The developed model was then compared to simulation results from a computational fluid dynamics (CFD) model to understand the impact of neglecting longitudinal diffusion in the matrix. The comparison was based on DFN1 (**Fig. 4-1**) using transport parameters for Case 3 (**Table 4-1**). COMSOL Multiphysics 5.5 (Zimmerman, 2006) was employed to sequentially solve the Navier-Stokes equations (to simulate fluid flow within the fractures), and the advection dispersion equation (to simulate solute transport across the entire domain, i.e., fractures and matrix). The Navier-Stokes equations describe single-phase, steady flow for an incompressible fluid under isothermal conditions:

$$\rho(u \cdot \nabla u) = -\nabla p + \mu \nabla^2 u \quad (4-7)$$

$$\nabla \cdot u = 0 \quad (4-8)$$

where  $u$  is the velocity vector,  $p$  is the total pressure,  $\rho$  is the fluid density ( $\rho = 1000 \text{ kg/m}^3$  for water), and  $\mu$  is the fluid viscosity ( $\mu = 1 \times 10^{-3} \text{ Pa}\cdot\text{s}$  for water). The hydraulic gradient applied was consistent with that used for the verification simulations (0.0029 m/m). The solute transport processes considered in the CFD model are governed by the advection dispersion equation written as:

$$\frac{\partial \theta c}{\partial t} + u \cdot \nabla c - \nabla \cdot \theta D^* (\nabla c) = 0 \quad (4-9)$$

where  $c$  [ $\text{M}/\text{L}^3$ ] is the solute concentration in the fluid phase,  $u$  [ $\text{L}/\text{T}$ ] is fluid velocity, and  $D^*$  [ $\text{L}^2/\text{T}$ ] is the molecular diffusion coefficient. In these simulations, dispersion results from

variations in the velocity field calculated by the Navier-Stokes equations. The network domain in the CFD model is discretized into 44,454 tetrahedral elements. The mesh size was selected to be coarse (~5 m) for the matrix domain, and finer (~0.5 m) near fracture intersections to capture the steep diffusion gradient (**Fig. 4-2**). The CFD model simulated DFN1 as a 3-D domain, with a unit width in the z-direction, and no-flow boundaries on either side in the z-direction (**Fig. 4-1**).

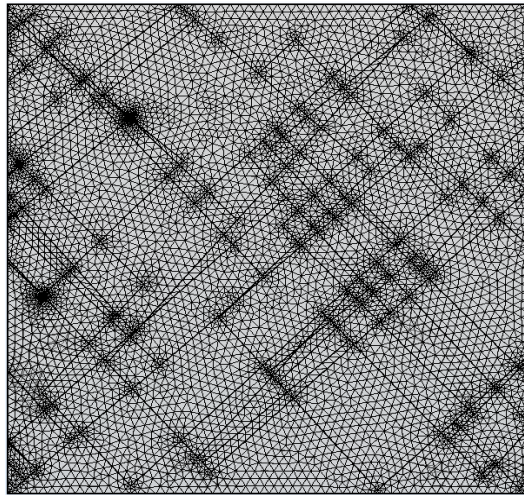


**Fig. 4-2: CFD model discretization scheme for DFN1 (Fig. 4-1).**

To visualize the spatial distribution of solute calculated by the developed model, each fracture in the network is discretized into 20 segments and the solute concentration at the fracture outlet is assigned to each segment. The network domain is then discretized into  $100 \times 100$  mesh grids and the solute mass within each grid block is summed and plotted.

As the diffusion process across the fracture-matrix interface is affected by the shape of the matrix

block,  $\overline{2B}$  is estimated by multiplying the fracture spacing by a shape factor  $(1 - \lambda)$ , where,  $\lambda$  is a dimensionless shape function that is approximately equal to 1/3 for the case of a matrix with a finite thickness (Zhang et al., 2013). Therefore,  $\overline{2B}$  is estimated to be 66% of the average fracture length ( $\overline{L_f} = 20.76$  m) which is approximated as the arithmetic mean of all fractures' lengths in the network and consequently  $\overline{2B} = 13.7$  m. The developed model assumes a constant fracture spacing for all fractures in the network ( $\overline{2B} = 13.7$ m) for comparison with the CFD model.

Following verification and validation in DFN1, the impact of fracture and matrix properties (i.e., diffusion, dispersivity, fracture aperture, and average fracture spacing) were investigated through simulations conducted in a second discrete fracture network, DFN2, with a much higher fracture density (**Fig. 4-3**). DFN2 was first presented by Khafagy et al., (2022a), and has the same domain size, fracture orientations, and boundary conditions as DFN1. DFN2 includes 13,083 fractures with two different orientations; 12,884 fractures are hydraulically active, 199 are dead-end fractures, and the fracture density is 0.449 m/m<sup>2</sup>.

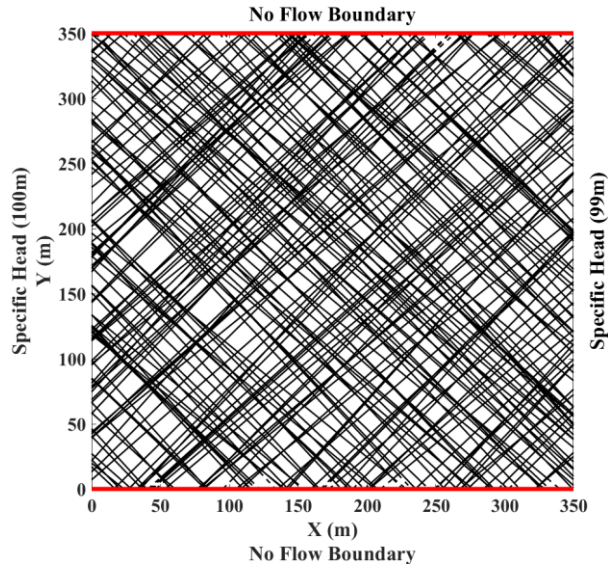


**Fig. 4-3: High fracture density DFN (DFN2) used for the simulation of spatial and temporal solute mass.**

#### **4.4. Results and Discussion**

The effluent BTCs calculated by the developed model for Case 1 parameters ( $\alpha = 5$  m;  $2b = 250$   $\mu\text{m}$ ;  $2B = 1$  m;  $D^* = 1 \times 10^{-7}$   $\text{m}^2/\text{sec}$ ;  $R_m = 1 - 3$ ;  $\theta = 0.1$ ;  $\tau = 1$ ) (**Table 4-1**) under both Type 1 and Type 2 influent boundary conditions in DFN1 using the CM method of mass sharing at intersections are plotted against those obtained from the AN model in **Fig. 4-4**. The comparison shows an excellent agreement between the developed model and the AN model for DFN1 for both influent boundary conditions. It is noteworthy that matrix retardation ( $R_m$ ) does not impact the accuracy of the AN model.

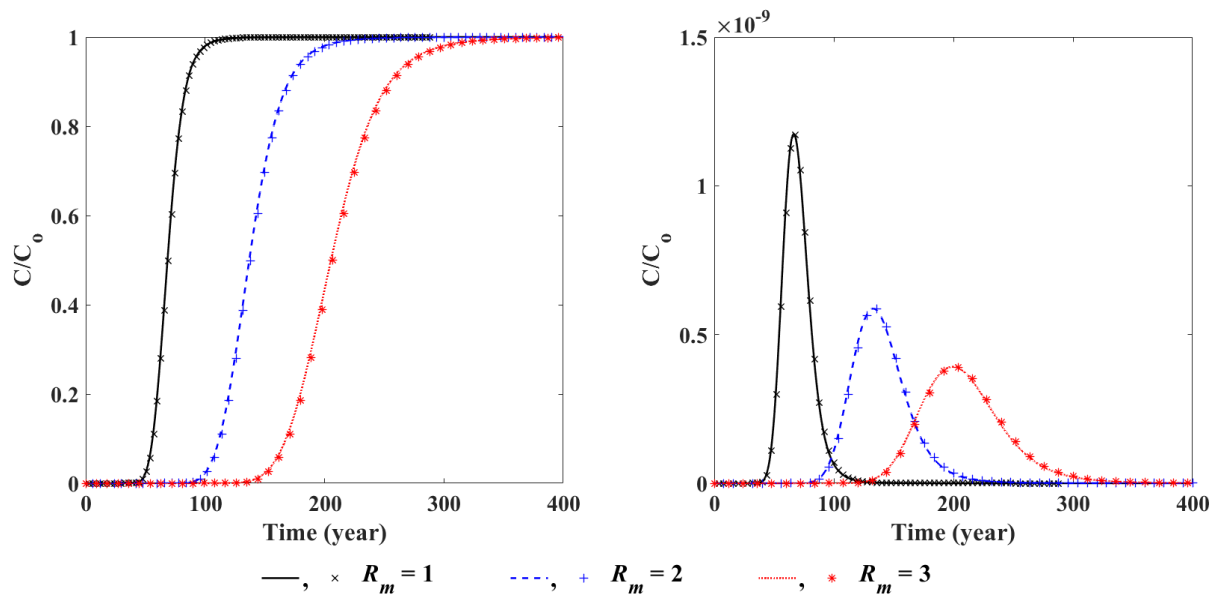


**Fig. 4-4: BTCs for Case 1 ( $\alpha = 5$  m;  $2b = 250$   $\mu$ m;  $2B = 1$  m;  $D^* = 1 \times 10^{-7}$  m<sup>2</sup>/sec;  $R_m = 1 - 3$ ;  $\theta = 0.1$ ;  $\tau = 1$ ) for (a) Type 1 and (b) Type 2 boundary conditions – lines represent AN model and symbols represent the developed model.**

The developed model was used to calculate effluent BTCs in DFN1 for Case 2 parameters ( $\alpha = 5$  m;  $2b = 250$   $\mu$ m;  $2B = 1 - 3$  m;  $D^* = 1 \times 10^{-7}$  m<sup>2</sup>/sec;  $R_m = 1$ ;  $\theta = 0.1$ ;  $\tau = 1$ ) (Table 4-1), which excludes matrix retardation (i.e.,  $R_m = 1$ ), under Type 1 and Type 2 influent boundary conditions. These were compared to results obtained from the AN model under the same conditions (Fig. 4-5). The comparison shows good agreement between the developed model and the AN model for DFN1, with the exception that the developed model has a slightly higher solute retention (by ~3.4%), with a slightly lower concentration peak for the Type 2 BC (by ~6%) compared to the AN model.

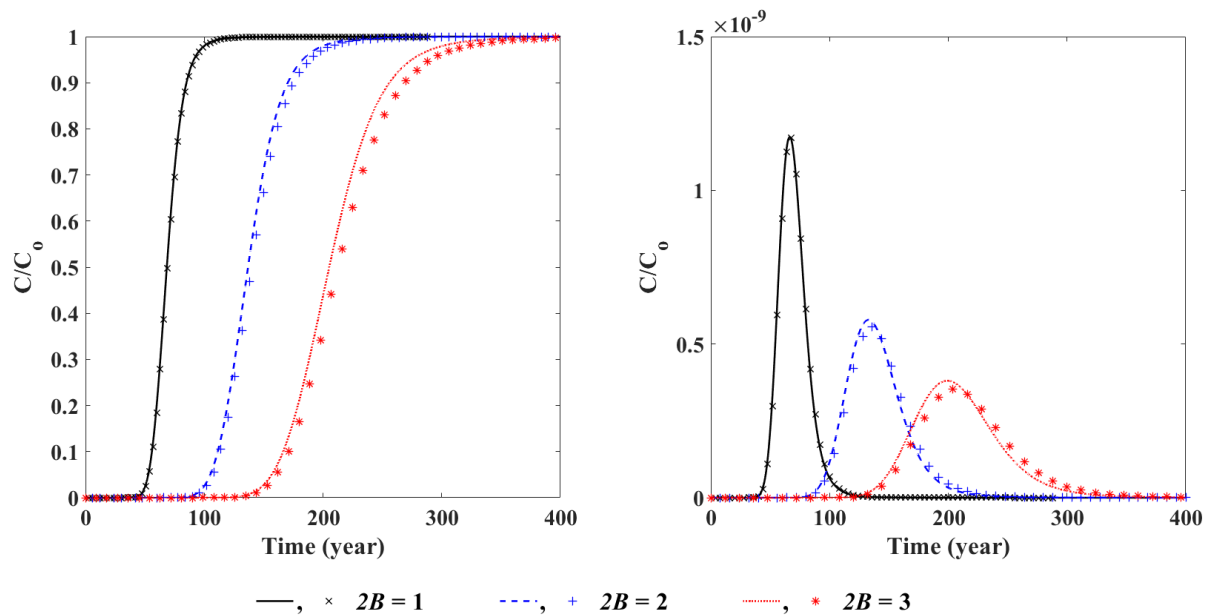


**Fig. 4-5: BTCs for Case 2 ( $\alpha = 5$  m;  $2b = 250$   $\mu$ m;  $2B = 1 - 3$  m;  $D^* = 1 \times 10^{-7}$  m<sup>2</sup>/sec;  $R_m = 1$ ;  $\theta = 0.1$ ;  $\tau = 1$ ) for (a) Type 1 and (b) Type 2 boundary conditions – lines represent AN model and symbols represent the developed model.**

The developed model simulations are then compared against those from the CFD model in DFN1 for Case 3 parameters ( $\alpha = 5$  m;  $2b = 250$   $\mu$ m;  $2B = 13.7$  m;  $D^* = 1 \times 10^{-7}$  m<sup>2</sup>/sec;  $R_m = 1$ ;  $\theta = 0.1$ ;  $\tau = 1$ ), excluding matrix retardation (i.e.,  $R_m = 1$ ), based on a Type 1 BC (**Fig. 4-6**). This comparison shows that when only transverse matrix dispersion is considered, the developed model significantly underrepresents dispersion. This is because when longitudinal matrix dispersion is neglected, reverse matrix diffusion (i.e., from the matrix back into the fracture) must occur at the same location as the original diffusion into the matrix. However, in real life applications, reverse matrix diffusion occurs at a location downstream of the original diffusion into the matrix as captured by the CFD model. Thus, the discrepancy between the developed and CFD models

demonstrates that longitudinal matrix diffusion is important. The developed model can approximate the results from the CFD model if a fracture dispersivity correction factor is employed to compensate for neglecting longitudinal diffusion in the matrix. In these simulations, the dispersivity correction factor was four (i.e., the validated longitudinal fracture dispersivity was four times that of the actual longitudinal dispersivity in the CFD model). However, the magnitude of the fracture dispersivity correction factor is dependent on several factors, including porewater velocity, fracture density, and fracture orientation. At low porewater velocities, transport is dominated by diffusion. Constituents will have more opportunity to diffuse into the matrix resulting in a larger dispersivity correction factor. Increasing fracture density results in shorter distances within the matrix for transverse diffusion to occur before reaching an adjacent fracture, where longitudinal diffusion will occur. This will result in smaller dispersivity correction factors. Finally, varying fracture orientations (with transverse matrix dispersion) results in a larger range of dispersivity directions, and therefore a smaller dispersivity correction factor. Given the range of parameters that affect the magnitude of the dispersivity correction factor, and the complexity of natural fracture networks, more research is required to determine the appropriate correction factor under a range of circumstances.

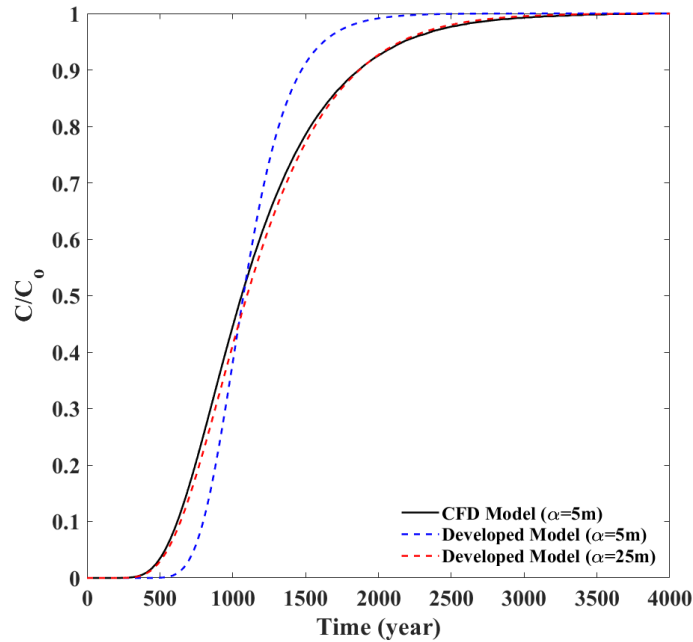


**Fig. 4-6: BTCs for Case 3 ( $\alpha = 5$  m;  $2b = 250$   $\mu\text{m}$ ;  $2B = 13.7$  m;  $D^* = 1 \times 10^{-7}$  m<sup>2</sup>/sec;  $R_m = 1$ ;  $\theta = 0.1$ ;  $\tau = 1$ ) for Type 1 BC calculated by the CFD model and the developed model.**

The spatial distribution of the solute concentration calculated by the validated developed model for Type 1 BC in DFN2 using Case 3 parameters ( $2b = 250$   $\mu\text{m}$ ;  $2B = 13.7$  m;  $D^* = 1 \times 10^{-7}$  m<sup>2</sup>/sec;  $R_m = 1$ ;  $\theta = 0.1$ ;  $\tau = 1$ ) using  $\alpha = 25$  m after 475 years is plotted alongside that obtained from the CFD model in **Fig. 4-7**. The comparison shows good agreement between the two models; however, the developed model fails to capture the solute concentration within the matrix blocks as it simulates solute transport in discrete fractures and interpolates the mass stored in the matrix based on adjacent fractures.

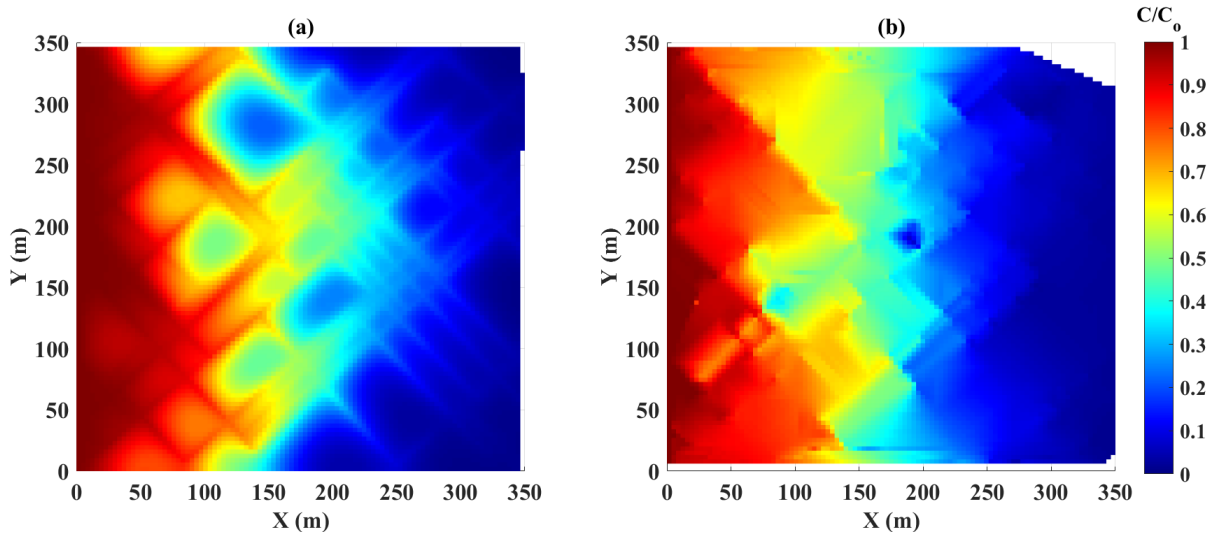


**Fig. 4-7: Spatial distribution of the solute concentration in DFN1 after 475 years from the time of release. Simulations are conducted using parameters for Case 3 ( $\alpha = 25$  m;  $2b = 250$   $\mu\text{m}$ ;  $2B = 13.7$  m;  $D^* = 1 \times 10^{-7}$  m<sup>2</sup>/sec;  $R_m = 1$ ;  $\theta = 0.1$ ;  $\tau = 1$ ) based on constant release (Type 1 BC) represented by (a) the CFD model using COMSOL and (b) the developed model.**

The spatial distribution of the solute mass simulated by the developed model for an injected mass of 10 kg in DFN2 using Case 1 parameters (**Table 4-1**;  $R_m = 1$  and 5) under a Type 2 influent BC is shown in **Fig. 4-8**. The results show that solute migration within the network is significantly slower when matrix diffusion is considered. When the retardation coefficient is large ( $R_m = 5$ ), the retention time in the matrix is larger relative to the fractures. This results in less longitudinal dispersion and higher peak concentrations in the fracture.

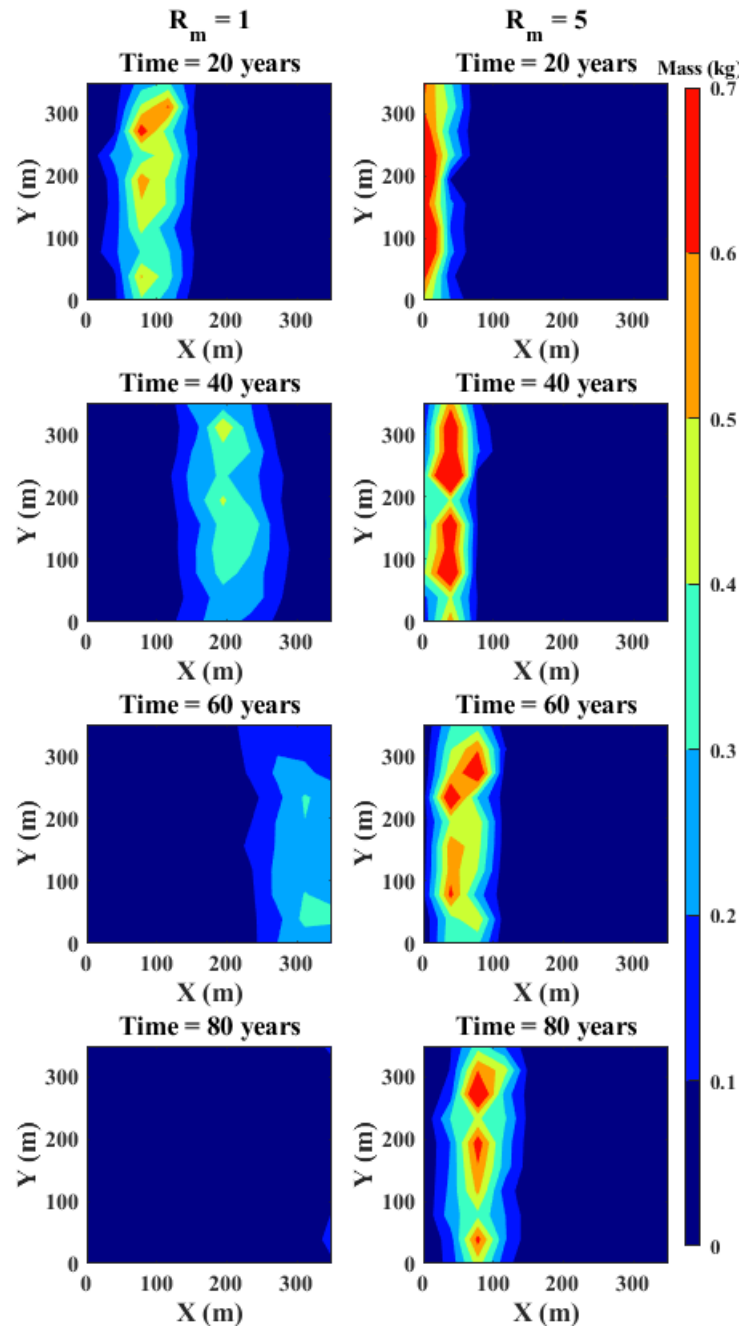


**Fig. 4-8: Spatial distribution of the solute mass in DFN 2 at 20, 40, 60, and 80 years from the time of release. Simulations are conducted using parameters for Case 1 ( $\alpha = 5$  m;  $2b = 250$   $\mu\text{m}$ ;  $2B = 1$  m;  $D^* = 1 \times 10^{-7}$   $\text{m}^2/\text{sec}$ ;  $R_m = 1$  and  $5$ ;  $\theta = 0.1$ ;  $\tau = 1$ ) based on a 10 kg pulse release (Type 2 BC).**

The impacts of diffusion, dispersivity, fracture aperture, and fracture spacing are assessed through multiple simulations conducted in DFN2 under a Type 2 BC for an injected mass of 10 kg. Each parameter is perturbed individually, and the results are compared to a base simulation using Case 1 parameters ( $\alpha = 5$  m;  $2b = 250$   $\mu\text{m}$ ;  $2B = 1$  m;  $D^* = 1 \times 10^{-7}$   $\text{m}^2/\text{sec}$ ;  $R_m = 1$ ;  $\theta = 0.1$ ;  $\tau = 1$ ) (**Fig. 4-9a**). The spatial distribution of mass based on changing the molecular diffusion coefficient ( $D^* = 1 \times 10^{-9}$   $\text{m}^2/\text{sec}$ ), dispersivity ( $\alpha = 10$  m), fracture aperture ( $2b = 400$   $\mu\text{m}$ ), and fracture spacing ( $2B = 0.5$  m) at  $t = 20$  years are presented in **Fig. 4-9a, b, c, and d**, respectively. It is observed that decreasing the effective diffusion coefficient facilitates mass migration (**Fig. 4-9a**), as lesser mass can diffuse into the matrix. The lower  $D^*$  also results in higher dispersion within the fracture, as lesser mass moves into the matrix. Increasing dispersivity causes slightly higher dispersion in the fracture (**Fig. 4-9c**). Increasing the fracture aperture, and decreasing the effective fracture spacing, lead to faster solute migration (**Fig. 4-9d** and **Fig. 4-9e**). The plume's centre of mass is about 80 m more advanced for the large fracture aperture case, and about 120 m more advanced for the small fracture spacing case.

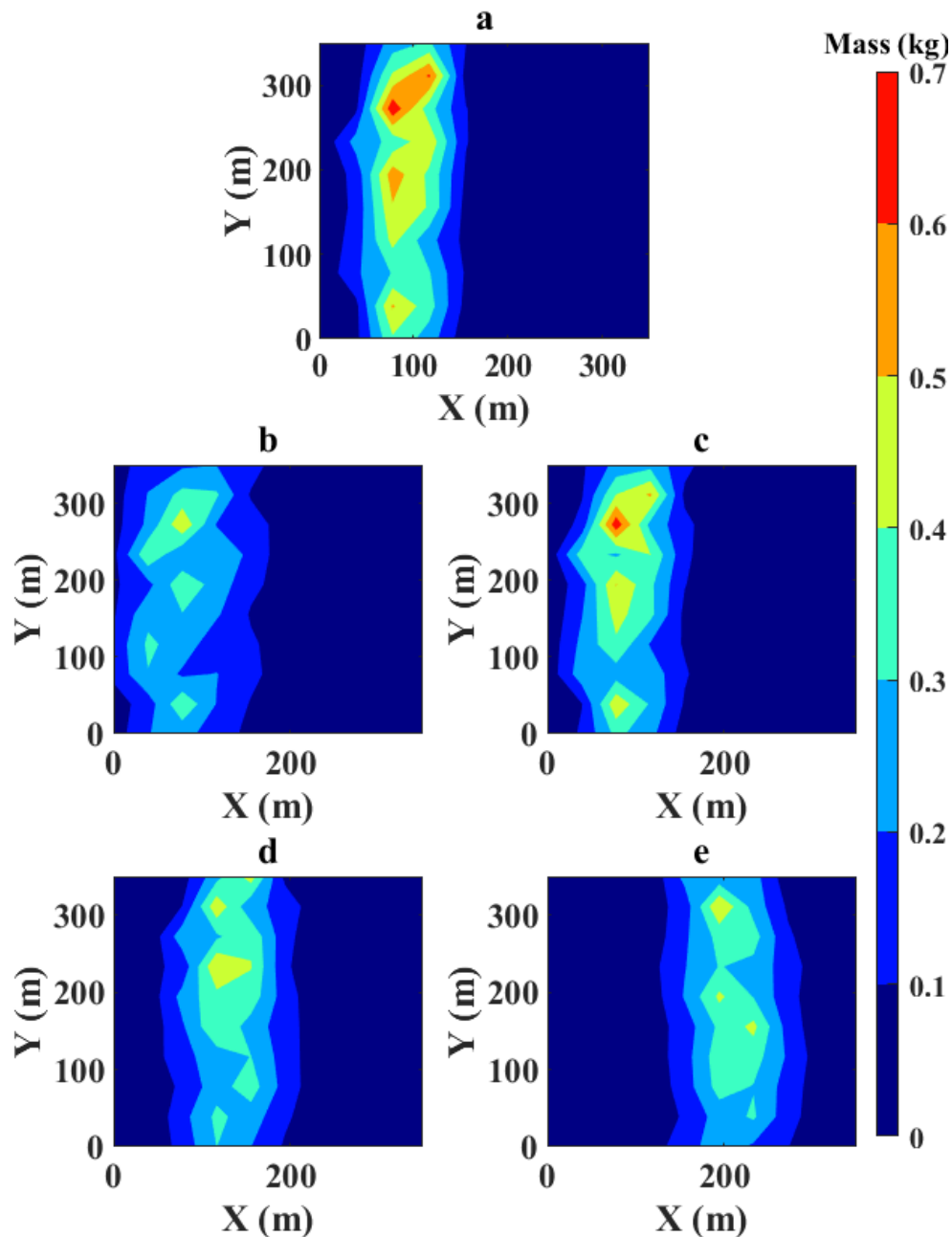


**Fig. 4-9: Effect of changing  $D^*$ ,  $\alpha$ ,  $2b$ , and  $2B$  on the spatial distribution of the solute mass in DFN2 (i.e., fractures and matrix). Panel (a) represents the base case at  $t = 20$  years based on Case 1 parameters ( $\alpha = 5$  m;  $2b = 250$   $\mu\text{m}$ ;  $2B = 1$  m;  $D^* = 1 \times 10^{-7}$   $\text{m}^2/\text{sec}$ ;  $R_m = 1$ ;  $\theta = 0.1$ ;  $\tau = 1$ ) under a Type 2 BC. Individual parameters are perturbed in panels (b)  $D^* = 1 \times 10^{-9}$   $\text{m}^2/\text{sec}$ , (c)  $\alpha = 10$  m, (d)  $2b = 400$   $\mu\text{m}$ , and (e)  $2B = 0.5$  m.**

The AN model predicts solute transport in DFN1 on the order of hours to arrive at a solution for Case 3 under Types 1 and 2 BCs (**Fig. 4-4**), while the developed model predicts the solute transport in the order of seconds for the same case. Therefore, the developed model solves the solute transport in approximately 250 times faster than the AN model—which was already shown to be an improvement over traditional time domain random walk and random walk particle tracking models (Khafagy et al., 2022a).

#### **4.5. Conclusion**

In this article, a hybrid model is developed to simulate the solute transport in fracture networks based on an extension of a MGGP solution for solute transport in a single fracture. The extension is achieved by applying the CM method for solute mass sharing at fracture intersections to form a solute injected BTC for each fracture inlet as an inlet BC in this fracture. Subsequently, the transfer function approach was applied between the injected BTC and the effluent BTC for the downstream fracture based on Type 2 BC. The developed model considers three mechanisms, with the ability of predicting solute transport at fracture intersections and at the network outlet for Type 1 and Type 2 BC. These mechanisms include advection and dispersion along the fracture; molecular diffusion within the fracture and into the matrix; and adsorption within the matrix

The model is compared to the analytical network (AN) model developed by Khafagy et al., (2022a) for DFN1 and the results indicated the developed model is approximately 250 times faster than the AN model. Furthermore, the model efficiency in predicting solute transport increases with network complexity compared to the AN model and other numerical models (i.e., TDRW and RWPT

approaches) (Khafagy et al., 2022a). Subsequently, the developed model is compared to the CFD model based on Navier Stokes equations for DFN1 and the comparison shows that the developed model has an obvious low dispersion compared to the CFD model. However, the developed model can approximately predict the solute transport as the CFD model when assuming a higher value of dispersivity which is highly affected by the fracture density in the fracture network. The high value of dispersivity in the developed model causes more solute dispersion that may overcome the neglect of the longitudinal matrix diffusion which is considered in the CFD model. However, it must be noted that these conclusions have been observed in the case studies proposed here (i.e., the DFN1) and the scaled value of dispersivity may be different for other fracture and matrix properties, especially, fracture orientations, fracture density. Finally, the numerical results of the DFN2 indicated that the low diffusion coefficient causes a long tail BTC at the outflow boundary of the network with smaller retention time of most of the solute, while small fracture aperture and large effective fracture spacings hinder the solute migration within the fracture network. Overall, the developed model will facilitate rapid simulations of solute transport in complex DFNs, while other models are computationally intensive to simulate the solute transport in such networks.

#### **4.6. Acknowledgment**

The financial support for the study was provided through the CaNRisk-CREATE program of the Natural Science and Engineering Research Council (NSERC) of Canada (Grant Number: CREAT-482707-2016).

#### 4.7. References

- Ahmed, R., Edwards, M.G., Lamine, S., Huisman, B.A.H., Pal, M., 2015. Control-volume distributed multi-point flux approximation coupled with a lower-dimensional fracture model. *J. Comput. Phys.* 284, 462–489. <https://doi.org/10.1016/j.jcp.2014.12.047>
- Akdas, S.B., Onur, M., 2022. Analytical solutions for predicting and optimizing geothermal energy extraction from an enhanced geothermal system with a multiple hydraulically fractured horizontal-well doublet. *Renew. Energy* 181, 567–580. <https://doi.org/10.1016/j.renene.2021.09.051>
- Alexandrov, B.L., Zakharchenko, E.I., Moskalenko, I. V., Elzhaev, A.S., 2020. The nature of the formation in clay strata of oil and gas saturated fractured reservoirs. *IOP Conf. Ser. Earth Environ. Sci.* 579. <https://doi.org/10.1088/1755-1315/579/1/012001>
- Bear, J., 1972. *Dynamics of Fluids in Porous Media*. New York, Dover Publ. 1–783.
- Berre, I., Doster, F., Keilegavlen, E., 2019. Flow in Fractured Porous Media: A Review of Conceptual Models and Discretization Approaches. *Transp. Porous Media* 130, 215–236. <https://doi.org/10.1007/s11242-018-1171-6>
- Bodin, J., Porel, G., Delay, F., Ubertosi, F., Bernard, S., de Dreuzy, J.R., 2007. Simulation and analysis of solute transport in 2D fracture/pipe networks: The SOLFRAC program. *J. Contam. Hydrol.* 89, 1–28. <https://doi.org/10.1016/j.jconhyd.2006.07.005>
- Chen, K., Zhan, H., 2018. A Green's function method for two-dimensional reactive solute transport in a parallel fracture-matrix system. *J. Contam. Hydrol.* 213, 15–21.

<https://doi.org/10.1016/j.jconhyd.2018.03.006>

Chittenden, N., McDermott, C.I., Bond, A.E., Wilson, J., Norris, S., 2016. Evaluating the importance of different coupled thermal, hydraulic, mechanical and chemical process simulations during fluid flow experiments in fractured novaculite and fractured granite.

*Environ. Earth Sci.* 75, 1–18. <https://doi.org/10.1007/s12665-016-5938-1>

Cvetkovic, V., Frampton, A., 2012. Solute transport and retention in three-dimensional fracture networks. *Water Resour. Res.* 48, 1–11. <https://doi.org/10.1029/2011WR011086>

Dong, S., Zeng, L., Dowd, P., Xu, C., Cao, H., 2018. A fast method for fracture intersection detection in discrete fracture networks. *Comput. Geotech.* 98, 205–216.

<https://doi.org/10.1016/j.compgeo.2018.02.005>

Eidesgaard, R., Schovsbo, N.H., Boldreel, L.O., Ólavsdóttir, J., 2019. Shallow geothermal energy system in fractured basalt: A case study from Kollafjørður, Faroe Islands, NE-Atlantic Ocean. *Geothermics* 82, 296–314. <https://doi.org/10.1016/j.geothermics.2019.07.005>

Feng, S., Wang, Hanqing, Cui, Y., Ye, Y., Liu, Y., Li, X., Wang, Hong, Yang, R., 2020. Fractal discrete fracture network model for the analysis of radon migration in fractured media.

*Comput. Geotech.* 128, 103810. <https://doi.org/10.1016/j.compgeo.2020.103810>

Frampton, A., Hyman, J.D., Zou, L., 2019. Advective Transport in Discrete Fracture Networks With Connected and Disconnected Textures Representing Internal Aperture Variability.

*Water Resour. Res.* 55, 5487–5501. <https://doi.org/10.1029/2018WR024322>

Hawez, H.K., Sanaee, R., Faisal, N.H., 2021. A critical review on coupled geomechanics and fluid

flow in naturally fractured reservoirs. *J. Nat. Gas Sci. Eng.* 95, 104150.  
<https://doi.org/10.1016/j.jngse.2021.104150>

Howroyd, M., Novakowski, K.S., 2022. Allocating transmissivities from constant head tests for the development of DFN models. *Can. Geotech. J.* 59, 87–100. <https://doi.org/10.1139/cgj-2020-0699>

Hu, Y., Xu, W., Zhan, L., Zou, L., Chen, Y., 2022. Modeling of solute transport in a fracture-matrix system with a three-dimensional discrete fracture network. *J. Hydrol.* 605, 127333.  
<https://doi.org/10.1016/j.jhydrol.2021.127333>

Hyman, J.D., Rajaram, H., Srinivasan, S., Makedonska, N., Karra, S., Viswanathan, H., Srinivasan, G., 2019. Matrix Diffusion in Fractured Media: New Insights Into Power Law Scaling of Breakthrough Curves. *Geophys. Res. Lett.* 46, 13785–13795.  
<https://doi.org/10.1029/2019GL085454>

Iraola, A., Trinchero, P., Karra, S., Molinero, J., 2019. Assessing dual continuum method for multicomponent reactive transport. *Comput. Geosci.* 130, 11–19.  
<https://doi.org/10.1016/j.cageo.2019.05.007>

Jing, L., Min, K.B., Baghbanan, A., Zhao, Z., 2013. Understanding coupled stress, flow and transport processes in fractured rocks. *Geosystem Eng.* 16, 2–25.  
<https://doi.org/10.1080/12269328.2013.780709>

Jongkittinarukorn, K., Escobar, F.H., Ramirez, D.M., Suescún-Díaz, D., 2021. Practical interpretation of pressure tests of hydraulically fractured vertical wells with finite-

conductivity in naturally fractured oil and gas formations. *J. Pet. Explor. Prod.* 11, 3277–3288. <https://doi.org/10.1007/s13202-021-01228-9>

Ju, Y.J., Massoudieh, A., Kaown, D., Yoon, Y.Y., Lee, K.K., 2020. Characterization of flow dynamics around highly-utilized agricultural wells in a fractured-rock aquifer: Assessment of uncertainties lying on groundwater age-dating. *J. Hydrol.* 586, 124885. <https://doi.org/10.1016/j.jhydrol.2020.124885>

Khafagy, M., El-Dakhakhni, W., Dickson-Anderson, S., 2022a. Multi-gene genetic programming expressions for simulating solute transport in fractures. *J. Hydrol.* 606, 127316. <https://doi.org/10.1016/j.jhydrol.2021.127316>

Khafagy, M., El-Dakhakhni, W., Dickson-Anderson, S., 2022b. Analytical model for solute transport in discrete fracture networks: 2D spatiotemporal solution with matrix diffusion. *Comput. Geosci.* 159, 104983. <https://doi.org/10.1016/j.cageo.2021.104983>

Larsson, M., Odén, M., Niemi, A., Neretnieks, I., Tsang, C.F., 2013. A new approach to account for fracture aperture variability when modeling solute transport in fracture networks. *Water Resour. Res.* 49, 2241–2252. <https://doi.org/10.1002/wrcr.20130>

Lei, Q., Latham, J.P., Tsang, C.F., 2017. The use of discrete fracture networks for modelling coupled geomechanical and hydrological behaviour of fractured rocks. *Comput. Geotech.* 85, 151–176. <https://doi.org/10.1016/j.compgeo.2016.12.024>

Li, X. wen, Li, J. ye, Liu, Y. lei, Ma, P. ling, Bi, J. ying, Zhang, X. wang, Chen, Y. ren, Jia, C. zi, Wang, Z. ao, 2021. Quantitative Azimuthal AVO Detection Method for Oil and Gas Analysis

of Deep Buried Fractured-Vuggy Reservoir, Springer Series in Geomechanics and Geoengineering. Springer Singapore. [https://doi.org/10.1007/978-981-16-0761-5\\_204](https://doi.org/10.1007/978-981-16-0761-5_204)

Liu, R., Jiang, Y., Li, B., Wang, X., 2015. A fractal model for characterizing fluid flow in fractured rock masses based on randomly distributed rock fracture networks. *Comput. Geotech.* 65, 45–55. <https://doi.org/10.1016/j.compgeo.2014.11.004>

Mahmoud, H.H., Kotb, A.D.M., Tawfik, M.Z., 2021. Application of Time Domain Electromagnetic survey to detect fractured limestone aquifer in desert fringes, West Assiut, Egypt. *NRIAG J. Astron. Geophys.* 10, 235–243. <https://doi.org/10.1080/20909977.2021.1913393>

Maillot, J., Davy, P., Le Goc, R., Darcel, C., de Dreuzy, J.R., 2016. Connectivity, permeability, and channeling in randomly distributed and kinematically defined discrete fracture network models. *Water Resour. Res.* 52, 8526–8545. <https://doi.org/10.1002/2016WR018973>

Makungo, R., Odiyo, J.O., Ndiritu, J.G., 2021. Hydraulic characteristics of a fractured crystalline basement aquifer in Nzhelele area, Limpopo Province, South Africa. *Cogent Eng.* 8. <https://doi.org/10.1080/23311916.2021.1928387>

Metcalf, R., Milodowski, A.E., Field, L.P., Wogelius, R.A., Carpenter, G., Yardley, B.W.D., Norris, S., 2021. Natural analogue evidence for controls on radionuclide uptake by fractured crystalline rock. *Appl. Geochemistry* 124. <https://doi.org/10.1016/j.apgeochem.2020.104812>

Miao, T., Yu, B., Duan, Y., Fang, Q., 2015. A fractal analysis of permeability for fractured rocks.

Int. J. Heat Mass Transf. 81, 75–80. <https://doi.org/10.1016/j.ijheatmasstransfer.2014.10.010>

Mohammadi, Z., Illman, W.A., Field, M., 2021. Review of Laboratory Scale Models of Karst Aquifers: Approaches, Similitude, and Requirements. *Groundwater* 59, 163–174. <https://doi.org/10.1111/gwat.13052>

Nakayama, H., Yamasaki, Y., Ohashi, K., Nakaya, S., 2021. Simple method for estimating well yield potential through geostatistical approach in fractured crystalline rock formations. *J. Hydrol.* 597, 125719. <https://doi.org/10.1016/j.jhydrol.2020.125719>

Nguyen, M.C., Dejam, M., Fazelalavi, M., Zhang, Y., Gay, G.W., Bowen, D.W., Spangler, L.H., Zaluski, W., Stauffer, P.H., 2021. Skin factor and potential formation damage from chemical and mechanical processes in a naturally fractured carbonate aquifer with implications to CO<sub>2</sub> sequestration. *Int. J. Greenh. Gas Control* 108, 103326. <https://doi.org/10.1016/j.ijggc.2021.103326>

Paradis, D., Ballard, J.M., Lefebvre, R., Savard, M.M., 2018. Transport multi-échelle des nitrates dans un système aquifère de grès soumis à une agriculture intensive. *Hydrogeol. J.* 26, 511–531. <https://doi.org/10.1007/s10040-017-1668-z>

Rezaei, A., Zare, M., 2016. Aquitard Horizontal Dispersion on Reactive Solute Transport in an Aquifer – Aquitard System. *Transp. Porous Media* 113, 695–716. <https://doi.org/10.1007/s11242-016-0719-6>

Schill, E., Genter, A., Cuenot, N., Kohl, T., 2017. Hydraulic performance history at the Soultz EGS reservoirs from stimulation and long-term circulation tests. *Geothermics* 70, 110–124.

<https://doi.org/10.1016/j.geothermics.2017.06.003>

Sharma, S., Agrawal, V., McGrath, S., Hakala, J.A., Lopano, C., Goodman, A., 2021. Geochemical controls on CO<sub>2</sub> interactions with deep subsurface shales: Implications for geologic carbon sequestration. *Environ. Sci. Process. Impacts* 23, 1278–1300. <https://doi.org/10.1039/d1em00109d>

Somogyvári, M., Jalali, M., Jimenez Parras, S., Bayer, P., 2017. Synthetic fracture network characterization with transdimensional inversion. *Water Resour. Res.* 53, 5104–5123. <https://doi.org/10.1002/2016WR020293>

Sornette, A., Davy, P., Sornette, D., 1990. Growth of fractal fault patterns. *Phys. Rev. Lett.* 65, 2266–2269. <https://doi.org/10.1103/PhysRevLett.65.2266>

Stein, E.R., Frederick, J.M., Hammond, G.E., Kuhlman, K.L., Mariner, P.E., Sevougian, S.D., 2017. Modeling coupled reactive flow processes in fractured crystalline rock, in: ANS IHLRWM 2017 - 16th International High-Level Radioactive Waste Management Conference: Creating a Safe and Secure Energy Future for Generations to Come - Driving Toward Long-Term Storage and Disposal. pp. 145–155.

Sudicky, E.A., Frind, E.O., 1982. Contaminant transport in fractured porous media: Analytical solutions for a system of parallel fractures. *Water Resour. Res.* 18, 1634–1642. <https://doi.org/10.1029/WR018i006p01634>

Viswanathan, H.S., Hyman, J.D., Karra, S., O'Malley, D., Srinivasan, S., Hagberg, A., Srinivasan, G., 2018. Advancing Graph-Based Algorithms for Predicting Flow and Transport in

Fractured Rock. Water Resour. Res. 54, 6085–6099.

<https://doi.org/10.1029/2017WR022368>

Wang, L., Cardenas, M.B., 2014. Non-Fickian transport through two-dimensional rough fractures: Assessment and prediction. Water Resour. Res. 50, 871–884.

<https://doi.org/10.1002/2013WR014459>

Wang, L., Cardenas, M.B., Zhou, J.Q., Ketcham, R.A., 2020. The Complexity of Nonlinear Flow and non-Fickian Transport in Fractures Driven by Three-Dimensional Recirculation Zones. J. Geophys. Res. Solid Earth 125, 1–14. <https://doi.org/10.1029/2020JB020028>

Watson, C., Wilson, J., Savage, D., Benbow, S., Norris, S., 2016. Modelling reactions between alkaline fluids and fractured rock: The Maqarin natural analogue. Appl. Clay Sci. 121–122, 46–56. <https://doi.org/10.1016/j.clay.2015.12.004>

Wei, C., Cheng, S., She, J., Gao, R., Luo, L., Yu, H., 2021. Numerical study on the heat transfer behavior in naturally fractured reservoirs and applications for reservoir characterization and geothermal energy development. J. Pet. Sci. Eng. 202, 108560. <https://doi.org/10.1016/j.petrol.2021.108560>

Wu, H., Jayne, R.S., Bodnar, R.J., Pollyea, R.M., 2021. Simulation of CO<sub>2</sub> mineral trapping and permeability alteration in fractured basalt: Implications for geologic carbon sequestration in mafic reservoirs. Int. J. Greenh. Gas Control 109, 103383. <https://doi.org/10.1016/j.ijggc.2021.103383>

Zakharova, N. V., Goldberg, D.S., Olsen, P.E., Collins, D., Kent, D. V., 2020. Reservoir and

sealing properties of the Newark rift basin formations: Implications for carbon sequestration.

Lead. Edge 39, 38–46. <https://doi.org/10.1190/tle39010038.1>

Zhang, Y., Labolle, E.M., Reeves, D.M., Russell, C., 2013. Direct numerical simulation of matrix diffusion across fracture/matrix interface. *Water Sci. Eng.* 6, 365–379.

<https://doi.org/10.3882/j.issn.1674-2370.2013.04.001>

Zhao, Z., Jing, L., Neretnieks, I., Moreno, L., 2011. Numerical modeling of stress effects on solute transport in fractured rocks. *Comput. Geotech.* 38, 113–126.

<https://doi.org/10.1016/j.compgeo.2010.10.001>

Zhao, Z., Rutqvist, J., Leung, C., Hokr, M., Liu, Q., Neretnieks, I., Hoch, A., Havlíček, J., Wang, Y., Wang, Z., Wu, Y., Zimmerman, R., 2013. Impact of stress on solute transport in a fracture network: A comparison study. *J. Rock Mech. Geotech. Eng.* 5, 110–123.

<https://doi.org/10.1016/j.jrmge.2013.01.002>

Zhou, R., Zhan, H., Chen, K., 2017. Reactive solute transport in a filled single fracture-matrix system under unilateral and radial flows. *Adv. Water Resour.* 104, 183–194.

<https://doi.org/10.1016/j.advwatres.2017.03.022>

Zhu, Y., Zhan, H., Jin, M., 2016. Analytical solutions of solute transport in a fracture–matrix system with different reaction rates for fracture and matrix. *J. Hydrol.* 539, 447–456.

<https://doi.org/10.1016/j.jhydrol.2016.05.056>

Zimmerman, W.B.J., 2006. INTRODUCTION TO COMSOL MULTIPHYSICS. pp. 1–26.

[https://doi.org/10.1142/9789812773302\\_0001](https://doi.org/10.1142/9789812773302_0001)

Zou, L., Jing, L., Cvetkovic, V., 2017. Modeling of flow and mixing in 3D rough-walled rock fracture intersections. *Adv. Water Resour.* 107, 1–9.  
<https://doi.org/10.1016/j.advwatres.2017.06.003>

## **Chapter 5: Computationally efficient upscaled model for simulating solute transport in complex large-scale fracture networks**

This chapter presents the development of an Upscaled Fracture Network (UFN) model employing random walk particle tracking (RWPT) in a DFN. The UFN model accurately captures solute transport processes occurring at the macroscopic scale in saturated fracture networks. The UFN model involves discretizing a complex fracture network into elementary volumes, within which both representative solute transport flow channels and their corresponding breakthrough curves were identified. This identified flow channels were then employed to construct the residence time at the macroscopic scale. The UFN model represents a significant advancement in simulating solute transport in complex, regional aquifers due to its computational efficiency, simple implementation, and high level of accuracy.

Authors: M. Khafagy, S. E. Dickson-Anderson, W. El-Dakhakhni

Journal: Water Resources Research

Status: Will be submitted in July

### **Chapter 5 Contributions:**

Mohamed Khafagy: Conceptualization, Methodology, Software, Formal analysis, Writing, and Original draft preparation.

Sarah Dickson-Anderson: Writing & Review & Editing, Supervision, and Funding acquisition.

Wael El-Dakhakhni: Writing & Review & Editing, Supervision, and Funding acquisition.

## **Abstract**

Currently, the most common approaches for simulating solute transport in fractured aquifers are the continuum and the discrete fracture network (DFN) methods. However, continuum approaches often lack accuracy due to averaging, whereas DFN approaches may be computationally prohibitive for large-scale fracture networks. To address these challenges, this study presents an Upscaled Fracture Network (UFN) model, developed using random walk particle tracking (RWPT) in a DFN. The UFN model discretizes a complex fracture network into elementary volumes, within which the representative solute transport flow channels are identified, and their corresponding breakthrough curves are calculated. The identified flow channels within each elementary volume are collectively employed to construct the residence time at the macro-scale. Validated using RWPT DFN-based approaches, the UFN model can accurately capture solute transport processes occurring at the macro scale in saturated fracture networks, and represents a significant advancement in simulating solute transport in complex, regional aquifers due to its computational efficiency, simple implementation, and high level of accuracy.

**Key words:** Discrete fracture networks, Subsurface transport, Upscaling, Particle tracking.

## 5.1. Introduction

Solute transport modeling through fracture networks is of extreme importance to predict groundwater system behaviors (Sweeney et al., 2020) due to the rising global concern on subsurface contamination and pollution due to escalation in various engineering operations such as radioactive waste disposal (e.g., Alzamel et al., 2022; Karolytè et al., 2022; Malkovsky and Yudinsev, 2022), percolation of leachate from landfills (e.g., Brunella and Raffaele, 2022; Javahershenas et al., 2022; Wang et al., 2022), coastal water intrusion (e.g., Luo et al., 2022; Tran et al., 2022; Yuan et al., 2022), oil spill (e.g., Kalibatiene and Burmakova, 2022; Mallants et al., 2022; Scanlon et al., 2022), exploitation of petroleum (e.g., Demenev et al., 2022; Li et al., 2022; Wei et al., 2022), gas and geothermal reservoirs (e.g., Morais et al., 2022; Ryu et al., 2022; Zhao et al., 2022), fluid pressure studies in deforming the rock (e.g., An et al., 2022; Wang et al., 2022), seepage process in mining and dams (e.g., Adamovic et al., 2022; Singha et al., 2022; Xu et al., 2022) etc. Various modeling approaches have been employed, which can be broadly divided into continuum (single or multiple) and discrete fracture models (Zhang et al., 2022). In single-continuum (equivalent parameters-based) models, individual fracture properties are translated into those of an equivalent porous medium without considering the surrounding matrix. On the other hand, multiple-continuum models (e.g., dual-continuum), allow for the approximate description of transport phenomena at large scales with the consideration of the surrounding matrix as a different continuum. However, these models may fail to capture non-Fickian features that small-scale models are able to (Benke and Painter, 2003; Painter et al., 2002). Such multiple-continuum models assume uniform dispersion — an assumption that may not always be valid in fractured

networks where flow and transport occur in discrete channels (Benke and Painter, 2003; Painter et al., 2002) and may reflect an inaccurate relationship between dispersivity ( $\alpha$ ) and scale (Bechtold et al., 2011). Additionally, continuum approaches may result in significant biases in when more heterogeneous fracture network geometries exist (Viswanathan et al., 2018).

Discrete fracture approaches reduce these biases by considering heterogeneous fracture geometries. Numerous discrete fracture approaches have been developed, which can be divided into three categories: 1) the discrete fracture network (DFN) model (Feng et al., 2020; Jiang et al., 2021; Khafagy et al., 2022, 2020; Yao et al., 2020); 2) the discrete fracture-matrix (DFM) model (Chen et al., 2020; Flemisch et al., 2018; Ma et al., 2018; Sandve et al., 2012; Sweeney et al., 2020); and, 3) the continuum fracture (CF) model (Dong et al., 2019; Khoei et al., 2020; L. Wang et al., 2020; Wu et al., 2022).

In the DFN approach, fracture geometry and hydraulic parameters are explicitly represented either as lines in two dimensions or planar polygons in three dimensions (Hyman et al., 2019; Maillot et al., 2016), which allow handling the high degree of complexity and heterogeneity of the networks (Sweeney et al., 2020). DFN models have been used to simulate a variety of important problems such as unconventional oil and gas extraction and nuclear waste repositories, which are representative of environments with relatively low fracture densities. (Follin et al. 2014; Cuss et al. 2015; Wang et al. 2016; Day-Lewis et al. 2017; Zhang et al. 2017; Bishop et al. 2020). These methods solve the flow and transport equations in individual fractures considering both anisotropy and stochasticity (Dippenaar et al., 2019; Wang et al., 2018); however, they do not consider

fracture-matrix interactions. Despite their known accuracy and robustness, DFN models are highly complex and computationally demanding compared to continuum models, which limit their adoption for macro-scale analyses (Iraola et al., 2019; Trinchero and Iraola, 2020). This is particularly true for 3D DFN models.

In contrast to DFN modeling, DFM models provide explicit representations of both the fracture network and surrounding porous matrix (Berre et al., 2019). DFM models are relatively new compared to DFN and continuum models, and thus require further development to facilitate their implementation (Sweeney et al., 2020). In general, a DFM model seeks to represent the fracture network as  $(n - 1)$ -dimension features coupled with a  $(n)$ -dimensional mesh representing the rock matrix. For example, a fracture can be represented as a polygon in a 3D grid, or a segment in a 2D grid. In addition, the fracture geometry must coincide with the matrix grid, where, due to the fracture spatial randomness, irregular grids must be employed in the DFM model. Since the fracture is distinct from the matrix, most of fracture parameters can be captured by the DFM model, and therefore the model accuracy is enhanced compared to DFN approaches. Nonetheless, one of the disadvantages of DFM models lies in the inability to handle stochastically generated networks with low angle fractures intersections. Additionally, meshing challenges materialize when two fractures in close proximity do not intersect (Berre et al., 2019). The primary challenges associated with modeling solute transport at the macro scale are underpinned by the ability to represent transport in fractures through coupling transport in fractures with transport in the surrounding matrix while preserving complex network geometries. Furthermore, the meshes associated with DFM models are inherently multidimensional, which further complicates solving the governing

equations of flow and transport. Therefore, at the macro scale, the computational cost of DFM model simulations is not justifiable—limiting the use of DFM models in such applications.

Both the DFN and DFM models are discrete models with a key feature being the distinction between the fracture and the matrix. However, fractures can also be deemed a special case of porous rock matrix in which the porosity and permeability are very high. With this understanding, fractures can be treated as a porous medium in DFM models, where the fractures are considered zones of high porosity and permeability compared to the matrix zones (Ahmed et al., 2019). As a result, a uniform grid size can be used in the model, resulting in a significantly reduced computational cost than DFN and DFM models. However, detailed fracture mapping and characterization to obtain the data required for these models is often not feasible due to the high degree of network complexity and heterogeneity. As such, information on geometric characteristics is typically obtained based on probability distributions and correlation functions (Wang et al. 2020). As such, there is a critical need for methods to bridge the spatial-scale gap between the typical DFN and regional scales.

## **5.2. Objectives**

In this paper, we describe a new approach for regional-scale simulation of transport in fractured rock based on upscaling the results from DFN simulations. Specifically, we use particle tracking in relatively small DFN domains to extract the relevant information required to identify flow and transport pathways (i.e., flow channels (FC)), and thus conduct transport simulations at the macro scale. The developed Upscaled Fracture Network (UFN) model generates representative FCs

employing random walk particle tracking (RWPT) to obtain the solute migration behavior in a representative micro-scale DFN to achieve upscaling.

### **5.3. Model Development**

The UFN model calculates solute transport in a micro-scale fracture network, which is then upscaled to a macro-scale network, and potentially to a regional-scale network. The UFN model development requires the flow boundary conditions to be downscaled from the regional-scale aquifer to the micro-scale. The first stage of the model (**Fig. 5-1**) involves dividing the micro-scale network into equal elementary volumes and a RWPT-based model is used to simulate solute transport to generate simple representative flow channels (FCs) at the micro scale. In the second stage of the model (**Fig. 5-1**), the representative FCs are upscaled to the macro-scale network. The third and final stage of the model involves simulating solute transport at the macro scale, based on the upscaled FCs, using the RWPT model. The rationale behind the UFN model development is that it is easier to obtain an accurate rapid solution at smaller scales and sequentially upscale the results than it is to obtain a solution directly at a larger scale.

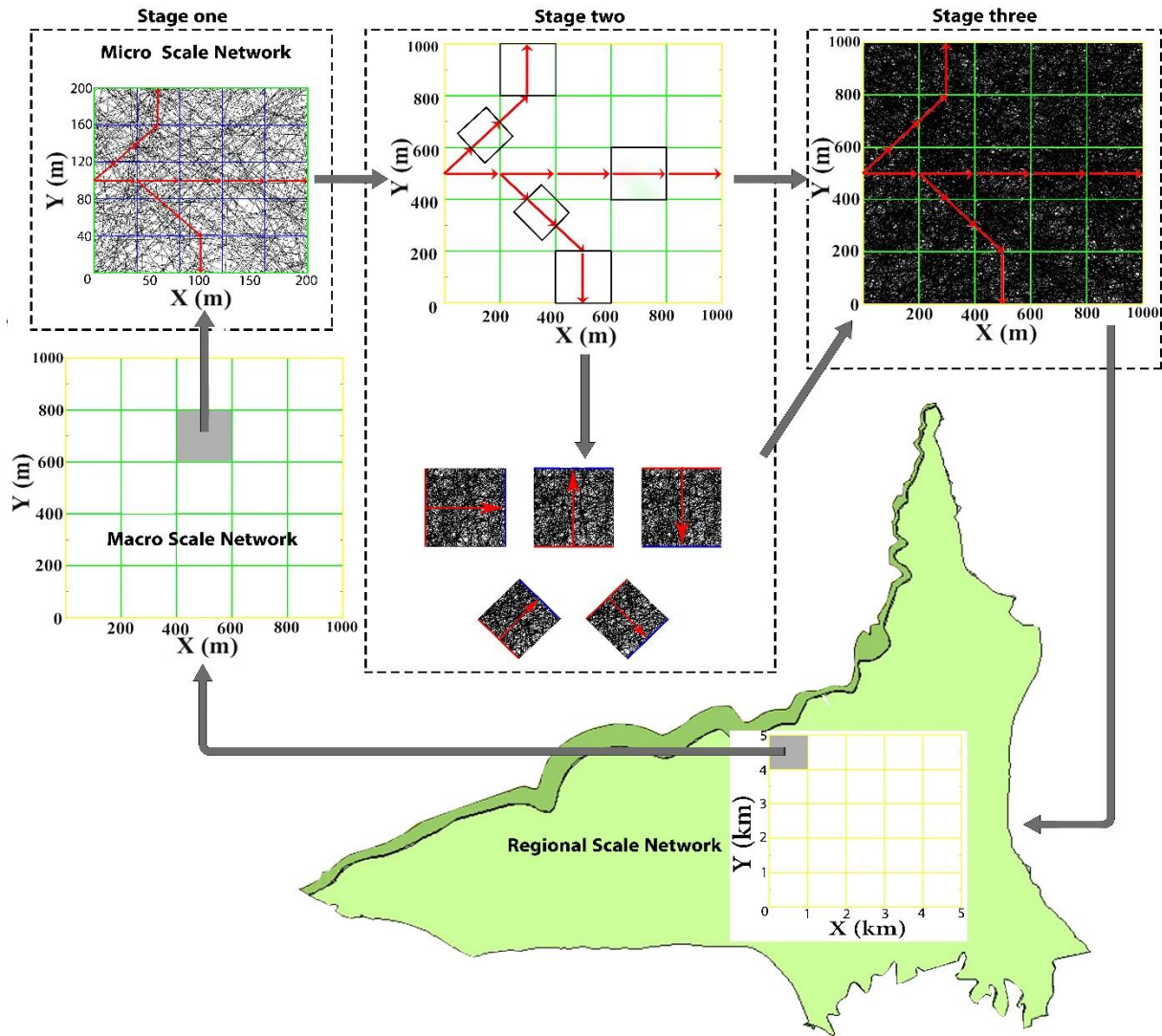


**Fig. 5-1: Illustration of the model at different scales (i.e., micro, macro, and regional network scales). Note the FCs (identified by red arrows) are upscaled from the micro to macro to regional scales.**

### 5.3.1 Steady State Flow Simulation

The steady state flow solution is obtained, at the scale of interest, in the DFN prior to simulating solute transport. The solute in the RWPT-based model is represented as particles that are injected at specified locations and migrate along individual fractures within the network. The transport mechanisms considered in this RWPT model are advection and dispersion. For simulating flow and transport in 2D DFNs, fractures are represented as line segments and are generated by sampling values for position, orientation, length, and aperture from statistical probability distributions. The DFN used in the simulations conducted here is shown in **Fig. 5-2**, and the distributions and other parameters used for the simulation setup are provided in **Table 5-1** (Ahmed et al., 2019). Once the fracture network is created, fracture intersections are identified. Since we are simulating a fully saturated network, flow is considered to only occur through the set of fractures that are hydraulically connected to the inflow and outflow boundaries. Therefore, any fracture disjointed from the flow system is removed, which results in only maintaining the conductive fractures in the network. Subsequently, by assuming conservation of mass at each fracture intersection, flow balance equations can be employed. The latter results in a system of linear pressure equations, where the pressure at each intersection is unknown, whereas the transmissivity between each pair of intersections is known and obtained from the characteristics of the fracture segment connecting the two intersections. By enforcing a boundary condition in the form of a pressure gradient (**Fig. 5-2**) across two or more intersections (0.01 m/m), the system of flow equations can be solved, and subsequently the pressure at every internal intersection in the system can be established.

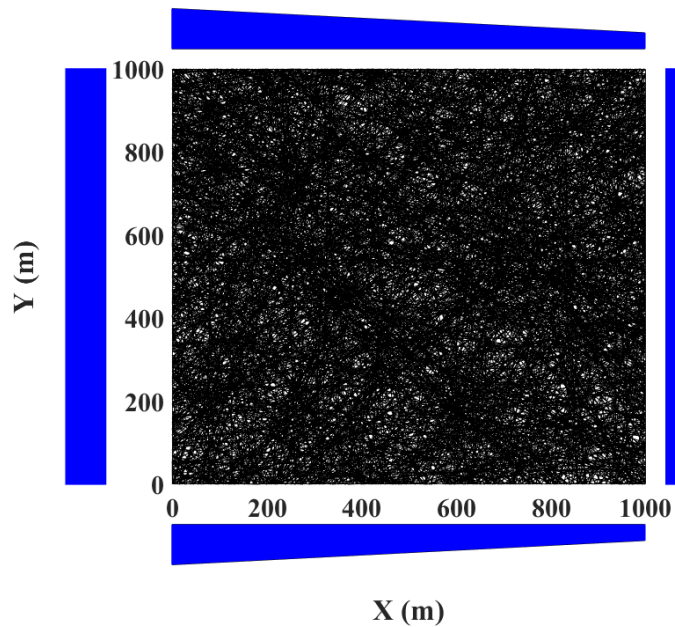


**Fig. 5-2: The macro scale network used in the simulation showing the hydraulic head along each boundary (i.e., quadrilateral). All dead-end and isolated fractures have been removed.**

The flow between intersections depends on how transmissivity in the fracture is calculated. Steady state flow and a linear pressure drop between each pair of connecting intersections was assumed, so that the equation governing flow presents the one-dimensional version of the Navier-Stokes equations (cubic law) (Snow, 1965).

$$Q = \frac{(2b)^3 \Delta p}{12\mu l} \quad (5-1)$$

where  $Q$  is flow through the fracture,  $2b$  is the aperture,  $\mu$  is the fluid viscosity, and  $\Delta p$  is the local pressure drop along the fracture with length  $l$ . This equation assumes steady-state, laminar flow through parallel plates, an averaged velocity profile across the aperture, and isothermal conditions.

**Table 5-1: Simulation parameters**

<b>Parameter</b>	<b>Values/Distributions</b>
Domain size	1000 × 1000 m <sup>2</sup>
Hydraulic gradient	0.01 m/m
Fracture density	1.26 m/m <sup>2</sup>
<b>Fracture property</b>	<b>Values/Distributions</b>
Position	Uniform throughout domain
Fracture orientation	Uniform over all angles
Fracture length ( <i>l</i> )	Lognormally distributed with $E(\ln(l)) = 10$ $Var(\ln(l)) = 0.1$ ( <i>l</i> in units of m)
Fracture aperture	0.00025 m
Dispersivity	1 m and 5 m

The micro-scale network (200 × 200 m<sup>2</sup>) is then extracted from the macro-scale network (1000 × 1000 m<sup>2</sup>) to calculate flow for the parameters shown in **Table 5-1**.

### 5.3.2 Solute Transport Using RWPT

The transport of particles is simulated in the micro-scale network using the RWPT model developed by (Khafagy et al., 2020), which is able to consider any combination of the following solute transport processes: advection, hydrodynamic dispersion, sorption on the fracture walls, sorption in the matrix, and matrix diffusion. The RWPT model is a solution for the advection-dispersion equation in fracture-matrix systems as follows:

$$\frac{\partial c}{\partial t} + \frac{v}{R} \frac{\partial c}{\partial z} - \frac{D}{R} \frac{\partial^2 c}{\partial z^2} + \lambda c - \frac{\theta D'}{bR} \frac{\partial c'}{\partial x} \Big|_{x=b} = 0 \quad (5-2)$$

where *c* and *c'* [M/L<sup>3</sup>] are the concentrations of solute in fracture and porous matrix, respectively,

$z$  [L] is the fracture length,  $x$  [L] is the coordinate perpendicular to the fracture axis with the origin at the centerline of the fracture [L],  $v$  [L/T] is groundwater velocity in the fracture,  $2b$  [L] is the aperture width,  $D$  [L<sup>2</sup>/T] is the hydrodynamic dispersion coefficient along the fracture,  $D'$  [L<sup>2</sup>/T] is the diffusion coefficient in the porous matrix,  $R$  [-] is the retardation coefficient due to sorption on the fracture walls,  $\theta$  [-] is the matrix porosity, and  $t$  [T] is the time.

In the fracture network, the solute mass sharing at intersections is calculated using the complete mixing (CM) method developed by Berkowitz, Naumann, and Smith (1994). In general, the effect of the choice of mixing rule on overall transport behaviour in the random networks considered here is rather minimal (Park et al., 2001). The CM method assumes that the BTC at the intersection is sufficient to allow spatial homogenization through molecular diffusion, and therefore solute concentrations in the downstream fractures are proportional to their discharges (**Fig. 2a**). Mass conservation at any fracture intersection, based on the CM method, is calculated by:

$$\sum_{i=1}^N c_i Q_i = \sum_{j=1}^M c_j Q_j \quad (5-3)$$

where the subscripts  $i$  and  $j$  represent the upstream and downstream fractures, respectively, and  $N$  and  $M$  represent the number of upstream and downstream fractures, respectively. The percent of the solute mass entering each downstream fracture is determined as follows:

$$P_k = \frac{Q_k}{\sum_{j=1}^M Q_j} \quad (5-4)$$

where  $P_k$  is the percent of solute mass from the upstream intersection entering a downstream fracture  $k$ .

### 5.3.3 Upscaling the Fracture Network Model

Based on the above rationale, the first stage of the UFN model development is focused on dividing the micro-scale network ( $\sim 200 \text{ m} \times 200 \text{ m}$ ) into equal elementary volumes (EV-FNs) ( $\sim 50 \text{ m} \times 50 \text{ m}$ ) such that the fracture density in one EV-FN is sufficient to represent the network properties.

**Fig. 5-3** shows the micro-scale network divided into equal EV-FNs such that the number of EV-FNs in the micro-scale network is equal to the number of EV-FNs in the macro scale network ( $\sim 1 \text{ km} \times 1 \text{ km}$ ).

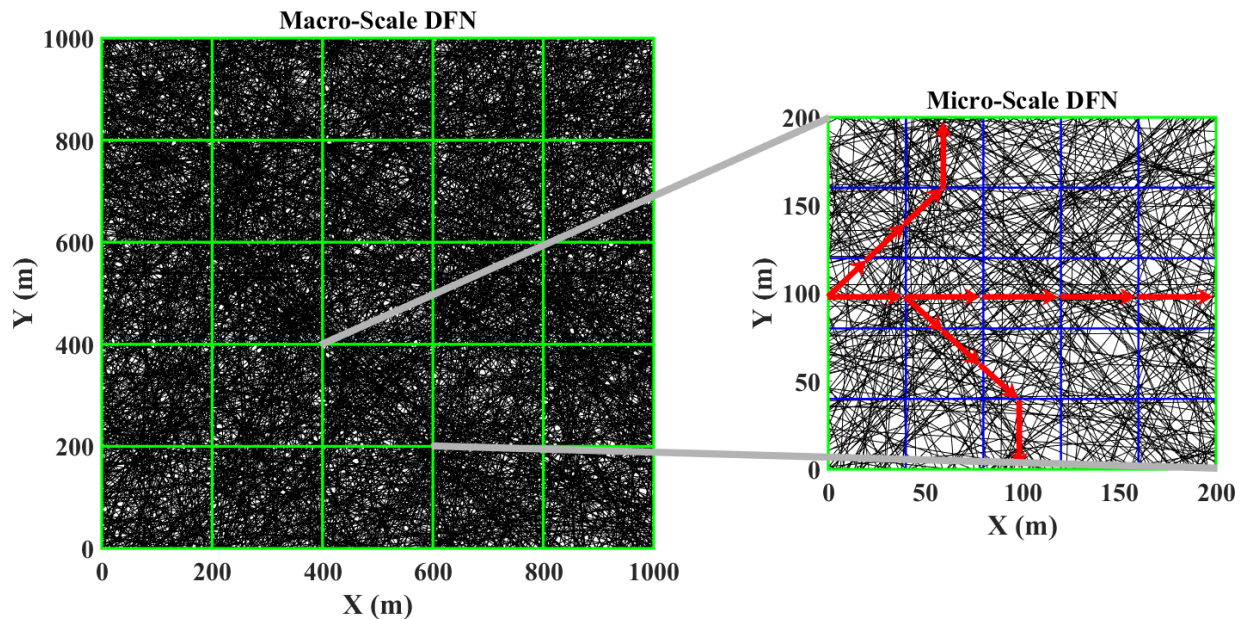


**Fig. 5-3: The macro- and micro-network scales showing the EV-FNs in the macro scale in green, the EV-FNs in the micro scale in blue, and the FCs in red.**

Subsequently, the solute transport migration is obtained at the micro-scale network using a RWPT-based model (see section 5.3.2) in a DFN (**Fig. 5-4**) by simulating the solute mass entering and leaving each EV-FN for a downscaled solute inlet boundary from the macro-scale to the micro-scale network. The calculated solute masses crossing the boundaries of each EV-FN are then used to generate representative FCs (**Fig. 5-4**) that represent the solute migration in the entire micro-scale network. Additionally, the mass ratios within each EV (microscale) were evaluated and assigned to the corresponding FC (macroscale). For illustration, **Fig. 5-4** shows an example of the micro-scale network discretized into equal EV-FNs with solute released on the left boundary between  $y = 80$  and  $120$  m.

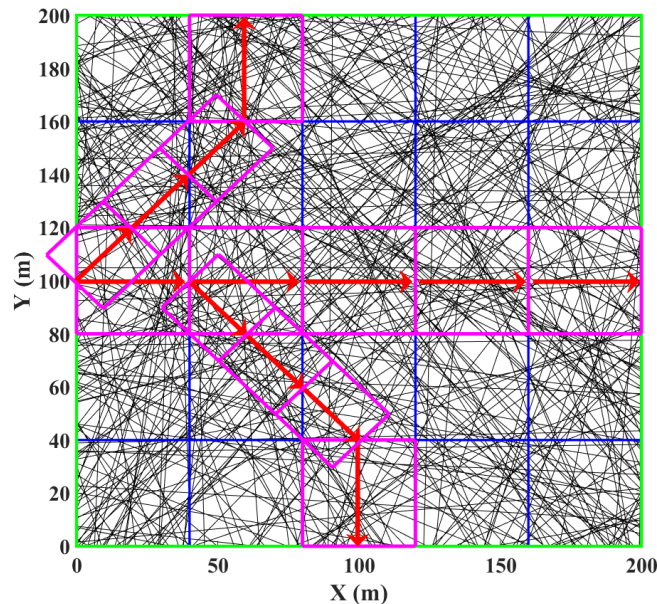


**Fig. 5-4: An example for the micro scale network showing the FCs in blue EV-FNs. The purple EV-FCs describe the solute retention in the flow channels.**

The second stage of the UFN model development upscales the FCs to the macro-scale network—essentially replacing each micro-scale network by a series of corresponding FCs. At this point, RWPT is then applied to the individual FC within the macroscale (recall that each FC represents a complete microscale network) to calculate the mass transfer probability. **Fig. 5-5** shows the EV-FCs corresponding to all five possible FC directions are obtained from the macro-scale network. Each FC in the FC-based network is either the length of the EV-FN (**Fig. 5-5a,b,c**) or the length that connects the boundary midpoint to the adjacent boundary midpoint ( $\text{boundary length} \times \frac{\sqrt{2}}{2}$ ) (**Fig. 5-5d,e**). For example, **Fig. 5-5a** shows solute migrating from left to right through the FC. The corresponding mass transfer probability is calculated at the effluent (right) boundary of the FC (which coincides with the right boundary of the EV-FN). The evaluated mass transfer probabilities are then retained in a look-up table. Note that five possible FCs are considered when the flow direction is from left to right; however, three more FCs are possible if flow from right to left is considered but this flow direction is beyond the scope of this work.

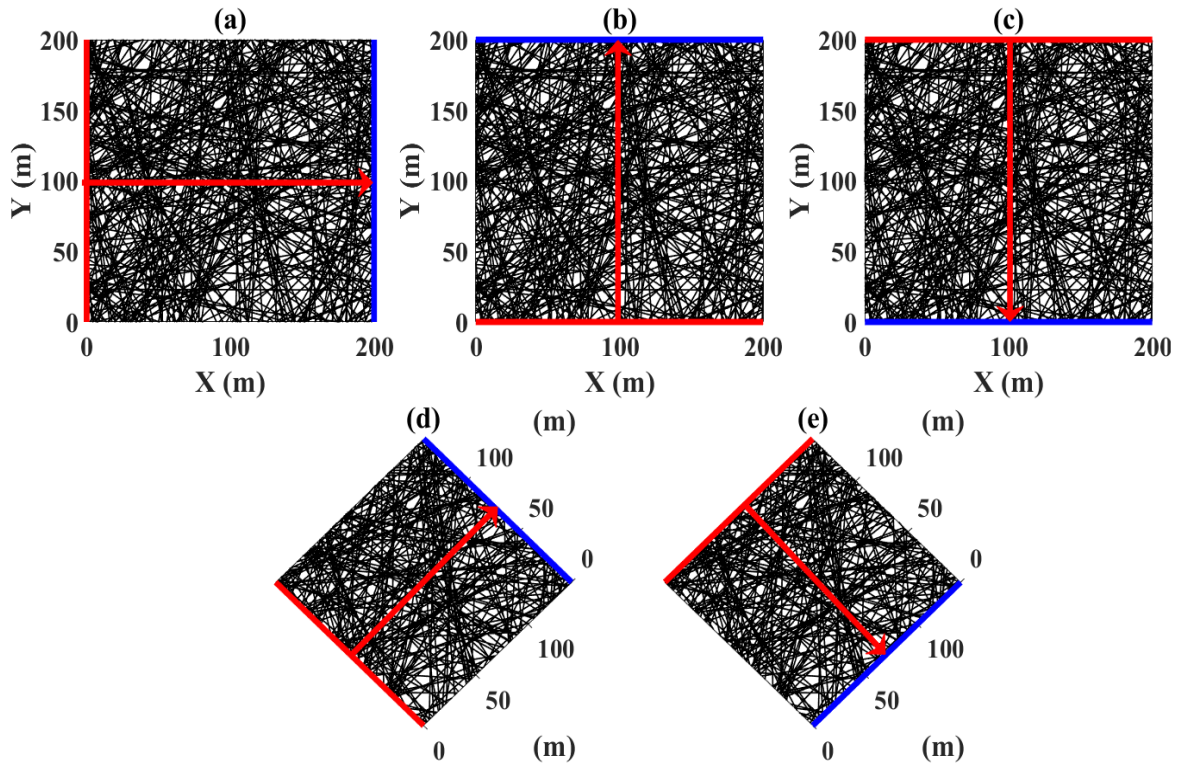


**Fig. 5-5: The EV-FCs with corresponding BTCs (in the micro-scale network) for all five possible FCs in case the flow direction is from left to right (i.e., solute transport directions). Solute is released along the influent (red) boundary, and the BTC is calculated at the effluent (blue) boundary.**

The third and final stage of the model development involves obtaining the solute transport solution in the macro scale. To calculate the breakthrough curve (BTC) in the inlet FC outlets, the injected solute mass ratio of the inlet FC is multiplied by the mass transfer probability of reaching the FC outlet. Then, the resulting breakthrough curve (BTC) at the FC intersection is multiplied by the solute mass ratio of the downstream FC to evaluate the proportional BTC influent to such FC.

Then, the mass transfer approach is numerically applied between the proportional BTC at each FC intersection and the mass transfer probability of reaching the FC outlet to calculate the macro-scale BTC at each downstream FC intersection to calculate the final effluent BTC in the downstream FCs:

$$C_{final}(t) = (C_1 * C_2)(t) = \int_0^t C_1(\tau) \cdot C_2(t - \tau) d\tau \quad (5-5)$$

where  $C_1$  [M/L<sup>3</sup>] is the solute concentration at the inlet of the FC at time  $\tau$ ,  $C_2$  [-] is the mass transfer probability of reaching the FC outlet shifted by  $t$ , and  $C_{final}(t)$  [M/L<sup>3</sup>] is the final effluent BTC for the FC. Finally, during applying the mass transfer approach, the effluent BTCs for the upstream FCs in each intersection in the FCs-based network are coupled to calculate the Final BTC at each intersection.

## 5.1. Results and Discussion

This section starts by presenting the solute masses in the EV-FNs calculated by the RWPT model. The comparison between the UFN model and the RWPT model are then plotted to validate the UFN model in the micro-scale network, and the impact of the EV-FN size was investigated. Finally, mass distribution is calculated using the UFN model in the macro scale network.

### 5.4.1 Model Validation

The BTCs from the RWPT-based model (Khafagy et al., 2020) (i.e., used to establish the simplified FC-based network) were compared to the BTCs obtained from the UFC model (i.e., using the FC-based network approach) to verify the validity of the UFN model approach. The fracture network

properties used in the UFN and RWPT model simulations for validation purposes are shown in **Table 5-1**. In these simulations, the solute was injected (i.e., 5,000 particles) along the entire west boundary using a pulse boundary condition, and the resulting BTCs from each EV-FC were converted to represent a constant concentration at the inlet boundary using the method described by Khafagy et al., (2022a). **Fig. 5-6** shows the FC-based network obtained from the RWPT simulation and the corresponding solute mass fractions for  $\alpha = 1$  m (**Fig. 5-6a**) and  $\alpha = 5$  m (**Fig. 5-6b**).

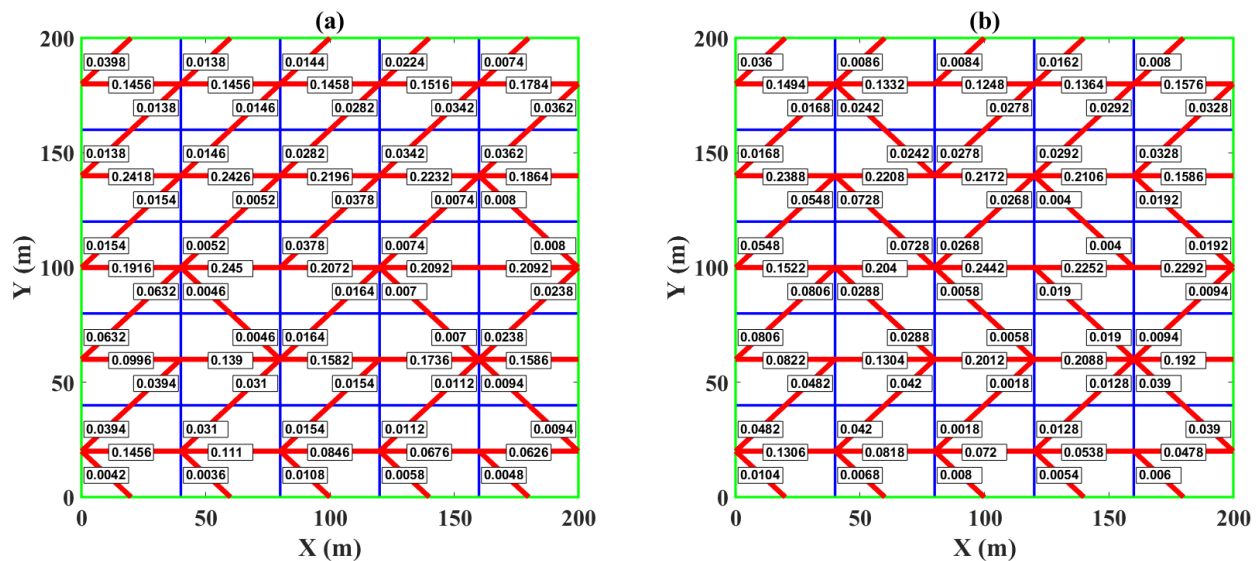


**Fig. 5-6: FC-based networks and solute masses corresponding to the micro scale network (Fig. 5-3b) for (a)  $\alpha = 1$  m and (b)  $\alpha = 5$  m.**

The effluent BTCs calculated by the UFN model validation simulations (i.e., model parameters in **Table 5-1**) (converted to simulate a Type 1 boundary condition) are plotted against those obtained

from the RWPT-based model in **Fig. 5-7** for the micro scale network shown in **Fig. 5-3b**. The results show good agreement between the UFN and RWPT results at all three effluent boundaries (i.e., north, east, and south) for both dispersivity values (i.e.,  $\alpha = 1$  m and  $\alpha = 5$  m). At the East boundary,  $r^2$  is 0.9923 for  $\alpha = 1$  m, whereas  $r^2$  is 0.9998 for  $\alpha = 5$  m. The BTC at the east boundary results in slightly longer retention time, with the solute mass reaching the east boundary approximately 6% later. The UFN model shows that sequential correlation of the BTCs along the generated FCs accurately reproduces the results of DFN simulations and provides a practical and easily implementable alternative to continuum transport models.

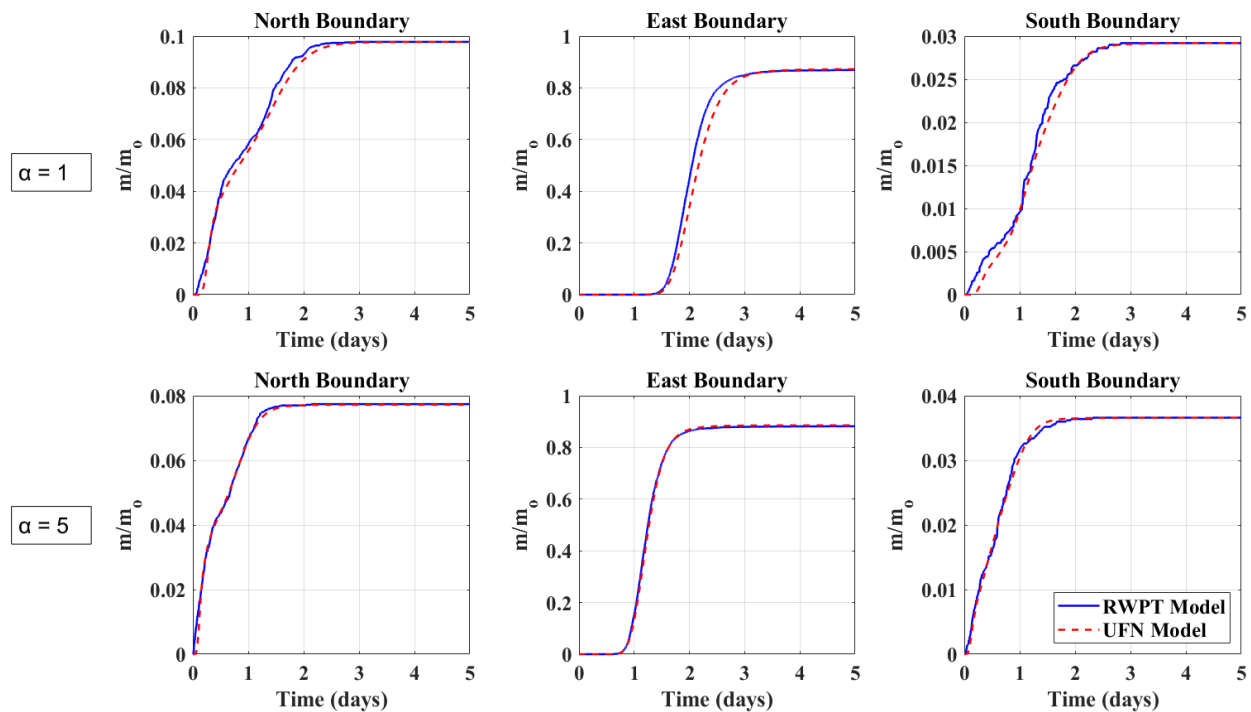


**Fig. 5-7: BTCs from model validation runs (i.e., network properties in Table 5-1 in the micro-scale network (Fig. 5-3b) with a Type 1 boundary condition for  $\alpha = 1$  m and  $\alpha = 5$  m. Solid blue lines represent the RWPT model and dashed red lines represent the UFN model.**

### 5.4.2 Impact of EV-FN Size

The impact of the EV-FN size was investigated by comparing the effluent BTCs simulated by the UFN model for the network properties in **Table 5-1** in the micro-scale network against those obtained from the RWPT model with 5,000 particles released. **Fig. 5-8** shows the RMSE of BTCs for each EV-FN size at effluent boundaries (east, north, and south boundaries) for  $\alpha = 1$  m. The results show that the RMSE for the east boundary is significantly larger than those of the north and south boundaries; this is because most of the solute mass reached the east boundary (~ 88%). In general, the RMSE increases as the EV-FN length decreases. For the network properties used in these simulations, and if a RMSE threshold of 0.05 is applied, then the EV-FN fails to represent the macro-scale network properties when its length is less than 33 m. Note that the EV-FN can be estimated prior to using the identified FC-based network at the macro or network scales by pre-calculating the RMSE for the micro-scale network.

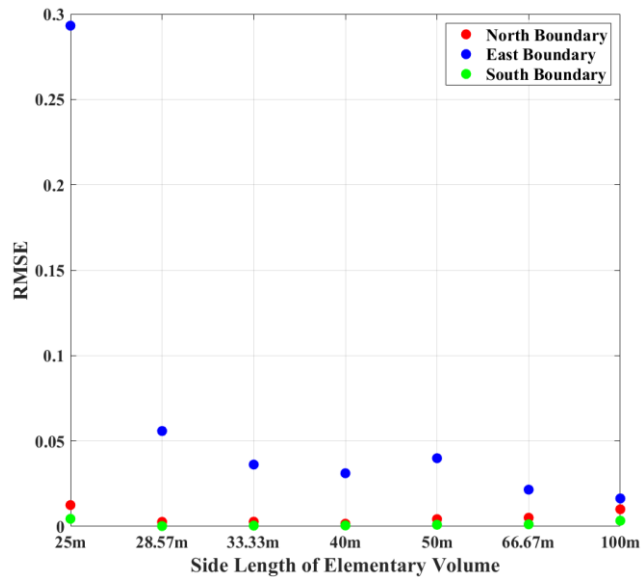


**Fig. 5-8: RMSE versus EV-FN size for the BTCs at effluent boundaries of the UFN model for  $\alpha = 1$  m.**

### 5.4.3 Mass Distribution using the UFN model

The UFN model can calculate the spatial and temporal distribution of mass in each EV-FN boundary in the macro scale network. The BTCs calculated by the UFN model at the north, east, and south effluent boundaries are shown in **Fig. 5-9** for the network properties in **Table 5-1** (converted to simulate a Type 1 boundary condition). Most of the solute mass reached the east boundary (~ 88%) due to the horizontal hydraulic gradient in the fracture network, whereas the remainder of the solute mass reached the north and south boundaries due to the hydrodynamic dispersion within the network. Increasing the dispersivity from 1 to 5 resulted in more mass spreading at the east boundary, a decrease in the fraction of mass exiting at the north boundary, and an increase in the fraction of mass exiting at the south boundary.

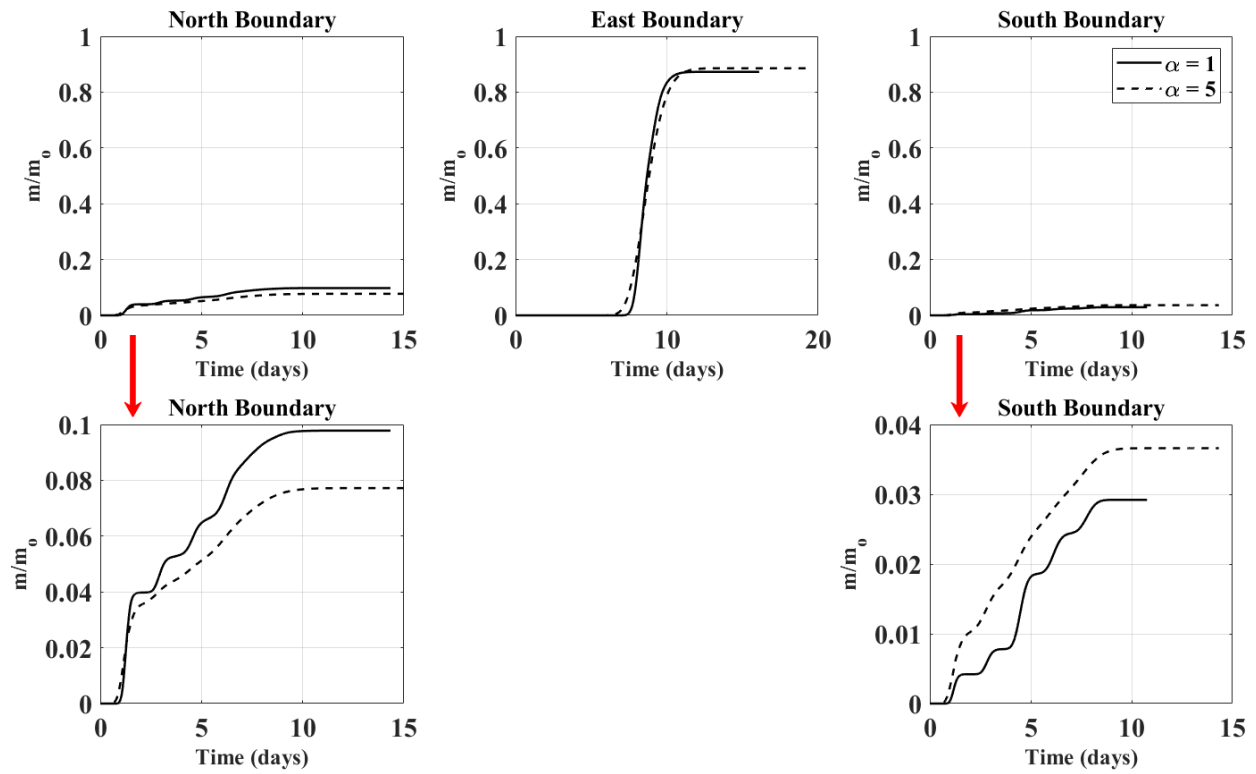


**Fig. 5-9: BTCs calculated for network properties in Table 2-1 calculated by the UFN model at effluent boundaries in the macro scale network (Fig. 2-3) for Type 1 boundary condition. Lines and dashed lines represent simulations for  $\alpha = 1$  m and  $\alpha = 5$  m, respectively.**

Note that if the direction of the macroscopic gradient varies significantly over the larger region of interest, similar subdivision may also be needed. This would, of course, require a separate set of DFN simulations to obtain the transport solution using the UFN model in each modeled subregion. The UFN model arrived at a solution in approximately 15% of the time required for the macro scale network (Fig. 5-2) to arrive at solutions using the RWPT approach only if the same number of released particles (5,000 particles in this study) in micro- scale fracture network (i.e., the small

FN (**Fig. 5-3b**)). The RWPT model requires at least five times more released particles to obtain accurate BTCs. Furthermore, the RWPT model requires higher computational resources than typical PC to obtain the transport solution in the macro scale network due to the large number of fractures in the network. This emphasizes the computational efficiency of the developed UFN model, which will become more pronounced as the scale and complexity of the fracture network increases and more solute particles are required for accurate results using the RWPT approach.

Another new aspect of this work is that the UFN model is extremely simple to implement, and the simulation executes very quickly. The UFN model does not yield the same level of insight that can be obtained through analytical methods, and we regard the approach as a practical tool that can be used to estimate transport at a given site.

## **5.2. Conclusion**

In conclusion, direct upscaling of DFN simulations provides an alternative to site-scale continuum transport models. The suggested procedure is to first perform small scale DFN simulations utilizing hydraulic, geologic, and chemical information on the fracture network, and then use the results collected from these DFN simulations to obtain transport results at larger scales. This approach avoids volume averaging and other assumptions inherent in the continuum approach, and preserves solute migration observed in DFN simulations. It also allows relevant transport and retention processes to be incorporated directly (e.g., advection and dispersion, matrix diffusion, sorption onto the fracture walls and in the matrix, and radioactive decay). The results presented here demonstrate that advection and dispersion can be included in the model at the macro scale

with relatively modest computational effort. The UNM model performed well when compared with simulations from the RWPT-based numerical model in the small FN. The UNM model is computationally efficient, arriving at a solution in approximately 25% of the time required for the RWPT model with 5,000 particles released. The impact of this efficiency will become more apparent when more particles are released, and in larger, more complex networks.

A key finding of this study is that the size of EV-FNs, which are used to estimate the FC-based network, impact the accuracy of the BTCs. The EV-FNs must be larger than the representative EV to preserve the network properties. Two straightforward modifications of the upscaling approach may be needed for applications. The method assumes that the DFN is homogeneous such that the FC-based network is representative of the larger region of interest. This would not be true if the statistical properties of the networks vary significantly over the larger region of interest. Such non-stationarity is not uncommon and can be addressed in applications by simply dividing the larger region of interest into subregions with approximately constant network properties in each. For anisotropic networks, the transport solution may also depend on the direction of macroscopic gradient relative to the principal directions of the network. If the direction of the macroscopic gradient varies significantly over the larger region of interest, similar subdivision may also be needed. This would, of course, require a separate set of DFN simulations to obtain the transport solution in each modeled subregion.

### **5.3. Acknowledgment**

The financial support for the study was provided through the CaNRisk-CREATE program of the Natural Science and Engineering Research Council (NSERC) of Canada (Grant Number: CREAT-482707-2016).

## 5.4. References

- Ahmed, M.I., Abd-Elmegeed, M.A., Hassan, A.E., 2019. Modelling transport in fractured media using the fracture continuum approach. *Arab. J. Geosci.* 12. <https://doi.org/10.1007/s12517-019-4314-3>
- Bechtold, M., Vanderborght, J., Ippisch, O., Vereecken, H., 2011. Efficient random walk particle tracking algorithm for advective-dispersive transport in media with discontinuous dispersion coefficients and water contents. *Water Resour. Res.* 47, 1–20. <https://doi.org/10.1029/2010WR010267>
- Benke, R., Painter, S., 2003. Modeling conservative tracer transport in fracture networks with a hybrid approach based on the Boltzmann transport equation. *Water Resour. Res.* 39, 1–11. <https://doi.org/10.1029/2003WR001966>
- Berkowitz, B., Naumann, C., Smith, L., 1994. Mass transfer at fracture intersections: An evaluation of mixing model. *Water Resour. Res.* 30, 1765–1773.
- Berre, I., Doster, F., Keilegavlen, E., 2019. Flow in Fractured Porous Media: A Review of Conceptual Models and Discretization Approaches. *Transp. Porous Media* 130, 215–236. <https://doi.org/10.1007/s11242-018-1171-6>
- Bishop, P., Persaud, E., Levison, J., Parker, B., Novakowski, K., 2020. Inferring flow pathways between bedrock boreholes using the hydraulic response to borehole liner installation. *J. Hydrol.* 580, 124267. <https://doi.org/10.1016/j.jhydrol.2019.124267>
- Chen, Y., Wang, H., Wang, Y., Ma, G., 2020. Numerical evaluation of a fracture acidizing

treatment in a three-dimensional fractured carbonate reservoir. *J. Nat. Gas Sci. Eng.* 81, 103440. <https://doi.org/10.1016/j.jngse.2020.103440>

Cuss, R.J., Harrington, J.F., Noy, D.J., Sathar, S., Norris, S., 2015. An experimental study of the flow of gas along synthetic faults of varying orientation to the stress field: Implications for performance assessment of radioactive waste disposal. *J. Geophys. Res. Solid Earth* 120, 3932–3945. <https://doi.org/10.1002/2014JB011333>

Day-Lewis, F.D., Slater, L.D., Robinson, J., Johnson, C.D., Terry, N., Werkema, D., 2017. An overview of geophysical technologies appropriate for characterization and monitoring at fractured-rock sites. *J. Environ. Manage.* 204, 709–720. <https://doi.org/10.1016/j.jenvman.2017.04.033>

Dippenaar, M.A., van Rooy, J.L., Diamond, R.E., 2019. Engineering, hydrogeological and vadose zone hydrological aspects of Proterozoic dolomites (South Africa). *J. African Earth Sci.* 150, 511–521. <https://doi.org/10.1016/j.jafrearsci.2018.07.024>

Dong, R., Lee, S., Wheeler, M., 2019. Numerical simulation of matrix acidizing in fractured carbonate reservoirs using adaptive enriched Galerkin method. *Soc. Pet. Eng. - SPE Reserv. Simul. Conf. 2019, RSC 2019* 1–19. <https://doi.org/10.2118/193862-ms>

Feng, S., Wang, Hanqing, Cui, Y., Ye, Y., Liu, Y., Li, X., Wang, Hong, Yang, R., 2020. Fractal discrete fracture network model for the analysis of radon migration in fractured media. *Comput. Geotech.* 128, 103810. <https://doi.org/10.1016/j.compgeo.2020.103810>

Flemisch, B., Berre, I., Boon, W., Fumagalli, A., Schwenck, N., Scotti, A., Stefansson, I., Tatomir,

- A., 2018. Benchmarks for single-phase flow in fractured porous media. *Adv. Water Resour.* 111, 239–258. <https://doi.org/10.1016/j.advwatres.2017.10.036>
- Follin, S., Hartley, L., Rhén, I., Jackson, P., Joyce, S., Roberts, D., Swift, B., 2014. Une méthodologie pour établir les paramètres du modèle hydrogéologique d'un réseau de fractures discrètes dans une roche cristalline peu fracturée, illustrée d'après les données du site de stockage de déchets nucléaires haute activité projeté à Forsmark, . *Hydrogeol. J.* 22, 313–331. <https://doi.org/10.1007/s10040-013-1080-2>
- Frampton, A., Hyman, J.D., Zou, L., 2019. Advective Transport in Discrete Fracture Networks With Connected and Disconnected Textures Representing Internal Aperture Variability. *Water Resour. Res.* 55, 5487–5501. <https://doi.org/10.1029/2018WR024322>
- Hyman, J.D., Rajaram, H., Srinivasan, S., Makedonska, N., Karra, S., Viswanathan, H., Srinivasan, G., 2019. Matrix Diffusion in Fractured Media: New Insights Into Power Law Scaling of Breakthrough Curves. *Geophys. Res. Lett.* 46, 13785–13795. <https://doi.org/10.1029/2019GL085454>
- Iraola, A., Trinchero, P., Karra, S., Molinero, J., 2019. Assessing dual continuum method for multicomponent reactive transport. *Comput. Geosci.* 130, 11–19. <https://doi.org/10.1016/j.cageo.2019.05.007>
- Jiang, L., Liu, J., Liu, T., Yang, D., 2021. Semi-analytical modeling of transient pressure behaviour for fractured horizontal wells in a tight formation with fractal-like discrete fracture network. *J. Pet. Sci. Eng.* 197, 107937. <https://doi.org/10.1016/j.petrol.2020.107937>

- Khafagy, M., El-Dakhakhni, W., Dickson-Anderson, S., 2022. Analytical model for solute transport in discrete fracture networks: 2D spatiotemporal solution with matrix diffusion. *Comput. Geosci.* 159, 104983. <https://doi.org/10.1016/j.cageo.2021.104983>
- Khafagy, M.M., Abd-Elmegeed, M.A., Hassan, A.E., 2020. Simulation of reactive transport in fractured geologic media using random-walk particle tracking method. *Arab. J. Geosci.* 13. <https://doi.org/10.1007/s12517-019-4952-5>
- Khoei, A.R., Salehi Sichani, A., Hosseini, N., 2020. Modeling of reactive acid transport in fractured porous media with the Extended-FEM based on Darcy-Brinkman-Forchheimer framework. *Comput. Geotech.* 128, 103778. <https://doi.org/10.1016/j.compgeo.2020.103778>
- Ma, G., Chen, Y., Jin, Y., Wang, H., 2018. Modelling temperature-influenced acidizing process in fractured carbonate rocks. *Int. J. Rock Mech. Min. Sci.* 105, 73–84. <https://doi.org/10.1016/j.ijrmms.2018.03.019>
- Maillot, J., Davy, P., Le Goc, R., Darcel, C., de Dreuzy, J.R., 2016. Connectivity, permeability, and channeling in randomly distributed and kinematically defined discrete fracture network models. *Water Resour. Res.* 52, 8526–8545. <https://doi.org/10.1002/2016WR018973>
- Painter, S., Cvetkovic, V., Selroos, J.O., 2002. Power-law velocity distributions in fracture networks: Numerical evidence and implications for tracer transport. *Geophys. Res. Lett.* 29, 14–17. <https://doi.org/10.1029/2002GL014960>
- Park, Y.J., De Dreuzy, J.R., Lee, K.K., Berkowitz, B., 2001. Transport and intersection mixing in

random fracture networks with power law length distributions. *Water Resour. Res.* 37, 2493–2501. <https://doi.org/10.1029/2000WR000131>

Sandve, T.H., Berre, I., Nordbotten, J.M., 2012. An efficient multi-point flux approximation method for Discrete Fracture-Matrix simulations. *J. Comput. Phys.* 231, 3784–3800. <https://doi.org/10.1016/j.jcp.2012.01.023>

Snow, D.T., 1965. A Parallel Plate Model of Fractured Permeable Media 344.

Sweeney, M.R., Gable, C.W., Karra, S., Stauffer, P.H., Pawar, R.J., Hyman, J.D., 2020. Upscaled discrete fracture matrix model (UDFM): an octree-refined continuum representation of fractured porous media. *Comput. Geosci.* 24, 293–310. <https://doi.org/10.1007/s10596-019-09921-9>

Trincherro, P., Iraola, A., 2020. Models for the assessment of transport of naturally-occurring nuclides in fractured media. *J. Hydrol.* 580, 124322. <https://doi.org/10.1016/j.jhydrol.2019.124322>

Viswanathan, H.S., Hyman, J.D., Karra, S., O'Malley, D., Srinivasan, S., Hagberg, A., Srinivasan, G., 2018. Advancing Graph-Based Algorithms for Predicting Flow and Transport in Fractured Rock. *Water Resour. Res.* 54, 6085–6099. <https://doi.org/10.1029/2017WR022368>

Wang, L., Mou, J., Mo, S., Zhao, B., Liu, Z., Tian, X., 2020. Modeling matrix acidizing in naturally fractured carbonate reservoirs. *J. Pet. Sci. Eng.* 186, 106685. <https://doi.org/10.1016/j.petrol.2019.106685>

- Wang, M., Zhao, W. dong, Garrard, R., Zhang, Y., Liu, Y., Qian, J. zhong, 2018. Revisit of advection-dispersion equation model with velocity-dependent dispersion in capturing tracer dynamics in single empty fractures. *J. Hydrodyn.* 30, 1055–1063. <https://doi.org/10.1007/s42241-018-0134-2>
- Wang, X., Jardani, A., Jourde, H., Lonergan, L., Cosgrove, J., Gosselin, O., Massonnat, G., 2016. Characterisation of the transmissivity field of a fractured and karstic aquifer, Southern France. *Adv. Water Resour.* 87, 106–121. <https://doi.org/10.1016/j.advwatres.2015.10.014>
- Wang, Z., Bi, L., Kwon, S., Qiao, L., Li, W., 2020. The effects of hydro-mechanical coupling in fractured rock mass on groundwater inflow into underground openings. *Tunn. Undergr. Sp. Technol.* 103, 103489. <https://doi.org/10.1016/j.tust.2020.103489>
- Wu, Y., Kou, J., Sun, S., 2022. Matrix acidization in fractured porous media with the continuum fracture model and thermal Darcy-Brinkman-Forchheimer framework. *J. Pet. Sci. Eng.* 211, 110210. <https://doi.org/10.1016/j.petrol.2022.110210>
- Yao, W., Mostafa, S., Yang, Z., Xu, G., 2020. Role of natural fractures characteristics on the performance of hydraulic fracturing for deep energy extraction using discrete fracture network (DFN). *Eng. Fract. Mech.* 230, 106962. <https://doi.org/10.1016/j.engfracmech.2020.106962>
- Zhang, C., Chen, Q., Qin, X., Hong, B., Meng, W., Zhang, Q., 2017. In-situ stress and fracture characterization of a candidate repository for spent nuclear fuel in Gansu, northwestern China. *Eng. Geol.* 231, 218–229. <https://doi.org/10.1016/j.enggeo.2017.10.007>

Zhang, Q., Deng, H., Dong, Y., Molins, S., Li, X., Steefel, C., 2022. Investigation of Coupled Processes in Fractures and the Bordering Matrix via a Micro-Continuum Reactive Transport Model. *Water Resour. Res.* 58, 1–18. <https://doi.org/10.1029/2021WR030578>

## Chapter 6: Summary and Conclusions

The main goal of this dissertation is to develop efficient numerical models that describe solute transport in complex, field-scale fractured aquifers. Four research objectives have been designed to achieve this goal: (1) develop a computationally efficient analytical model for simulating two-dimensional spatial and temporal solute transport in discrete fracture networks (DFNs), (2) develop a closed-form solution describing the classical advection-dispersion equation for simulating reactive transport in single, parallel-plate fractures under a range of conditions, (3) develop a numerical model (based on the closed-form solution developed in Objective 2) to simulate solute transport in small-scale ( $\sim 350 \text{ m} \times 350 \text{ m}$ ) discrete fracture networks considering mass exchange between the fracture and surrounding matrix, and (4) upscale the frameworks developed in Objectives 1 and 3 to develop an accurate and computationally efficient numerical model simulating solute transport in field-scale fracture networks .

The first Objective is presented in Chapter 2. An analytical network (AN) model is developed to simulate solute transport in two-dimensional fracture networks considering advection and dispersion within the fracture, sorption on the fracture walls and within the matrix, matrix diffusion, and first-order decay. the complete mixing (CM) and stream-tube (ST) methods are used for mass sharing at intersections, and the performance of these methods was compared under a range of Peclet numbers ( $P_e$ ). The transfer function approach was applied to calculate solute transport in each fracture using the output from the mass sharing scheme as the upstream boundary condition. Based on the work presented in chapter 2, it can be concluded that:

- It was also found that when  $P_e$  is small, the mass sharing method impacts the shape of the BTC

regardless of the presence of matrix diffusion, with the CM method producing higher dispersion than the ST method.

- The differences between the CM and ST BTCs are less pronounced under high values of  $P_e$  in the absence of matrix diffusion.
- When matrix diffusion is considered at high  $P_e$ , the increased dispersion caused by the CM approach is only observable at early times, as the effect is dampened by matrix diffusion.
- The developed AN model arrived at a solution in FN1 network in less than 1% and 3% of the time required for the TDRW (without matrix diffusion) and RWPT (with matrix diffusion) approaches.

The second Objective is presented in Chapter 3. A closed-form solution (MGGP SF-ST model) is developed employing MGGP to simulate reactive transport in a single, parallel plate fracture under a range of hydraulic, geological and chemical conditions for either a constant concentration or pulse injection at the inlet. The model was developed based on a large dataset of BTCs (101,740 datapoints) generated from a published analytical solution for solute transport in a single fracture under a range of conditions (i.e., velocity, dispersion along the fracture, molecular diffusion within the fracture and into the matrix, and adsorption within the matrix). Based on the work presented in chapter 3, it can be concluded that:

- The MGGP SF-ST model represents an important contribution as it is relatively easy to implement and provides a computationally efficient tool relative to existing analytical solutions and numerical models.
- The MGGP SF-ST model advances solute transport behavior predictions especially when the

scale of simulation increases from that of a single fracture to a network.

The third Objective is presented in Chapter 4. A numerical model is developed to simulate the solute transport in fracture networks based on an extension of the MGGP SF-ST model for solute transport in a single fracture considering advection and dispersion along the fracture; molecular diffusion within the fracture and into the matrix; and, adsorption within the matrix for Type 1 and Type 2 BC. The extension is achieved by applying the CM method for solute mass sharing at fracture intersections to form a solute injected BTC for each fracture inlet as an inlet BC in this fracture. Based on the work presented in chapter 4, it can be concluded that:

- The developed model can approximately predict the solute transport as the CFD model when assuming a higher value of dispersivity which is highly affected by the fracture density in the fracture network.
- The numerical results of the DFN2 indicated that the low diffusion coefficient causes a long tail BTC at the outflow boundary of the network with smaller retention time of most of the solute, while small fracture aperture and large effective fracture spacings hinder the solute migration within the fracture network.
- The developed model will facilitate rapid simulations of solute transport in complex DFNs, while other models are computationally intensive to simulate the solute transport in such networks.

The fourth Objective is presented in Chapter 5. An upscaled fracture network (UFN) model is developed employing RWPT approach in a DFN. The UFN model accurately captures solute transport processes occurring at the macro scale fracture networks. The model involved

discretizing a complex fracture network into elementary volumes, within which both representative solute transport flow channels and their corresponding breakthrough curves were identified. Based on the work presented in chapter 5, it can be concluded that:

- The size of elementary volumes, which are used to estimate the flow channel-based network, are an important control on the breakthrough curves. The elementary volumes must be larger than the representative elementary volume to preserve the network properties.
- The UFN model assumes that the DFN is homogeneous such that the flow channel-based network is representative of the larger region of interest.
- The fluctuating statistical properties of the networks over the larger region of interest require a separate set of DFN simulations to obtain the transport solution in each modeled subregion.

## Appendix 1

Bear (1972) proposed an analytical solution to **Eq. (2-1)** neglecting the matrix (i.e., the fifth term in **Eq. (2-1)**). Their solution gives the concentration at the outlet boundary under a pulse injection at the fracture inlet and considers advection and hydrodynamic dispersion within the fracture, sorption on the fracture walls, and first-order decay:

$$C = \frac{m_o z}{2b W v \sqrt{4\pi \frac{D}{R} t^3}} \exp\left(-\frac{\left(z - \frac{v}{R} t\right)^2}{4 \frac{D}{R} t}\right) \exp(-\lambda t) \quad (\text{A.1.1})$$

where  $m_o$  [M] is the mass injected,  $W$  [L] is the fracture width, and  $R$  is the retardation coefficient due to sorption on the fracture walls represented by the linear adsorption isotherm (Freeze and Cherry, 1980):

$$R = 1 + \frac{K_f}{b} \quad (\text{A.1.2})$$

where  $K_f$  [L] is the fracture distribution coefficient.

Sudicky and Frind (1982) proposed an analytical solution to **Eq. (2-1)** for a constant concentration boundary at the inlet considering matrix diffusion (i.e., the fifth term in **Eq. (2-1)**), advection and hydrodynamic dispersion in the fracture, molecular diffusion into the matrix, adsorption onto the walls and within the matrix, and first-order decay:

$$\frac{C}{C_0} = \frac{2}{\pi^2} \exp(vz) \int_l^\infty \exp \left[ -\xi^2 - \frac{v^2 z^2}{4\xi^2} - \frac{R\lambda z^2}{4D\xi^2} \right] \cdot \int_0^\infty \frac{\varepsilon}{\lambda^2 + \frac{\varepsilon^4}{4}} \exp(\varepsilon_R) \cdot \left\{ \exp(-\lambda T) \left[ \frac{\varepsilon^2}{2} \sin(\varepsilon_l)|_T - \lambda \cos(\varepsilon_l)|_T \right] + \frac{\varepsilon^2}{2} \sin(\Omega) + \lambda \cos(\Omega) \right\} d\varepsilon d\xi \quad (\text{A.1.3})$$

where

$$Y = \frac{v^2 K^2 z^2}{4A \xi^2} \quad K^2 = \frac{4RD}{V^2}$$

$$\Omega = \frac{Y\varepsilon}{2} \left( \frac{\sinh(\sigma\varepsilon) + \sin(\sigma\varepsilon)}{\cosh(\sigma\varepsilon) + \cos(\sigma\varepsilon)} \right) \quad \Omega' = \Omega + \frac{Rz^2 \varepsilon^2}{8\xi^2}$$

$$\sigma = G(B - b) \quad G = \sqrt{\frac{R'}{D'}}$$

$$A = \frac{bR}{\theta \sqrt{R'D'}} \quad D = \alpha_L V + D^*$$

$$D' = \tau D^* \quad v = \frac{V}{2D}$$

$$\varepsilon_l = \frac{\varepsilon^2 t}{2} - \frac{Y\varepsilon}{2} \left( \frac{\sinh(\sigma\varepsilon) + \sin(\sigma\varepsilon)}{\cosh(\sigma\varepsilon) + \cos(\sigma\varepsilon)} \right) \quad \varepsilon_R = \frac{Y\varepsilon}{2} \left( \frac{\sinh(\sigma\varepsilon) - \sin(\sigma\varepsilon)}{\cosh(\sigma\varepsilon) + \cos(\sigma\varepsilon)} \right)$$

$$T = t - \frac{Rz^2}{4D\xi^2} \quad T \geq 0$$

and where  $C_0$  [M/L<sup>3</sup>] is the source concentration,  $2B$  [L] is the spacing between the centerlines of

the fractures,  $R'$  [-] is the retardation coefficient in the matrix,  $D^*$  [ $L^2/T$ ] is the molecular diffusion coefficient for the solute in water,  $\alpha_L$  [L] is the dispersivity,  $\tau$  [-] is the matrix tortuosity, and  $R'$  is the matrix retardation coefficient due to sorption and is represented by the linear adsorption isotherm (Freeze and Cherry, 1980):

$$R' = 1 + \frac{\rho_b}{\theta} K_m \quad (\text{A.1.4})$$

where  $\rho_b$  [ $M/L^3$ ] is the bulk density of the porous matrix, and  $K_m$  [ $L^3/M$ ] is the matrix distribution coefficient.

## References

Bear, J. (1972). *Dynamics of Fluids in Porous Media*. New York, Dover Publications, 1–783.

Freeze, R.A., Cherry, J.A., 1980. Groundwater, *Journal of Hydrology*.  
[https://doi.org/10.1016/0022-1694\(80\)90057-8](https://doi.org/10.1016/0022-1694(80)90057-8)

Sudicky, E.A., Frind, E.O., 1982. Contaminant transport in fractured porous media: Analytical solutions for a system of parallel fractures. *Water Resour. Res.* 18, 1634–1642.  
<https://doi.org/10.1029/WR018i006p01634>

## Appendix 2

Sudicky and Frind (1982) proposed an analytical solution for a constant concentration boundary at the inlet considering matrix diffusion, advection and hydrodynamic dispersion in the fracture, molecular diffusion into the matrix, adsorption onto the walls and within the matrix, and first-order decay:

$$\frac{c}{c_o} = \frac{2}{\pi^{\frac{3}{2}}} \exp(vz) \int_l^\infty \exp \left[ -\xi^2 - \frac{v^2 z^2}{4\xi^2} - \frac{R\lambda z^2}{4D\xi^2} \right] \cdot \int_0^\infty \frac{\varepsilon}{\lambda^2 + \frac{\varepsilon^4}{4}} \exp(\varepsilon_R) \cdot \left\{ \exp(-\lambda T) \left[ \frac{\varepsilon^2}{2} \sin(\varepsilon_l)|_T - \lambda \cos(\varepsilon_l)|_T \right] + \frac{\varepsilon^2}{2} \sin(\Omega) + \lambda \cos(\Omega) \right\} d\varepsilon d\xi \quad (\text{A.2.1})$$

where

$$Y = \frac{v^2 K^2 z^2}{4A \xi^2}$$

$$K^2 = \frac{4RD}{V^2}$$

$$\Omega = \frac{Y\varepsilon}{2} \left( \frac{\sinh(\sigma\varepsilon) + \sin(\sigma\varepsilon)}{\cosh(\sigma\varepsilon) + \cos(\sigma\varepsilon)} \right)$$

$$\Omega' = \Omega + \frac{Rz^2 \varepsilon^2}{8\xi^2}$$

$$\sigma = G(B - b)$$

$$G = \sqrt{\frac{R_m}{D_m}}$$

$$A = \frac{bR}{\theta \sqrt{R_m D_m}}$$

$$D = \alpha_L V + D^*$$

$$D_m = \tau D^* \qquad v = \frac{V}{2D}$$

$$\varepsilon_l = \frac{\varepsilon^2 t}{2} - \frac{Y\varepsilon}{2} \left( \frac{\sinh(\sigma\varepsilon) + \sin(\sigma\varepsilon)}{\cosh(\sigma\varepsilon) + \cos(\sigma\varepsilon)} \right) \qquad \varepsilon_R = \frac{Y\varepsilon}{2} \left( \frac{\sinh(\sigma\varepsilon) - \sin(\sigma\varepsilon)}{\cosh(\sigma\varepsilon) + \cos(\sigma\varepsilon)} \right)$$

$$T = t - \frac{Rz^2}{4D\xi^2} \quad T \geq 0 \qquad R = 1 + \frac{K_f}{b}$$

$$R_m = 1 + \frac{\rho_b}{\theta} K_m \qquad \lambda = \frac{\ln 2}{t_{1/2}}$$

where  $z$  [L] is the fracture length,  $t$  [T] is the time,  $C_o$  [M/L<sup>3</sup>] is the source concentration,  $V$  [L/T] is groundwater velocity in the fracture,  $b$  [L] is half of the aperture width,  $B$  [L] is half of the distance between centerline of two fractures,  $D^*$  [L<sup>2</sup>/T] is the molecular diffusion coefficient for the solute in water,  $D$  [L<sup>2</sup>/T] is the hydrodynamic dispersion coefficient along the fracture,  $D_m$  [L<sup>2</sup>/T] is the diffusion coefficient in the porous matrix,  $\alpha_L$  [L] is the dispersivity,  $\tau$  [-] is the matrix tortuosity,  $\theta$  [-] is the matrix porosity,  $\lambda$  [T<sup>-1</sup>] is the first-order decay constant,  $t_{1/2}$  [T] is the half-life of the solute,  $R$  [-] and  $R_m$  [-] are retardation coefficients in the fracture and matrix, respectively, based on linear adsorption isotherms as represented by Freeze and Cherry (1980),  $K_f$  [L] is the fracture distribution coefficient,  $\rho_b$  [M/L<sup>3</sup>] is the bulk density of the porous matrix, and  $K_m$  [L<sup>3</sup>/M] is the distribution coefficient of the porous matrix.

## References

Freeze, R.A., Cherry, J.A., 1980. Groundwater, Journal of Hydrology.  
[https://doi.org/10.1016/0022-1694\(80\)90057-8](https://doi.org/10.1016/0022-1694(80)90057-8)

Sudicky, E.A., Frind, E.O., 1982. Contaminant transport in fractured porous media: Analytical solutions for a system of parallel fractures. Water Resour. Res. 18, 1634–1642.  
<https://doi.org/10.1029/WR018i006p01634>

### Supplementary Data A (TDRW-Based Model)

The TDRW-based model used in this research is based on that developed by Bodin et al., (2003). The model simulates solute transport in fracture networks using a Lagrangian time domain random walk (TDRW) approach that combines the merits of both the random walk (RW) and particle tracking (PT) methods. Specifically, RW accounts for stochastic processes in the system, and PT calculates the length of time required for a particle to migrate from the upstream to downstream nodes (i.e., along a single fracture). Unlike PT which allows the particle to migrate a certain distance within a specified time step, RW allows a particle to migrate from the upstream to downstream nodes in a single step. At the network scale, a set of particles is injected at an inlet boundary and tracked through the network until they exit at the outlet boundary. The solution divides the fracture network into a set of parallel (elementary) pathways, and a portion of the particles released at the inlet boundary is assigned to each elementary pathway based on the relative discharge in that pathway. The TDRW algorithm is applied to the individual particles and accounts for the stochastic processes that they experience. Solute breakthrough curves are calculated based on the residence time distribution of all particles in the network. The mean and variance of particle travel times for an elementary displacement of length  $dx$  is:

$$\mu_t(dx) = \frac{R}{v^2} \left( v + \frac{\partial D}{\partial x} \right) dx \quad (\text{S. 1.1})$$

$$\sigma_t^2(dx) = R^2 \frac{2D}{v^3} dx \quad (\text{S. 1.2})$$

where  $\mu_t$  [T] and  $\sigma_t^2$  [T<sup>2</sup>] are the mean and variance of the particle travel time distribution,  $v$  [L/T]

is groundwater velocity in the fracture,  $D$  [ $L^2/T$ ] is the hydrodynamic dispersion coefficient along the fracture, and  $R$  [-] is the retardation coefficient due to sorption on the fracture walls.

The particle motion along an elementary pathway of length  $L$  [L] can be considered as a series of independent steps, and therefore the means and variances are additive (Rasmuson, 1985; Bodin et al., 2003c). Thus, the mean and variance of the particle travel time distribution for an elementary pathway can be written as:

$$\mu_t = \frac{R}{v^2} \int_0^L \left( v + \frac{\partial D}{\partial x} \right) dx = \frac{R}{v^2} \left( vL + \int_0^L \frac{\partial D}{\partial x} dx \right) \quad (\text{S. 1.3})$$

$$\sigma_t^2 = \frac{2R^2}{v^3} \int_0^L D dx \quad (\text{S. 1.4})$$

For Péclet numbers ( $P_e = vL/D$ ) [-] larger than 10, it can be shown that the travel time distribution is lognormal (Bodin et al., 2003). Therefore, the stochastic calculation of travel times for individual particles over an elementary pathway is given by:

$$\ln(\Delta t_f) = \mu_{ln} + Z_N \sigma_{ln} \quad (\text{S. 1.5})$$

$$\mu_{ln} = \ln \left( \mu_t / \sqrt{1 + \sigma_t^2 / \mu_t^2} \right) \quad (\text{S. 1.6})$$

$$\sigma_{ln}^2 = \ln(1 + \sigma_t^2 / \mu_t^2) \quad (\text{S. 1.7})$$

where  $\Delta t_f$  [L] is the time for particle  $f$  to travel along an elementary pathway,  $\mu_{ln}$  and  $\sigma_{ln}^2$  are the mean variance of the log transform, and  $Z_N$  is a random number drawn from a normal distribution.

Note that the TDRW method enables a scale-dependent dispersion coefficient provided that the spatial derivative in **Eq. (S.1.3)** is calculable. If indexes  $n$  and  $n + 1$  refer to the upstream and downstream nodes of an elementary pathway of length  $L$ , the particle travel time in this pathway can be written as:

$$t_{n+1} - t_n = \Delta t_f = \exp(\mu_{ln} + Z_N \sigma_{ln}) \quad (\text{S. 1.8})$$

Despite the simplicity of this technique, it does have limitations. In fracture networks,  $P_e$  can be less than 10, either locally in short fracture segments, or in elementary pathways with low flow velocities. The assumption of a lognormal travel time distribution in these bonds is flawed and yields inaccurate results. Bodin et al. (2003) proposed an empirical correction of **Eq. (S.1.6)** to preserve accuracy where  $P_e < 10$ . This correction is as follows:

$$\mu'_{ln} = \beta \mu_{ln} = \left(1 - \frac{1}{33P_e}\right) \ln\left(\frac{\mu_t}{\sqrt{1 + \sigma_t^2/\mu_t^2}}\right) \quad (\text{S. 1.9})$$

where  $\mu'_{ln}$  is the corrected mean of the log transform, and  $\beta$  [-] is the empirical correction factor.

## References

Bodin, J., Porel, G., & Delay, F. (2003). Simulation of solute transport in discrete fracture networks using the time domain random walk method. *Earth and Planetary Science Letters*, 208(3–4), 297–304. [https://doi.org/10.1016/S0012-821X\(03\)00052-9](https://doi.org/10.1016/S0012-821X(03)00052-9)

## Supplementary Data B (RWPT-Based Model)

The random walk particle tracking method (RWPT) involves the release of a large number of representative particles at the inlet boundary of a domain. For each particle, advective transport is simulated using a stepwise deterministic process, and dispersive transport using a stochastic process (e.g., LaBolle et al. 1996; Masciopinto 1999; Hassan and Mohamed 2003; Langevin 2003; Reeves et al. 2008; Masciopinto et al. 2010; Cadini et al. 2012; Willmann et al. 2013). Based on this, the spatial location of each particle is calculated after each time step as follows (Tompson and Gelhar, 1990):

$$X_{t+\Delta t} = X_t + [V(X_t, t) + \nabla \cdot d(V(X_t, t))]\Delta t + [2d(V(X_t, t))\Delta t]^{1/2} \cdot Z \quad (\text{S. 2.1})$$

where  $X_{t+\Delta t}$  [L] is the position of the particle at time  $t + \Delta t$ ,  $X_t$  [L] is the position of the particle at time  $t$ ,  $V(X_t, t)$  [L/T] is the velocity vector of the particle at position  $X_t$  and time  $t$ ,  $d$  [L<sup>2</sup>/T] is the local-scale dispersion tensor at  $X_t$  and time  $t$ ,  $\Delta t$  [T] is the time step, and  $Z$  is a tensor of random numbers drawn from a normal distribution with a mean of zero and a unit variance.

In order to apply this technique within discrete fracture networks (DFNs), the DFN must be conceptualized as a network of interconnected one-dimensional pipes (Bodin et al. 2003; Bodin et al. 2007). The RWPT model considered in this work considers the following processes:

1. Advection and mechanical dispersion along the fractures.
2. Diffusion into the matrix.
3. Reactive process within the matrix.

4. Reactive process on the fracture walls.

The fluid velocity in the fracture,  $V_f$  [L/T], is obtained from:

$$V_f = \frac{T_f dh}{n b dl} \quad (\text{S. 2.2})$$

where  $T_f$  [ $L^2/T$ ] is the transmissivity,  $n$  [-] is the porosity,  $b$  [L] is fracture's aperture size, and  $\frac{dh}{dl}$  is the hydraulic gradient. A particle with velocity  $v$  [L/T] located in a fracture oriented at an angle  $\theta$  (**Fig. S.2.1**) migrates some distance,  $\Delta l$  [L], due to advection and dispersion. This is calculated using the RWPT method represented as follows:

$$\Delta l = v \Delta t + \sqrt{2 d \Delta t} Z \quad (\text{S. 2.3})$$

where  $\Delta t$  [T] is the time step,  $d$  [ $L^2/T$ ] is hydrodynamic dispersion coefficient, and  $Z$  is a random number drawn from a normal distribution with zero mean and unit variance. The dispersion coefficient is related to the velocity through the dispersivity,  $\alpha$  [L] as follows:

$$d = \alpha v + D^* \quad (\text{S. 2.4})$$

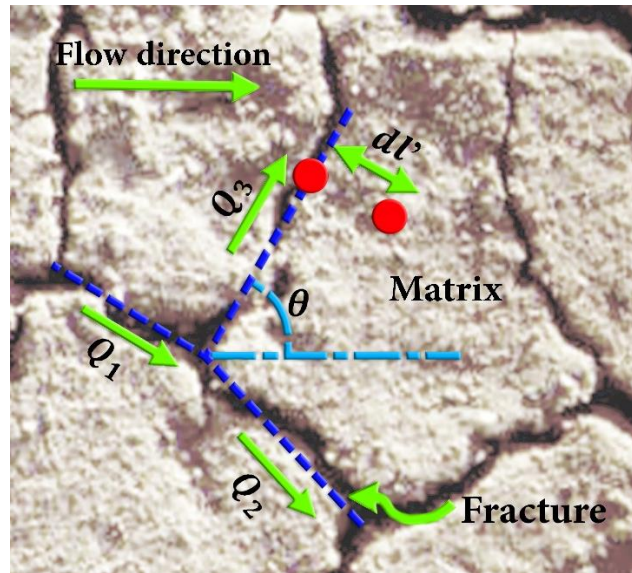


**Fig S.2.1: Fracture geometry and properties.** The solid arrows represent direction of flow and particle migration, the dashed lines are parallel plate representations of fractures, and the circles represent particles.

The new particle location can be obtained from:

$$X_{p\_new} = X_{p\_old} + dl \cos(\theta) \quad (\text{S.2.5})$$

$$Y_{p\_new} = Y_{p\_old} + dl \sin(\theta) \quad (\text{S.2.6})$$

where  $X_{p\_new}$  [L] and  $X_{p\_old}$  [L] are the new and old x-coordinates, respectively, and  $Y_{p\_new}$  [L] and  $Y_{p\_old}$  [L] are new and old y-coordinates, respectively.

The above equation and RWPT technique described are valid within the fracture length (i.e., as long as the particle has not reached the end node). Once a particle reaches the end node (i.e.,

fracture intersection), a mass sharing technique is applied to determine the probability distribution for the particle's new location with respect to the multiple downstream fractures. Park and Lee (1999) proposed the use of the perfect mixing approach, and estimated the particle transition probability between all downstream fractures based on relative discharge. The probability that the particle enters each downstream fracture is determined as follows:

$$P_j = \frac{Q_j}{\sum_{k=1}^N Q_k} \quad (S.2.7)$$

where  $P_j$  is the fraction of solute mass from the upstream intersection entering a downstream fracture  $j$ ,  $Q_j$  [ $L^3/T$ ] is the discharge in downstream fracture  $j$ , and  $N$  is the total number of downstream fractures. **Fig. S.2.1** shows a particle just upstream of the intersection of three fractures. When a particle is near to an intersection (i.e., either upstream or downstream), its location at the next time step is subject to one of the following three possibilities. The first possibility is that particle step is small enough such that it does not reach either an upstream or downstream intersection and remains in the same fracture. The second possibility is that particle step is exactly equal to the distance to an upstream or downstream intersection. In this case the particle will move to the intersection and remain there until the next time step. The third possibility is when the particle step is larger than the distance to the fracture intersection. In this case, the particle will move to the intersection in time  $\Delta t_1$ , which is less than the time step,  $\Delta t$ , as follows:

$$\Delta t_1 = \frac{L_{residual}}{dl} \Delta t \quad (S.2.8)$$

where  $L_{residual}$  [L] is the distance from the current particle location to the fracture intersection.

The remaining time ( $\Delta t_2 = \Delta t - \Delta t_1$ ) is then be used to move the particle from the intersection into a fracture that is selected based on the transition probability (**Eq. (S.2.7)**). The location within the new fracture is determined as follows:

$$dl_2 = V_i \Delta t_2 + \sqrt{2 d \Delta t_2} Z \quad (\text{S.2.9})$$

where  $V_i$  [L/T] is the new particle velocity, and  $d_i$  [L<sup>2</sup>/T] is the new particle hydrodynamic dispersion coefficient based on the new fracture's velocity  $V_i$ ,  $Z$  is a random number taken from a normal distribution with zero mean and unit variance.

### **Incorporating Diffusion Process**

There are two main required steps to incorporate the matrix diffusion process into the RWPT-based transport model:

1. Calculate the transfer probabilities of both solute particles moving from the fracture to the matrix and from the matrix to the fracture.
2. Calculate the diffusion distance for particles moving from the fracture to the matrix.

#### *Matrix Diffusion Step 1: Transfer Probabilities*

The particle transfer probabilities developed by Pan and Bodvarsson (2002) are used in this RWPT-based model as follows:

$$P_{fm} = \frac{F_{fm}}{Q_f + F_{fm}} \left[ 1 - \exp\left(-\frac{\Delta t}{\tau_f}\right) \right] \quad (\text{S.2.10})$$

$$P_{mf} = \frac{F_{mf}}{Q_m + F_{mf}} \left[ 1 - \exp\left(-\frac{\Delta t}{\tau_m}\right) \right] \quad (\text{S. 2.11})$$

$$F_{fm} = \max(q_{fm}A_{fm}, 0) + \frac{D_m A_{fm}}{S_{fm}} \quad (\text{S. 2.12})$$

$$F_{mf} = \max(-q_{fm}A_{fm}, 0) + \frac{D_m A_{fm}}{S_{fm}} \quad (\text{S. 2.13})$$

$$Q_f = \sum_{i=1}^N \left[ \max(q_f A_i, 0) + \frac{D_{fi} A_i}{S_i} \right] \quad (\text{S. 2.14})$$

$$Q_m = \sum_{i=1}^N \left[ \max(q_m A_i, 0) + \frac{D_{mi} A_i}{S_i} \right] \quad (\text{S. 2.15})$$

$$\tau_f = \frac{V_f R_f}{F_{fm} + Q_f} \quad (\text{S. 2.16})$$

$$\tau_m = \frac{V_m R_m}{F_{mf} + Q_m} \quad (\text{S. 2.17})$$

where  $P_{fm}$  and  $P_{mf}$  are the diffusion probabilities for particles moving from the fracture to the matrix and from the matrix to the fracture, respectively,  $F$  [ $L^3/T$ ] is the strength of the advection and dispersion/diffusion processes across the fracture-matrix interface,  $Q$  [ $L^3/T$ ] is the strength of advection and dispersion/diffusion processes through the interfaces to adjacent grid cells in the same continuum,  $\tau_f$  and  $\tau_m$  [T] are the characteristic times of the fracture continuum and the

matrix continuum, respectively,  $\Delta t$  [T] is the time step,  $A_{fm}$  and  $A_i$  [L/T] represent the areas of the fracture-matrix interface within the grid cell and the interface adjacent to the  $i^{th}$  cell, respectively,  $q_{fm}$  and  $q_i$  [L/T] represent the fluid flux across the fracture-matrix interface within the grid cell and the interface adjacent to the  $i^{th}$  grid cell, respectively,  $D_m, D_{fi}$  and  $D_{mi}$  [L<sup>2</sup>/T] are effective dispersion coefficients in the matrix within the grid cell, the fracture continuum at the interface of the  $i^{th}$  adjacent cell, and the matrix continuum at the interface of the  $i^{th}$  adjacent cell, respectively,  $S_i$  [L] is the distance between the centers of the cell and the  $i^{th}$  adjacent cell,  $S_{fm}$  [L] is the characteristic length of the fracture-matrix system, and  $V_m$  [L<sup>3</sup>] is the total matrix volume.

Pan and Bodvarsson (2002) developed equations describing the activity range to have the ability of capturing the transient features of the diffusion depth into the matrix for a certain pulse. The probabilities developed by Liu, Bodvarsson, and Pan (2000) use the total matrix volume  $V_m$  and the fixed characteristic distance  $S_{fm}$  regardless of the time. In reality, the full matrix volume and the characteristic distance are time dependent. The following equations describing the activity range:

$$V_m(t_p) = V_m \frac{B^*(t_p)}{B} \quad (\text{S. 2.18})$$

$$S_{fm}(t_p) = S_{fm} \frac{B^*(t_p)}{B} \quad (\text{S. 2.19})$$

$$B^*(t_p) = \min \left( 4 \sqrt{\frac{4\sqrt{4D't_p}}{R'}}, B \right) \quad (\text{S. 2.20})$$

where  $t_p$  [T] is the time elapsed from the pulse injection, which can be considered as the particle's age in the dual-continuum particle tracking method,  $2B$  [L] is the fracture spacing,  $B^*(t_p)$  [L] is the activity range,  $D'$  [L<sup>2</sup>/T] is the diffusion coefficient in the matrix, and  $R'$  [-] is the retardation factor for sorption in the matrix.

#### *Matrix Diffusion Step 2: Migration into the Matrix*

Subsequent to the transfer probabilities determining which particles will diffuse into the matrix, the following equation determines the distance that a particle will diffuse into the matrix ( $dl'$  [L]):

$$dl' = b + B \times U' \quad (\text{S. 2.21})$$

where  $b$  [L] is half of the aperture,  $B$  [L] is matrix length,  $U'$  [0,1] is a random number taken from a standard uniform distribution. **Fig. S.2.1** shows a particle moving a distance  $dl'$  into the matrix.

### **Sorption**

#### *Sorption in the matrix*

The reactive transport problem is represented by the Advection-Dispersion Equation with the addition of the sorption term as shown in the following equations:

$$\frac{\partial C}{\partial t} + \frac{\partial S}{\partial t} = \nabla \cdot (d \cdot \nabla C) - \nabla \cdot (VC) = 0 \quad (\text{S. 2.22})$$

$$\frac{\partial S}{\partial t} = K_r(K_d C - S) = K_f C - K_b S \quad (\text{S. 2.23})$$

where  $C$  [M/L<sup>3</sup>] is the aqueous phase concentration,  $S$  [M/L<sup>3</sup>] is the sorbed phase concentration,  $V$  [L/T] is the velocity vector,  $d$  [L<sup>2</sup>/T] is the local scale dispersion tensor,  $K_d$  [-] is the partition coefficient,  $K_r$  [T<sup>-1</sup>] is the reaction rate coefficient,  $K_f$  [T<sup>-1</sup>] is a forward rate coefficient, and  $K_b$  [T<sup>-1</sup>] is a backward rate coefficient.

Kinzelbach (1988) and Valocchi and Quinodoz (1989) presented a detailed discussion on using the RWPT technique for simulating transport of kinetically sorbing solutes with deterministic reaction rate coefficients for a one dimensional flow field. The RWPT model used in this work builds on their methodology, simulating the transport of kinetically sorbing solutes with deterministic reaction rate coefficients in a two-dimensional flow field.

In the RWPT model, the particle moves between the aqueous phase (state 1) and the sorbed phase (state 2). At any instant in time, the particle exists in one of these two states. Each particle is assigned a state variable  $Y(t)$ , where  $Y(t) = 1$  for the aqueous phase and  $Y(t) = 2$  for the sorbed phase. Initially all particles are assumed to be in the aqueous phase. The advection - dispersion steps are only applied to particles in the aqueous phase. At the end of each time step, the particles may change their phase according to two transitional probabilities,  $P_{1,2}$  and  $P_{2,1}$ .

$$P_{1,2} = K_f \times \Delta t \quad (\text{S. 2.24})$$

$$P_{2,1} = K_b \times \Delta t \quad (\text{S. 2.25})$$

where  $P_{1,2}$  is the probability that a particle changes its state from the aqueous to sorbed phase,  $P_{2,1}$  is the probability that the particle changes its state from the sorbed to aqueous phase, and  $\Delta t$  [T] is the time step.

At the end of each time step a uniform random distribution  $X$  [0,1] is drawn for each particle. The final state,  $Y(t + \Delta t)$ , is adjusted according to **Eq. (S.2.26)** for particles in the aqueous phase, and according to **Eq. (S.2.27)** for particles in the sorbed phase.

$$Y(t + \Delta t) = \begin{cases} 2, & X < P_{1,2} \\ 1, & X \geq P_{1,2} \end{cases} \quad (\text{S. 2.26})$$

$$Y(t + \Delta t) = \begin{cases} 1, & X < P_{2,1} \\ 2, & X \geq P_{2,1} \end{cases} \quad (\text{S. 2.27})$$

where  $Y(t + \Delta t)$  is the updated state of the particle after time step  $\Delta t$ . This process is repeated at each time step. Sorption acts to retard the particles; the average retardation factor for sorption in the matrix can be calculated as:

$$R' = 1 + \frac{K_f}{K_b} \quad (\text{S. 2.28})$$

### *Sorption on fracture walls*

The reactive transport problem on fracture walls is represented by the following equation:

$$\frac{\partial S}{\partial t} = K_f C - K_b S = K_f \left( C - \frac{1}{K_a} S \right) \quad (\text{S. 2.29})$$

where  $C$  [M/L<sup>3</sup>] is the aqueous phase concentration,  $S$  [M/L<sup>3</sup>] is the sorbed phase concentration,

and  $K_a$  [L] is the fracture distribution coefficient ( $K_a = K_f/K_b$ ). The retardation factor of sorption on the fracture wall can be calculated as:

$$R = 1 + \frac{K_a}{b} \quad (\text{S.2.30})$$

where  $R$  is the retardation factor due to sorption on the fracture wall. **Eqs. (S.2.24 – S.2.27)** and **Eq. (S.2.30)** may be implemented using either the forward and backward rate coefficients,  $K_f$  and  $K_b$ , or the retardation factor,  $R$ , as input data.

## References

- Liu, H. H., G. S. Bodvarsson, and L. Pan. 2000. "Determination of Particle Transfer in Random Walk Particle Methods for Fractured Porous Media." *Water Resources Research* 36(3):707–13.
- Pan, Lehua, and Gudmundur S. Bodvarsson. 2002. "Modeling Transport in Fractured Porous Media with the Random-Walk Particle Method: The Transient Activity Range and the Particle Transfer Probability." *Water Resources Research* 38(6):16-1-16–17.